Gas flow through methane oxidation systems

A laboratory and numerical study for optimising system design

Charlotte van Verseveld

Gas flow through methane oxidation systems

A laboratory and numerical study for optimising system design

by

Charlotte J.W. van Verseveld

in fulfilment of the requirements for the degree of

Master of Science
in
Applied Earth Sciences

at the Delft University of Technology,
to be defended publicly on Friday July 6, 2018 at 16.00 PM.

Thesis committee:

Dr. J. Gebert (Chair)	TUDelft Geo-Engineering
Prof. Dr. Ir. T.J. Heimovaara	TUDelft Geo-Engineering
Dr. H. Hajibeygi	TUDelft Petroleum Engineering

Department of Geoscience & Engineering
Delft University of Technology

Summary

Landfills have been indicated as a major source of methane emissions. Inside a landfill the biodegradable part of the organic material is degraded, producing landfill gas, which mainly consists of methane ($55-60\%$) and carbon dioxide ($40-45\%$). The global warming potential of one mole of methane is 28 times higher than one mole of carbon dioxide, therefore these methane emissions must be avoided. Methane oxidation systems are 'low technology' systems that can treat the landfill gas. They do so by providing a suitable environment for bacteria (methanotrophs), which oxidise the methane into carbon dioxide. Methane oxidation systems comprise of a methane oxidation layer, in which the methanotrophs live, underlain by a gas distribution layer. The required oxygen is retrieved from the atmosphere and flows into the methane oxidation layer from the top. The methane is provided by the landfill gas and flows via the gas distribution layer into methane oxidation layer. The gas distribution layer has the function to spatially homogenise the landfill gas distribution, before the gas enters the methane oxidation layer in order keep the landfill gas flux low, allowing the needed oxygen to flow in from the top. Yet, methane oxidation systems are herein still sub-optimal and leave room for improvement. Therefore, there is a need to optimise the spatial homogeneity of the gas flux into the methane oxidation layer.

The objective of this thesis is to provide insight into the required effective gas permeability ratio between the gas distribution layer and the methane oxidation layer necessary to achieve a spatial homogeneous methane load, and into the amount and spatial distribution of the gas inlet points. To research this, a numerical model was established. Furthermore, laboratory experiments were performed to asses the influences of compaction level, hydraulic conditions and physical properties of a soil on the effective permeability of that soil. This was done in order to relate the permeability ratio to the design choice for the materials. All this is considered on a continuum scale in steady state therefore discarding dynamic influences such as weather, dynamic methane loads and settlement.

For the laboratory study pressure loss experiments were conducted on two different soils. In total, 18 soil samples were tested with varying compaction levels and water contents. From the results it can be concluded that the effective permeability is predominantly influenced by the compaction level and soil texture. Upon compaction the intrinsic permeability and correspondingly the effective permeability decrease exponentially. This means that the initial compaction will have a large influence on the effective permeability, while upon further compaction this influence become smaller and smaller. The soil texture defines the porosity and water retention characteristics. The coarse sand fraction mainly governs the amount of coarse pores, resulting in a higher intrinsic permeability. The clay fraction predominantly determines the water retention, and is thus likely to influence the connectivity and tortuosity of the air filled pore system. The saturation of the soil appears to have a significant influence only at near saturated conditions. This means that the choice of suitable material and adequate construction has more effect on the effective permeability than seasonal changes in saturation in moderate climates.

A numerical model was build to research the spatial homogeneity of the methane flux from the gas distribution layer into the methane oxidation layer. An advection & diffusion model with a simplified methane oxidation reaction was build in COMSOL Multiphysics. In total 60 simulations were performed. From the results it can be concluded that there are two parameters governing the spatial homogeneity of the methane fluxes from the gas distribution layer into the methane oxidation layers: the permeability

ratio between these layers, and the centre-to-centre distance between the inlet points. A design plot was generated, relating these two parameters for various homogeneity criteria. The design plot shows a quadratic increase in the required permeability ratio with an increasing centre-to-centre distance. The design plot can be used for the design of gas inlet systems and for the selection of the materials for the gas distribution layer and methane oxidation layer.

Samenvatting

Stortplaatsen zijn aangeduid als een belangrijke bron van methaanemissies. Binnen in een stortplaats wordt het biologisch afbreekbare deel van het organische materiaal afgebroken. Dit process produceert stortgas, wat voornamelijk uit methaan ($55 - 60\%$) en koolstofdioxide ($40 - 45\%$) bestaat. Het aardopwarmingsvermogen van één mol methaan is 28 keer groter dan van één mol koolstofdioxide. Daarom is het van belang dat deze methaanemissies voorkomen worden. Methaanoxidatiesystemen zijn technisch simpele systemen die het stortgas kunnen saneren. Deze systemen bieden een geschikte omgeving voor bacteriën (methanotrofen), die het methaan oxideren tot koolstofdioxide. Methaanoxidatiesystemen bestaan uit een gasdistributielaag met daar bovenop een methaanoxidatielaag, waarin de methanotrofen leven. De benodigde zuurstof wordt uit de atmosfeer gehaald en stroomt via de bovenkant van de methaanoxidatielaag naar binnen. Het methaan in het stortgas stroomt via de gasdistributielaag door de bodem van de methaanoxidatielaag naar binnen. De gasdistributielaag heeft de functie om de laterale distributie van het stortgas te homogeniseren, voordat het stortgas de methaanoxidatielaag in stroomt. Dit zorgt voor een lage stortgasstroom door de methaanoxidatielaag en laat daardoor toe dat de zuurstof van bovenaf in tegengestelde richting stroomt. Op dit moment is het homogeniseren in de bestaande methaanoxidatiesystemen nog weinig efficient en is het noodzakelijk om de homogeniteit van deze laterale distribute van het stortgas te optimaliseren.

De doelstelling van dit onderzoek is om inzicht te geven in de benodigde ratio tussen de effectieve permeabilitiet voor gas van de gasdistributielaag en van de methaanoxidatielaag en tevens inzicht te geven in de maximale hart-op-hart afstand tussen de gasinlaatpunten, om deze lateraal homogene methaandistributie te bereiken. Om dit te onderzoeken is er een nummeriek model gegenereerd. Daarnaast zijn er laboratorium experimenten uitgevoerd om de invloeden van het compactieniveau, de hydraulische condities en de fysieke grondeigenschappen op de effectieve permeabiliteit voor gas vast te stellen. Beiden zijn uitgevoerd op een continue schaal voor een stabiele toestand en nemen dus geen dynamische invloeden mee zoals weer, dynamische methaanladingen of inklinking.

Voor het laboratoriumonderzoek zijn twee drukvervalexperimenten uitgevoerd op twee verschillende grondsoorten. In totaal zijn er 18 grondmonsters getest met varierende compactieniveaus en watergehaltes. Er kan geconcludeerd worden dat de effectieve permeabiliteit hoofdzakelijk wordt beinvloed door het compactieniveau en de grondtextuur. Bij verdichting verminderen de intrinsieke en bijbehorende effectieve permeabiliteit exponentieel. Dit betekent dat initiele verdichting een grote invloed heeft op de effectieve permeabiliteit, terwijl verdere verdichting steeds minder invloed heeft. De grondtextuur bepaalt de porositeit en waterretentiekenmerken van de grond. Met name de grovezandfractie bepaalt de hoeveelheid grove poriën. Meer grove poriën leidt tot een hogere intrinsieke permeabiliteit. De waterrentie wordt voornamelijk bepaald door de kleifractie, die hierdoor waarschijnlijk de connectiviteit en de tortuositeit van het met luchtgevulde poriënstelsel beinvloedt. Het watergehalte blijkt alleen een significante invloed te hebben onder bijna verzadigde omstandigheden. Dit betekent dat een gepaste materiaalkeuze en adequate constructie de effectieve permeabiliteit voor gas meer beinvloeden dan de seizoensgerelateerde veranderingen in het watergehalte in gematigde klimaten.

Het numerieke model is als advectie & diffusie model in combinatie met een versimpelde methaanoxidatiereactie gebouwd in "COMSOL Multiphysics". Met dit model is de benodigde ratio tussen de effectieve

permeabilitiet voor gas van de gasdistributielaag en van de methaanoxidatielaag onderzocht. In totaal zijn er 60 simulaties gedaan. Uit de resultaten kan geconcludeerd worden dat twee parameters bepalend zijn voor de laterale homogeniteit van de methaanstroom van de gasdistributielaag naar de methaanoxidatielaag: de ratio tussen de effectieve permeabilitiet voor gas van deze twee lagen, en de hart-op-hart afstand tussen de gasinlaatpunten.

Vervolgens, is er een ontwerpdiagram gemaakt, die deze twee bepalende parameters aan elkaar relateert voor verschillende homogeniteitscriteria. Het ontwerpdiagram laat zien dat bij een toenemende hart-op-hart afstand de benodigde permeabiliteitsratio kwadratisch toeneemt. Dit onwerpdiagram kan gebruikt worden voor ontwerptoepassingen aangaande het gasinlaatsysteem en voor de selectie van geschikte materialen voor de gasdistributielaag en de methaanoxidatielaag.

Preface

Throughout the past ten months, I had the opportunity to delve into subject of methane oxidation systems. It is a interesting principle where nature can purify our landfill emission of methane, contributing to a more sustainable world. Methane oxidation systems are still in a phase where detailed understanding of processes should be further expanded and design methods require specification. This thesis contributes on these points to improve methane oxidation systems.

The origin of my interest in the topic lies with Timo Heimovaara, who introduced me to the coupling of subsurface processes. I want to thank him for his supervison, ideas and critical attitude. Furthermore, my gratitude extends to Hadi Hajibeygi for his constructive feedback and to André van Turnhout for his assistance with COMSOL.

I would like to express a special thank-you to Julia Gebert, my daily supervisor and chair of my thesis committee, for her outstanding guidance and injection of enthusiasm. I thoroughly enjoyed our collaboration.

This thesis could not have been realised without the help of the laboratory technicians. Therefore, many thanks to Wim Verwaal, Arno Mulder, Han de Visser, Jens van den Berg and Marc Friebel.

Lastly, I would like to express my appreciation to my family and friends for their support and confidence in me.

Charlotte van Verseveld
Delft, 29 June 2018

Nomenclature

Abbreviations

AFP	Air filled porosity
EPS	Exopolymeric substances
GDL	Gas distribution layer
GHG	Green house gas
LFG	Landfill gas
MO	Methane oxidation
MOL	Methane oxidation layer
MOS	Methane oxidation system

Chemical formulas

$[CH_4]$	Methane concentration in the aqueous phase
$[O_2]$	Oxygen concentration in the aqueous phase
$CaCO_3$	Calcium carbonate
CH_4	Methane
CO_2	Carbon dioxide
H_2O	Water
N_2	Nitrogen
N_2O	Nitrous oxide
O_2	Oxygen

Subscripts

0	At time=0
α	α-phase, can be either the water phase or the total gas phase
atm	Atmospheric
c	Capillary
e	Air entry
eff	Effective
end	At the last time step
g	Total gas phase
i	Component i

j	Component j, which is not component i
m	Gas mixture
R	Radius
res	Residual
T	Total volume
w	Water phase
wt	Water table

Superscripts

$*$	Effective
D	Nonequimolar
K	Knudsen
V	Total advective

Parameters

β	Compressible of water	$[m^2/N]$
γ	Surface tension	$[N/m]$
κ	Intrinsic permeability	$[m^2]$
λ	Decay factor	$[-]$
λ	Pore size distribution index	$[-]$
μ	Dynamic viscosity	$[Pa \cdot s]$
ν	Kinematic viscosity	$[m^2/s]$
ϕ	Total porosity	$[-]$
ρ	Density	$[g/cm^3]$
θ	Volumetric content	$[-]$
θ	contact angle	$[rad]$
A	Area	$[cm]$,$[m]$
c	Concentration	$[mol/m^3]$,$[mol/L]$
D	Chemical potential coefficient	$[mol/Jms]$
D	Mean grain diameter	$[m]$
D_{ij}	Binary diffusion coefficient	$[m^2/s]$
D_{pr}	Proctor density	$[g/cm^3]$
E	Energy	$[J]$
F	Methane flux from the GDL into the MOL	$[mol/m^2day]$
g	Gravitational acceleration	$[m/s^2]$
h	Capillary/hydraulic head	$[m]$
H^{cp}	Henry's constant	$[mol/^3Pa]$
h_{fall}	Fall height	$[m]$
J	Diffusive flux	$[mol/m^2s]$

K_m	Michaelis-Menten constant	$[mol/m^3]$
k_r	Relative permeability	$[m^2]$
KE	Kinetic energy	$[J]$
L	Length of the soil sample	$[m]$
M	Molar mass	$[g/mol]$
m	Falling weight	$[kg]$
N	Flux	$[mol/m^2s]$
n	Number of drops	$[-]$
P	Pressure	$[Pa]$,$[hPa]$
PE	Potential energy	$[J]$
q	Specific discharge	$[m/s]$
R	Radius	$[m]$
R	Reaction rate	$[mol/m^3day]$
R	Universal gas constant	$[J/Kmol]$
Re	Reynolds number	$[-]$
S	Saturation	$[-]$
T	Temperature	$[K]$
t	Time	$[s]$,$[day]$
V	Velocity	$[m/s]$
V	Volume	$[m^3]$
V_{max}	Maximum reaction rate	$[mol/m^3day]$
x	Mole fraction	$[-]$
z	Elevation from a fixed datum	$[m]$

List of Figures

List of Tables

Contents

1 Introduction

This chapter first provides a general introduction to landfills, methane oxidation systems, and their impact on climate, to explain the motivation for this research. Subsequently the problem description and the strategy for problem solving are given. Chapter 2 elaborates on methane oxidation systems and Appendix A on the atmosphere and climate change.

1.1 Landfills

Integrated waste management has become a popular way of managing waste, aiming to reduce the amount of waste (Sadasivam and Reddy, 2014). It does so by implementing the following hierarchy (IenM, 2014): prevention, reuse, recycling, energy recovery, flaring/burning, and land-filling. Although land-filling is the very last option in the chain, a large amount of waste still ends up in landfills: 25.3% of the EU municipal waste in 2015 (Eurostat URL, 2017) and even 52.6% of the USA municipal waste in 2014 (EPA, 2016).

The biodegradable part of the organic material within landfills (paper, animal matter, garden waste, etc.) is anaerobically degraded, producing landfill gas (LFG). This continues until the biodegradable part of the organic material has been degraded, which can take up to several decades. Typically LFG consists of $55 - 60\%$ methane (CH_4), $40 - 45\%$ carbon dioxide (CO_2) and traces of volatile organic compounds (Sadasivam and Reddy, 2014; Scheutz et al., 2009). Landfills have been indicated as a major methane source. In 2015 landfills contributed 18% of the anthropogenic methane emissions in the US (EPA, 2016). Both carbon dioxide and methane are greenhouse gasses, thereby contributing to global warming. Carbon dioxide has the largest contribution to global warming as there are significantly more global carbon dioxide emissions than the global methane emissions. Yet the global warming potential of one mole of methane is 28 times higher than one mole of carbon dioxide (IPCC, 2014).

To avoid the methane emissions, the LFG can be recovered. In modern engineered landfills the LFG recovery is primarily performed by gas collection systems. These are placed within the waste and actively capture the LFG, after which it is flared or used for energy recovery (Huber-Humer et al., 2008). The methane generation over the lifespan of a landfill is illustrated in Figure 1.1. It can be seen that gas collection systems are only in operation during the operation, closure and active aftercare phases, which cover not even half the lifespan. Besides, gas extraction is not 100% efficient, thus there are still methane emissions even with active gas collection system. As the landfill ages or has a low organic fraction (Scheutz et al., 2009), the methane production rate decreases. At some point it becomes economically infeasible to operate the gas collection system. The system is turned off and the passive aftercare phase initiates. This phase may continue for several decades up to a century. Over this passive aftercare phase, the net accumulation of methane is not negligible with respect to climate change (Huber-Humer et al., 2008).

Therefore, there is a need to implement additional (low-cost) methods to treat LFG. One such method,

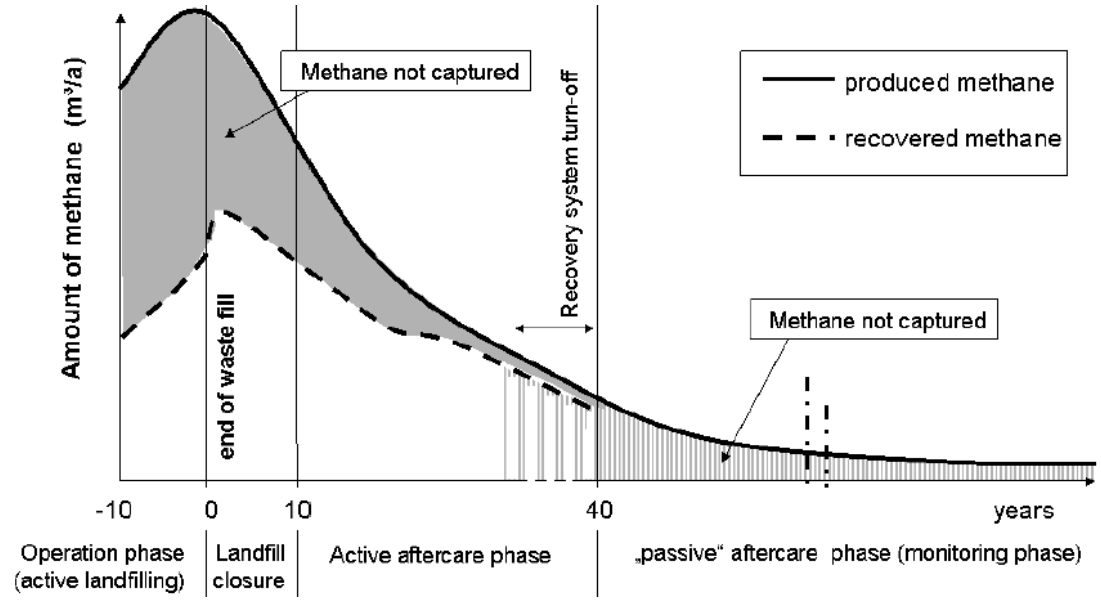

Figure 1.1: Methane generation over the phases of the lifespan of a landfill; adapted from (Huber-Humer et al., 2008).

often seen in combination with a gas collection system, is a methane oxidation system (Sadasivam and Reddy, 2014; Gebert et al., 2003; Huber-Humer et al., 2008; Scheutz et al., 2009; Ahoughalandari and Cabral, 2017). It has low operation expenses and requires little maintenance. This also makes this 'low technology' system suitable for developing countries (Scheutz et al., 2009), which generally landfill a bigger part of the waste generated.

1.2 Methane oxidation systems

Methane oxidation systems can be temporary (a day to months) or final (for the rest of the landfill life) (Sadasivam and Reddy, 2014). The temporary systems are used during the operation and closure phases, as depicted Figure 1.1, while final systems are used during both the aftercare phases. Various types of final systems exist: soil covers, biocovers, biofilters, and biowindows (Huber-Humer et al., 2008). The latter three are commonly referred to as methane oxidation systems (MOS) and will be the focus of this thesis. They comprise of a methane oxidation layer (MOL) underlain by a gas distribution layer (GDL). A soil cover is similar to a methane oxidation system, except it does not have a GDL.

1.2.1 General mode of operation

Methane oxidation systems are engineered systems to stimulate methanotrophy: the oxidation of methane to carbon dioxide by naturally occurring bacteria, which use the methane as carbon and energy source (Cao and Staszewska, 2013; Scheutz et al., 2009; Tuli et al., 2005; Gebert and Groengroeft, 2006). These specific bacteria are called methanotrophs and settle on the grain surfaces in the MOL surrounded by a water film. Generally the MOL is composed of organic rich materials (composts, peat, etc.) either alone or as amendments to a soil (Sadasivam and Reddy, 2014). This supports the methanotrophs via nutrients, proper water content and viable temperature regimes (Huber-Humer et al., 2008). Furthermore, the methanotrophs need a balanced methane and oxygen supply in order to have efficient oxidation. The LFG, and thus the methane, flows in via the base of the MOL, see Figure 1.2. The oxygen is retrieved from the atmosphere and thus flows in from the top of the MOL. After the methane is oxidised, the carbon dioxide flows into the atmosphere.

Due to the heterogeneity of the waste, the LFG flows out of the waste via preferential flow paths, creating spots of high LFG fluxes, so called 'hotspots'. When a gas extraction system is in place, the inlet points are also spots with high LFG fluxes. Due to the counter flow of LFG and air it is important too keep the LFG load low. Otherwise oxygen will not be able to flow in, preventing methanotrophy. For this reason, it is important to have an evenly distributed LFG flux into the MOL (Röwer et al., 2011; Ahoughalandari and Cabral, 2017). To establish this, the GDL is in place, which has the task to spatially homogenise the LFG fluxes before they enter the MOL. If this is not properly established, the methane flux is locally too high and is still emitted into the atmosphere. To establish this spread of LFG, the GDL needs to have a higher effective permeability than the MOL. Due to this permeability difference, the gas pressure can build up in the GDL, pushing the LFG in lateral direction. This only works if the ratio in effective permeability between the MOL and GDL is large enough. These effective permeabilities are governed by compaction level, hydraulic conditions, and the physical properties of the soil.

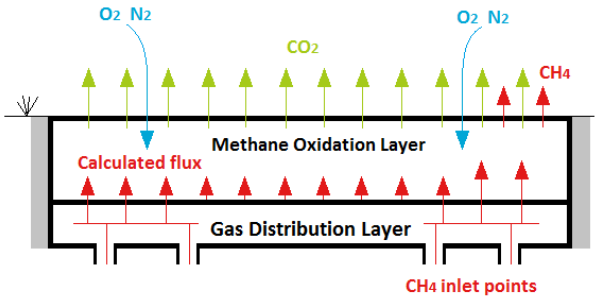

Figure 1.2: Schematic representation of a methane oxidation system.

1.3 Problem description

1.3.1 Problem statement

Ideally, the GDL distributes the LFG such that a perfect spatial equal load of LFG enters the MOL in order to obtain optimal methane oxidation. Röwer et al. (2011) and Ahoughalandari and Cabral (2017) emphasise the importance of an even distribution of methane fluxes entering the MOL. When dealing with soils, this ideal situation will never become reality, since soil is a heterogeneous material. Yet, methane oxidation systems are herein still sub-optimal and leave room for improvement. Therefore there is a need to optimise the spatial homogeneity of the gas flux into the MOL. Accordingly, more insight is needed into the behaviour of LFG flow at the boundary between the MOL and GDL. However, Ahoughalandari and Cabral (2017) indicate the lack of rigorous numerical studies on the uniformity of the LFG distribution and its ease to flow from the GDL into the MOL. These studies could provide tools for design purposes, such as assigning appropriate geometrical parameters or selecting materials with the appropriate geotechnical and hydraulic characteristics.

1.3.2 Objective

This research aims to establish a gas transport model for optimisation of the homogeneity of the gas flux into the MOL on continuum scale. Furthermore, for design and construction purposes, this research aims to provide insight into the effective gas permeability ratio between the GDL and MOL necessary to achieve a spatial homogeneous methane load and into the amount and spatial distribution of the gas inlet points.

1.3.3 Research questions

Multiple research questions are formulated in order to accomplish the objective:

1. How does the effective permeability of a soil depend on the compaction level of that soil?
2. How do the hydraulic conditions influence the effective permeability of a soil?
3. How does the effective permeability of a soil depend on the physical properties of that soil?
4. How can gas flow within a methane oxidation system be modelled?
5. What is the minimum effective permeability ratio between the methane oxidation layer and gas distribution layer for a homogeneous methane flux?
6. What should the centre-to-centre distance be of the gas inlet points to accomplish a homogeneous methane flux distribution?

1.3.4 Scope

This thesis focuses on the spatial distribution of the methane flux on a continuum scale. It will asses the spatial distribution in steady state, therefore discarding dynamic influences such as weather (rain, wind, temperature change, evaporation), change in methane load and settlement. Since the focus lies on the gas flow, only a simplified description of the methane oxidation process is taken into account. Furthermore, influences such as vegetation and animals, are out of scope. Chapter 2 gives an more elaborate overview of the scope of this thesis.

1.3.5 Approach

The first three research questions will be answered by the laboratory work performed. The other three questions are answered by means of the numerical study. Both the laboratory and numerical study are based upon the literature study.

Report structure
The literature study is presented in Part I. Chapter 2 elaborates on the workings of methane oxidation systems and the factors that influence them. It also gives an overview of the scope of this thesis. Chapter 3 discusses the theory behind gas flow through porous systems and discusses models used for methane oxidation systems found in literature.

Part 2 presents the laboratory studies. It starts off with an introduction on the experiments and more elaboration on the hypotheses in Chapter 4, followed by an elaboration on the materials and methods used in Chapter 5. Then the results are presented and discussed in Chapter 6, after which Chapter 7 shows the conclusions on this part.

Next, the numerical study is elaborated on in Part 3. Chapter 8 introduces the numerical model and its purpose, and it presents a more detailed hypothesis. Its implementation and verification are given in Chapters 9 and 10, respectively. Subsequently, Chapter 11 presents the results and discussion of the simulations. The results are concluded upon in Chapter 12.

This thesis concludes with the conclusions and recommendations in Part 4.

Part I

Background

2 Methane oxidation systems

The focus of this thesis will be on methane oxidation systems, which include biocovers, biofilters, and biowindows. These are all final systems, which are installed at the top-most part of the landfill cover. Biocovers cover the entire area of the landfill, whereas biofilters and biowindows cover smaller regions of the landfill. The latter are used when a full cover is not permitted or economically feasible (Huber-Humer et al., 2008). Biocovers and biowindows integrated into the landfill cover receive the LFG directly from underlying waste. These systems are passive, which means the LFG is solely driven by pressure and concentration gradients between the landfill and atmosphere. Flow rates and composition of LFG can be highly variable (Huber-Humer et al., 2008). Biofilters, however, need a supporting structure and require a gas collection system. These gas collection systems are often actively controlled, which means that the LFG is pumped into the methane oxidation system. Conditions regarding flow rates, composition, temperature and moisture can then be controlled (Gebert et al., 2003).

Even though the system designs and implementation differ, all three systems are based on the same oxidation and transport processes. There are processes driving the gas transport, but at the same time there is resistance governed by the permeability, since it is a transport through a porous medium. The drivers and permeability together govern the availability of methane and oxygen for the methane oxidation process. The methane oxidation process itself has again an influence on the drivers and permeability of the gas transport. An overview of the processes and the scope of this thesis is given in Figure 2.1. These processes will be explained in the rest of this chapter.

2.1 Drivers of gas transport

Gas transport is driven by two key parameters: concentration gradient and pressure gradient. Inside the landfill, organic matter is biodegraded producing land fill gas. The LFG has a different composition than the atmosphere, creating a concentration gradient between the landfill and atmosphere. The compositions of the atmosphere and LFG generally do not vary much between different locations. The composition of LFG typically consists of $55 - 60\%$ methane (CH_4), $40 - 45\%$ carbon dioxide (CO_2) and traces of volatile organic compounds (Sadasivam and Reddy, 2014; Scheutz et al., 2009). The composition of air is 78% nitrogen (N_2), 20% oxygen (O_2), and some water vapour, argon, carbon dioxide, and other gases (ThoughtCo URL, 2017).

Furthermore, the flow of LFG is blocked by low permeability of the waste and the landfill cover. Therefore pressure can build up, creating a pressure difference between the landfill and atmosphere. Gebert and Groengroeft (2006) performed a research on the effect of pressure change. Over-pressure, thus a LFG pressure exceeding the atmospheric pressure, causes LFG emission toward the atmosphere. Under-pressure can completely reverse the gas flux drawing air in through the methane oxidation system and gas extraction system into the landfill. LFG pressure change is dependent on the production rate of the LFG and the resistance to gas flow, enabling the pressure built up inside the landfill.

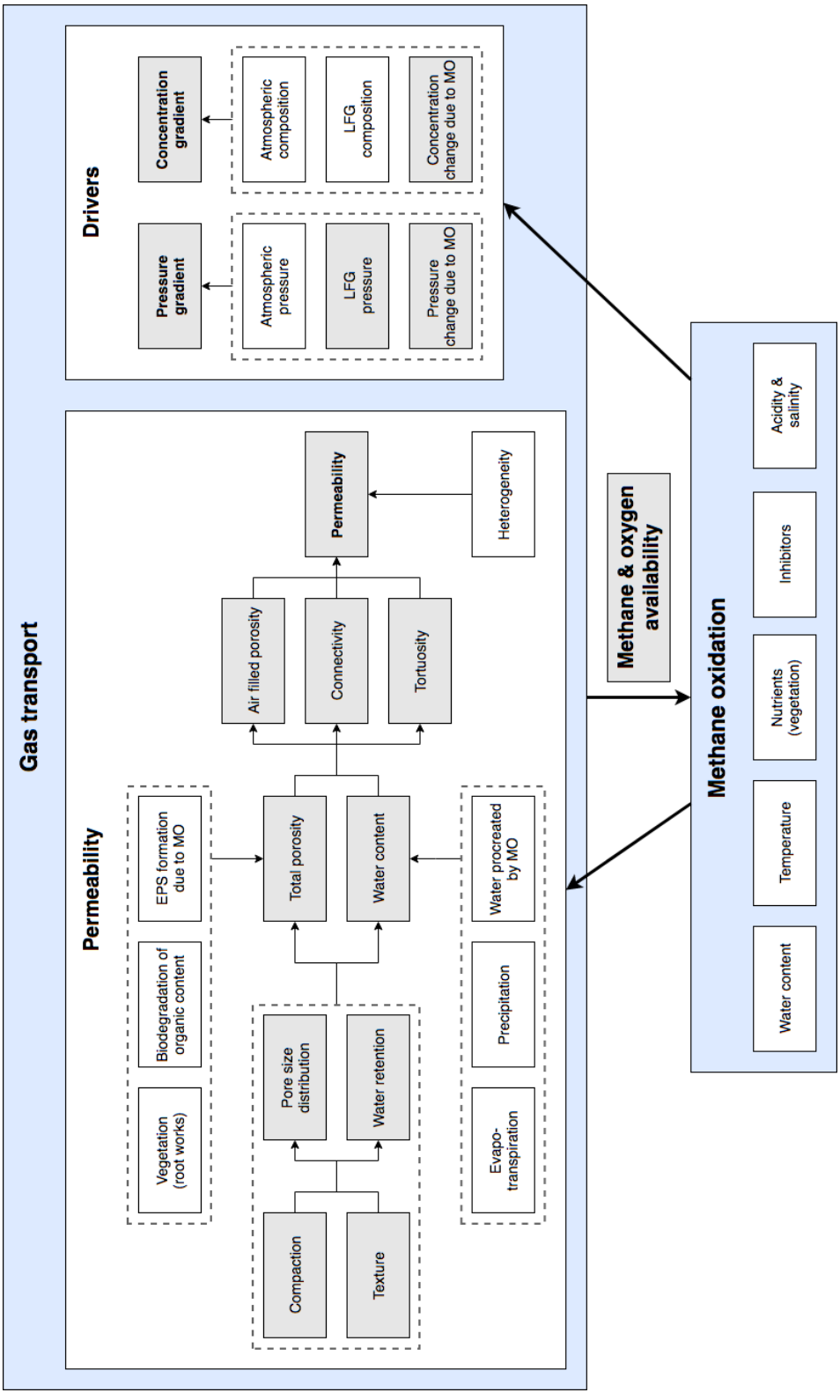

Figure 2.1: An overview of the factors influencing methane oxidation systems; MO = methane oxidation, LFG = landfill gas, EPS = exopolymeric substances. The dashed lines mean all blocks inside have an influence on the next block. The grey blocks represents the scope of this thesis.

According to a literature study by Scheutz et al. (2009) the methane production depends upon several factors, among which the landfill waste volume, the organic fraction and biodegradability, its age, and multiple environmental factors. Pressure change can be caused by a change in LFG pressure or atmospheric pressure. Atmospheric pressure at the earth's surface ($1atm = 101325Pa$) varies on three different scales: Firstly, the auto-oscillation of air varies the atmospheric pressure by $\pm 1hPa$. Secondly, the daily alternation of sunlight varies the atmospheric pressure by $\pm 4hPa$. Thirdly, the weather/temperature, the passage of atmospheric pressure highs and lows vary the atmospheric pressure by $\pm 20hPa$.

2.2 Permeability

The gas flows from the landfill via the methane oxidation system into the atmosphere. The methane oxidation system creates resistance to the gas flow, since its ability to let flow pass (the permeability) is relatively low. The permeability is described with the effective permeability and the diffusivity of the methane oxidation system for flow driven by pressure and concentration gradients, respectively. The larger they are the easier it is for the methane oxidation system to supply the methanotrophs with methane and oxygen. However, if they become too similar to the effective permeability and diffusivity of the gas distribution layer, the methane flux will not spread (homogeneously) through gas distribution layer before it enters the methane oxidation layer, creating solely a local supply for the methanotrophs.

2.2.1 Air filled porosity, connectivity and tortuosity

The permeability is governed by three main factors (Tuli et al., 2005) as indicated in Figure 2.1. Firstly, the air filled porosity (AFP), which is the share of total porosity occupied by air. Secondly, the connectivity, which describes how well the air filled pores are connected and how much of the air filled porosity actually contributes to the flow. Thirdly, the tortuosity, which determines the path length a gas particle needs to travel relatively to the effective length it travels. The larger the air filled porosity and connectivity, the higher the permeability. In contrast, the higher the tortuosity the lower the permeability. Gebert et al. (2011) showed that there was a threshold for the AFP of $10\%V$ below which connectivity was obstructed.

2.2.2 Total porosity and water content

The air filled porosity, connectivity and tortuosity are mainly governed by the total porosity and water content, see Figure 2.1. Total porosity is the space not occupied by solids and is highly influenced by the texture and compaction of the soil. It can be filled by anything other than solids. Secondary influences on total porosity are for instance vegetation (roots loosen up the soil) (Wang et al., 2008; Bohn et al., 2011; Tanthachoon et al., 2008), and organic content (biodegradable, resulting in settlement of the MOL which may reduce the effective permeability) (Huber-Humer, 2004). The water content is the amount of water in the soil and is influenced by factors such as evapotransipration, precipitation and frost (volumetric expansion of the water). But it is also governed by the water retention characteristics of the soil, as explained in more detail in the paragraph below. Furthermore water is produced during methane oxidation as will be explained in Section 2.3.

It is shown in literature that the water content strongly effects both the effective diffusivity (Cabral et al., 2004) and the gas effective permeability (Gebert et al., 2011). This is both due to the fact that an increase in water content leads to a decrease in air filled porosity and to an increase in tortuosity. Furthermore, if the water content gets high enough to obstruct connectivity, the gas has to diffuse through the water. This transport process is four orders of magnitude slower than transport through air.

Water retention

The water retention characteristics of a soil depend on the pore size distribution as explained in more detail in the next paragraph. The smaller the pores the better they can retain the water due to capillary

forces, which will be explained in Chapter 3. The share of wide coarse pores ($d > 50\mu m$) are drained under gravity even at elevated moisture levels. Therefore, they predominantly control the AFP (Gebert et al., 2011; Tuli et al., 2005). The water is thus bound by the pores with a diameter less than $50\mu m$, which is according to a capillary pressure of $60hPa$.

A methane oxidation system comprises of a finely textured soil (the MOL) situated on top of a course textured material (the GDL). This creates the potential of forming a capillary barrier (Ahoughalandari and Cabral, 2017): the MOL retains water at the boundary between the MOL and GDL. This capillary barrier may block the LFG transport from the GDL into the MOL. As a consequence, the lateral gas transport of the LFG may be increased, which in turn can cause emissions next to the landfill.

Pore size distribution
The texture and compaction together determine the pore size distribution. Well sorted coarse soils will have (mainly) wide coarse pores, whereas well graded soils will have pores of all sizes and fine soils will have (mainly) smaller pores. Gebert et al. (2011) showed that soil compaction leads to a decrease in total porosity and simultaneously affects the pore size distribution. Compaction mainly affects the wide coarse pores. The susceptibility towards compaction determines the extent of compaction effects and thus in fine-textured materials these effects are more pronounced than in sandy soils, even though sandy soils have a higher share of wide coarse pores. Furthermore the pore size distribution has an influence on the connectivity and tortuosity. Generally, smaller pores sizes lead to lower connectivity and higher tortuosity, which even more pronounced due to the high water retention characteristics of small pores.

2.2.3 Heterogeneity

Lastly, the resistance to gas transport is influenced by the heterogeneity of the soil, as the gas will always migrate along the path of least resistance. This preferential flow can overload the methane oxidation layer locally, creating a 'hotspot'. The homogeneity is often disturbed by cracks and fissures, which are caused by multiple reasons according to Scheutz et al. (2009): landfill settlement, wetting and drying of the methane oxidation layer, or vegetation and their roots. But also spatial differences in texture, compaction and water content can lead to preferential flow paths (Röwer et al., 2011). Furthermore, hotspots can be caused by heterogeneous gas production, which is inherent to the highly heterogeneous waste.

2.3 Methane oxidation

The key process to a methane oxidation system is methanotrophy. This is the process where bacteria, methanotrophs, oxidise methane to carbon dioxide to obtain energy and carbon to live on (Cao and Staszewska, 2013; Scheutz et al., 2009; Tuli et al., 2005; Gebert and Groengroeft, 2006). This biochemical reaction creates the opportunity to clean the LFG before it enters the atmosphere. The methane oxidation reaction is as follows (Scheutz et al., 2009):

$$CH_4 + 2O_2 \quad \longrightarrow \quad CO_2 + 2H_2O + \text{heat} \tag{2.1}$$

The biochemical reaction is dependent on the methane and oxygen availability. Increased methane loads stimulates population growth (biomass), which in turn increases the methane oxidation capacity (Gebert et al., 2003; Röwer et al., 2011). Too high loads, however, can impede oxygen ingress, limiting oxidation and increasing emissions (Gebert et al., 2011). There is thus an optimal LFG load to achieve maximum oxidation rate.

Equation 2.1 shows that the oxidation process leads to the formation of carbon dioxide. First of all this means that three moles of gas are turned into one mole of gas. This creates an under-pressure driving the gas transport of both the LFG and oxygen. Secondly, methane is oxidised into carbon dioxide, decreasing

the methane and oxygen concentrations and increasing the carbon dioxide concentrations in the methane oxidation layer. This drives the gas transport of methane and oxygen into the methane oxidation system, and for carbon dioxide out of the methane oxidation system into the atmosphere. However, it diminishes the diffusive transport of carbon dioxide into the methane oxidation system.

Lastly, equation 2.1 shows that water is formed during the oxidation process. Water is one of the major factors influencing methane oxidation rates, as discussed extensively in literature (Gebert et al., 2003; Sadasivam and Reddy, 2014; Cabral et al., 2004; Huber-Humer et al., 2008; Scheutz and Kjeldsen, 2004). The MOL must contain some water for the methanotrophs to live in to drain away metabolites. Furthermore, too little water will cause reduced activity or even desiccation. Excessive water will limit methane oxidation in two ways. 1) The water fills voids, so reduced space is available for gas transport. Therefore, methane and oxygen availability will be restricted. The impact of excessive pore water on the gas transport, depends on the pore size distribution of the soil. 2) The methane and oxygen have to travel a larger distance through the water towards the bacteria. Diffusion through water is order of 10^4 lower in water than in air, which slows down the methane oxidation rate.

The methane oxidation process is used by the methanotrophs to extract carbon from the carbon dioxide. This carbon is used for growth of the methanotroph population, thus for production of biomass. However, when there is excessive carbon, exopolymeric substances (EPS) are created. The EPS cover the cells and clog the pores, limiting diffusion into and out of the methanotrophs (micro-scale) and gas flow through the methane oxidation layer (macro-scale), respectively (Wilshusen et al., 2004). Thus the excessive formation of EPS leads to a reduced performance of the methane oxidation system.

In addition to the above mentioned factors, there are some environmental factors influencing methane oxidation, as can be seen in Figure 2.1: temperature, vegetation, inhibitors, acidity and salinity. In literature, optimum operating temperatures are found around $30°C$ (Scheutz and Kjeldsen, 2004; Huber-Humer et al., 2008; Gebert et al., 2003). Oxidation activity can occur down to $2°C$ (Christophersen et al., 2000; Scheutz and Kjeldsen, 2004). Hence, methane oxidation is strongly influenced by ambient temperature fluctuations. Materials with high air-filled porosity have an insulating effect (Huber-Humer, 2004), cited in (Scheutz et al., 2009), and thus maintain suitable temperature conditions during small fluctuations. During the seasons temperature fluctuations are larger over a longer time period, resulting in larger oxidation rates in summer then in winter (as long as it does not get too dry). The lower oxidation rates in the winter must be taken into account when dimensioning these methane oxidation systems.

Several studies have shown the positive effect of vegetation on methane oxidation (Wang et al., 2008; Bohn et al., 2011; Tanthachoon et al., 2008). Firstly, oxygen supply reaches deeper into the soil: The spreading roots loosen the soil structure and pore water is lost via evapotranspiration. Secondly, the plants' rhizosphere, a zone that surrounds the roots and is influenced by them, creates a favourable habitat for the methanotrophs: The roots and debris of dead plants improve nutrient (nitrogen, phosphorus) supply.

Inhibitors inhibit methane oxidation due to competition with methane for binding sites. There are multiple inhibitors indicated in literature, among which methyl, ammonium, nitrate, and certain pesticides (Scheutz et al., 2009). Some of these inhibitors can be contained withing the LFG itself.

Finally, the acidity and salinity of the soil. In literature, optimal pH values for methanotroph growth are found in the range of $5.5 - 8.5 pH$ (Scheutz et al., 2009; Cao and Staszewska, 2013; Scheutz and Kjeldsen, 2004). Since methanotrophs can adapt to a wide range of pH conditions and the pH value generally varies slightly around 7, acidity is not a major limiting factor. Higher salinity decreases methane oxidation due to osmotic stress (Gebert et al., 2003). The salt extract the water out of the bacteria, therefore methane oxidation systems will not perform optimally in salt environments.

2.4 Soil gas profile

A soil gas profile is the vertical pattern of soil gas composition. A typical gas profile for a methane oxidation system can be seen in Figure 2.2. From the processes describe above can be concluded that one of the key aspects of a methane oxidation system is the bi-directional flow of LFG and air. Due to this counter flux, the main activity of methanotrophs is confined to a relatively narrow band within the MOL. This (highly) active band was found in laboratory incubation experiments in the top 30cm of the soil sample (Scheutz et al., 2004; Kightley et al., 1995; de Visscher et al., 1999; Czepiel et al., 1996), and around 60cm depth (Pawlowska and Stephniewski, 2006). In field experiments the band was found in the top 60cm according to Rachor and Gebert (2009), cited within (Röwer et al., 2011). This can be seen in the figure on the right side. Below these depths, gas composition is close to the LFG composition. While in the active band, the soil gas composition changes due to the methane oxidation process. The exact soil gas profile depends on the methane oxidation performance, thus on the LFG ingress from the bottom, the oxygen ingress from the top and the methane oxidation activity. Hence, the soil gas profile is strongly dependent on the permeability and all its influencing parameters.

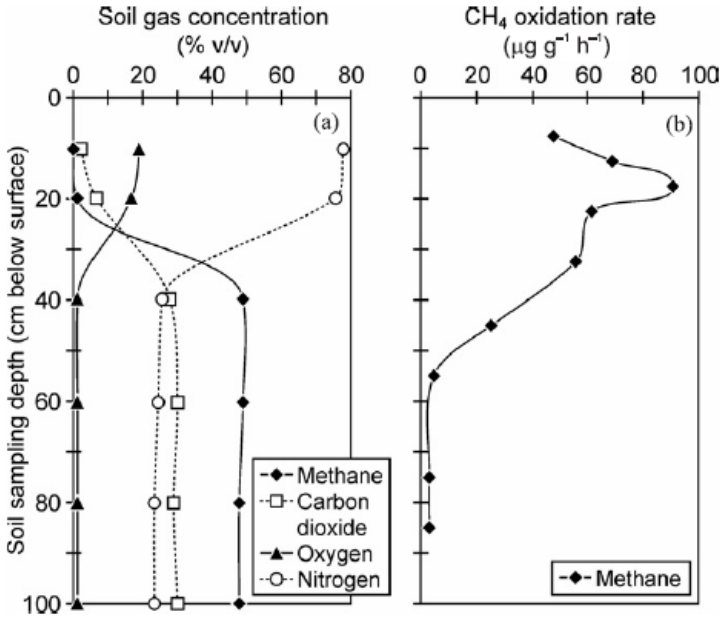

Figure 2.2: Typical gas profile inside the methane oxidation system; on the left, a soil gas concentration profile; on the right, the methane oxidation rates. (Scheutz et al., 2009)

In addition to the processes of gas transport and methane oxidation, additional processes play a role in determining the soil gas profiles. These processes occur in the top of the landfill, the landfill cover, and in the methane oxidation system. Among these processes are: aerobic respiration resulting in carbon dioxide production, and nitrification and de-nitrification (Scheutz et al., 2009).

3 Flow modelling

This chapter presents the theory behind water and gas transport through soils and how to model them on a continuum scale. This means that the soil can be represented by elementary volumes, which have average material properties of that volume. When the elementary volume is sub-divided into infinitesimal elements, these elements will still have the properties of the bulk material of the elementary volume. First, the unsaturated zone is elaborated on, after which the water model for such an unsaturated zone is discussed. Second, the main gas transport mechanisms and their implementation in numerical models are explained. Third, the methane oxidation model will be discussed. This chapter concludes with a mass balance and how the phases and their components are coupled.

3.1 Unsaturated zone

Methane oxidation systems are always situated in the unsaturated zone. In contrast to saturated, where all pores are filled completely with water, the pores inside the unsaturated zone are partially filled with water (liquid phase, $_w$) and partially with air or gas (gaseous phase, $_g$), as illustrated in Figure 3.1.

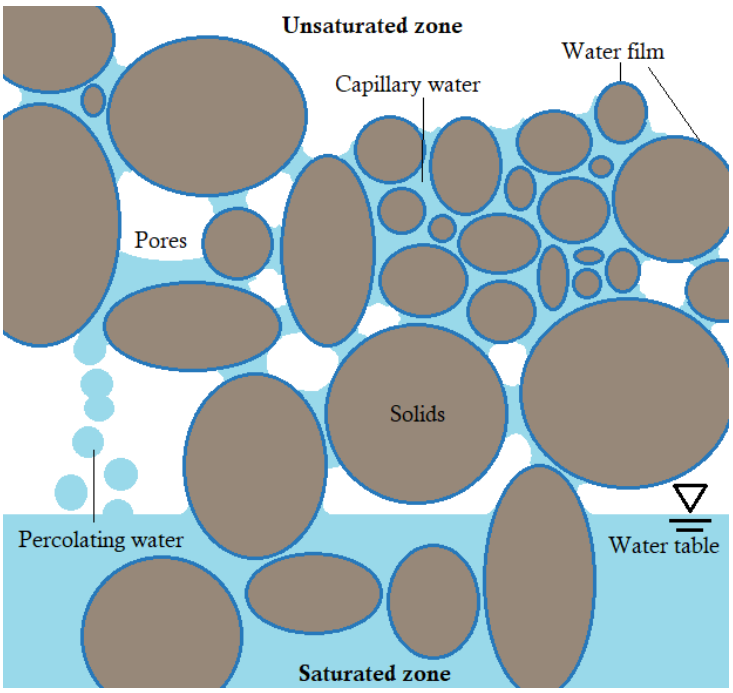

Figure 3.1: The main physical concepts of a soil, at particle scale.

The occupation of the pore space by the liquid or gaseous phase can be described in two ways (Bear and Cheng, 2010): in terms of volumetric fraction or in terms of saturation. The volumetric fraction (θ) is defined as equation 3.1 and the saturation (S) as equation 3.2.

Volumetric fraction:

$$\theta_\alpha = \frac{V_\alpha}{V_T} \tag{3.1}$$

Saturation:

$$S_\alpha = \frac{V_\alpha}{V_v} \tag{3.2}$$

Where V_α is the volume of the α-phase (which can be either the liquid ($_w$) or the gaseous ($_g$) phase), V_T the total volume, and V_v the pore space. The liquid and gaseous phases are related by the following equations, with ϕ being the porosity ($\phi = V_v/V_T$).

$$\theta_w + \theta_g = \phi \tag{3.3}$$

$$S_w + S_g = 1 \tag{3.4}$$

3.1.1 Capillarity

There are three phases in the unsaturated zone: the solid phase (grains), the liquid phase and the gaseous phase. They all behave in a certain way toward each other. First of all, the solids pull at the water and gas molecules. This causes the water to be around the solids and in the smaller pores (the wetting fluid), and the gas to be in the middle of the larger pores, only in contact with the water (the nonwetting fluid), see Figure 3.1. The molecular forces of the solids prevent complete drainage of the water; a thin film (only a few molecules thick) of adsorbed water will always remain around the solids. Within this water film, water cannot flow freely. Further away from the solids, these molecular forces are less strong and water is free to flow. The free water will to flow under gravity unless the soil pulls stronger at the water. When the solids are close together the forces between the solids and the water are larger than the cohesive forces within the water. This causes the free water to be retained or even to rise, which is capillarity. This is best explained when studying a tube with a small diameter, see Figure 3.2. The molecular forces at the sides of the tube pull at the water, creating negative pore water pressures and thus a difference in pressure at the interface of the two phases. The rise is the capillary head, h_c, and the pressure difference is the capillary pressure, p_c. They are defined as described in Bear and Cheng (2010):

$$P_c = P_{nonwetting} - P_{wetting} = P_g - P_w = \frac{2\gamma_{gw}\cos\theta}{R} \tag{3.5}$$

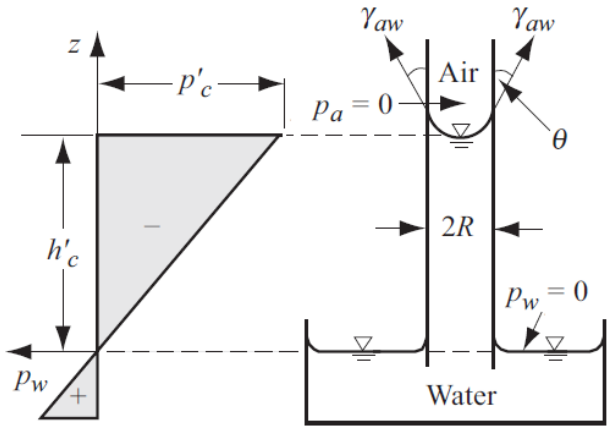

Figure 3.2: Schematic representation of a capillary tube; adapted from Bear and Cheng (2010). The gaseous phase is here represented by air ($_a$), while in the formulas this is by gas ($_g$).

$$h_c = \frac{P_c}{\rho_w g} \tag{3.6}$$

Where P_g and P_w are the gas and water pressures at the interface, γ_{gw} the surface tension between the gas and water phase, θ the contact angle, R the radius of the tube, ρ_w the density of water, and g the gravitational acceleration. The suction of the walls on the water holds the water against gravity. The capillary pressure is, therefore, inversely proportional to the radius of the tube. Hence, a wider tube creates less capillary rise than a narrower tube. Upon drying a soil, this causes the larger pores to be drained earlier than the smaller pores.

Plotting the dependency between the volumetric content and the capillary pressure results in a water retention curve as illustrated in Figure 3.3 for three types of soil; clayey, silty and sandy soil. Using equation 3.5, the capillary pressure can be translated into pore diameters. When the water content decreases fast in a certain, the pore sizes according to this are highly represented. Thus the water content for the sandy soil decreases already in the coarse pores region, while the water content for the clayey soil decreases mainly in the medium and fine pore regions.

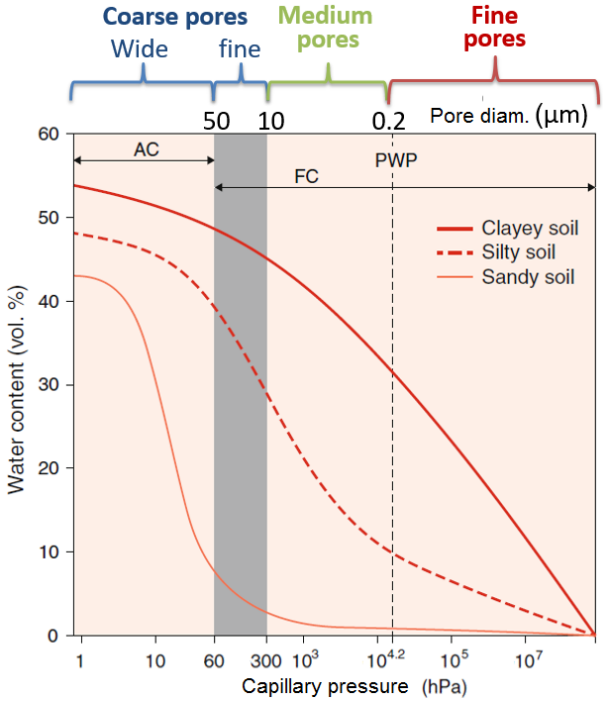

Figure 3.3: Typical water retention curves for different soil types; adapted from Gebert (2017).

Such a water retention model can be described by various formulations, among which the most known the Brooks and Corey formulation and the van Genuchten formulation. For this thesis the approach of Brooks and Corey is chosen, see equation 3.7. In this formulation the pores drain when the capillary pressure (the suction) is higher than the air entry pressure.

$$S_{eff} = \begin{cases} \left(\frac{P_e}{P_c}\right)^{\lambda}, & P_c > P_e \\ 1, & P_c \leq P_e \end{cases} \qquad \text{with} \qquad S_{eff} = \frac{\theta_w - \theta_{res}}{\phi - \theta_{res}} \tag{3.7}$$

Where S_{eff} is the effective saturation. P_e and P_c are the air entry pressure and the capillary pressure. θ_w and ϕ are the volumetric water content and total porosity, respectively. θ_{res} is the residual volumetric water content.

3.2 Water transport model

The basic law that governs the hydraulic flux under isothermal conditions in an unsaturated system is Darcy's law for unsaturated flow (Bear and Cheng, 2010):

$$q_w = -\frac{\kappa k_r}{\mu_w}\rho_w g \nabla h \tag{3.8}$$

Where q_w is the specific discharge, κ is the intrinsic permeability. k_r is the relative permeability factor and take the effects of saturation on the permeability into account. κ and k_r together they form the effective permeability. μ_w and ρ_w are the the dynamic viscosity and density of water and g is the gravitational acceleration. h is the hydraulic head, which consist of three parts: (a) elevation head, (b) pressure head, and (c) the kinetic energy head (Bear and Cheng, 2010).

$$\begin{underset{(a)}{h} = \underset{(a)}{z} + \underset{(b)}{\frac{P_w}{\rho_w g}} + \underset{(c)}{\beta\frac{V_w^2}{2g}}} \tag{3.9}$$

Where z is the elevation from a fixed datum, P_w is the hydraulic pressure, V_w is the (average) velocity of the water, and β is the compressibility of water. The velocity of water through porous media is very slow and, therefore, often negligible compared to the elevation and pressure heads (Bear and Cheng, 2010). Darcy's law can thus be simplified to:

$$q_w = -\frac{\kappa k_r w}{\mu_w}\left(\nabla P_w + \rho_w g \nabla z\right) \tag{3.10}$$

3.3 Gas transport mechanisms

Gas transport in unsaturated systems is the result of a combination of advection, diffusion (multiple types), mechanical dispersion and ebullition. This section elaborates on each of these transport mechanisms. They all follow the same principle: the gas molecules will go from a high energy state to a low energy state. The energy state results among others from the chemical composition, temperature and pressure.

3.3.1 Advection

Advection is the process in which the bulk flows. In this case the gas component flows along with the gas mixture (convection). The flow of the bulk gas acts as a continuum fluid driven by a pressure gradient as a result of external forces (Warrick, 2002). It is important to note that the pressure gradient results in bulk flow and does not segregate the gas into individual components. Therefore the driving force is the gradient of the total pressure of the gas mixture, and not the gradient of the partial pressures of the gas components. The resistance for the flow is caused by the viscosity of the gas mixture (and the porous medium). Therefore an other term for advective flow is viscous flow. For advective flux, the flux of component i is proportional to its mole fraction (x_i) in the gas mixture:

$$N_i^V = x_i N^V \tag{3.11}$$

Where N^V is the bulk flux due to external pressures. The bulk flux of gas can be described with Darcy's law modified for gas flow and must be written in terms of molar flux in this case. The gas is compressible and assumed to follow the ideal gas law. This results in the formulation of Darcy's law for gas:

$$N^V = -\frac{P}{RT}\frac{\kappa k_r}{\mu}\nabla P \tag{3.12}$$

Where P is the gas pressure, R the ideal gas constant, T the temperature, κk_r the effective permeability, μ the bulk gas viscosity, and ∇P the gas pressure gradient.

Advection is the dominant transportation process when the mean free path of the gas molecules is far smaller than the pore and particle radii, provided that a total pressure gradient exists. In a sand this is often the case. However, upon wetting the sand, the gas filled pore space becomes less. When the effective pore radius becomes approximately the same as the mean free path, viscous slip flux occurs (the Klinkenberg effect), which enhances the effective permeability. Tanikawa and Shimamoto (2006) showed that the Klinkenberg effect becomes important for soils/rock with permeabilities less than $10^{-18}m^2$. Therefore the Klinkenberg effect can be ignored for sands.

3.3.2 Diffusion

Multiple forms of diffusion are encountered: molecular diffusion, nonequimolar diffusion, Knudsen diffusion, thermal diffusion, surface diffusion and pressure diffusion. They will be discussed in similar order.

Molecular diffusion

Molecular diffusion is the transportation of components in a gas mixture due to a concentration gradient. For purely molecular diffusion isothermal and isobaric conditions are needed (Warrick, 2002). Equimolar pairs of gases (gas molecules with equal molecular weights) will then counter-diffuse, maintaining the isobaric conditions. For a binary gas mixture the molecular diffusion is described by Fick's law:

$$J_i = -D^*_{ij} \nabla c_i \tag{3.13}$$

Where D^*_{ij} is the effective binary diffusion coefficient and ∇c_i the molar concentration gradient of component i. Fick's law, however, cannot be used for a multicomponent gas mixture when binary diffusion coefficients are used. Therefore, Fairbanks and Wilke (1950) developed the following equation to approximate the diffusion coefficient of a component in a multicomponent gas mixture ($D_{i,m}$) based upon the binary diffusion coefficients in free gas (D_{ij}):

$$D_{i,m} = \frac{1 - x_i}{\sum \frac{x_j}{D_{ij}}} \tag{3.14}$$

D^*_{ij} (or $D^*_{i,m}$) can be calculated by equation 3.15 (Moldrup et al., 2000), with θ_G the volumetric gas content and ϕ the total porosity.

$$D^*_{ij} = \frac{\theta_g^{2.5}}{\phi} D_{ij} \tag{3.15}$$

Molecular diffusion is the dominant process when the mean free path of the gas molecules is far smaller than the pore radius, provided isobaric conditions. It decreases with increased water content in unsaturated systems; at low water contents, gas occupies the wider pores and water occupies the smaller pores, thus the decrease goes slowly. At higher water contents the decrease speed can suddenly be very high, when the large pores become occluded, obstructing the connectivity.

Nonequimolar diffusion and bulk diffusive flux

Nonequimolar diffusion occurs when gas components have different (nonequi-) molecular weights (-molar) (Warrick, 2002). When molecular diffusion occurs, the lighter molecules diffuse more faster than the heavier molecules. Therefore the total number of molecules in the gas are not equally spread any longer, creating a pressure gradient. Such a pressure gradient should be distinguished from external pressure gradients that drive advective flux. In this case, the pressure gradient is induced by molecular diffusion of a nonequimolar gas and results in nonequimolar flux. This nonequimolar flux does behave similar to an advective advective flux: a bulk gas flux, not separating the gas molecules. It is clear that nonequimolar

diffusion only occurs when molecular diffusion occurs in an nonequimolar gas mixture. This can be described by the bulk diffusive flux, which includes both diffusion mechanisms:

$$N_i^D = J_i + x_i N^D \tag{3.16}$$

Where N_i^D is the bulk diffusive flux for gas component i, and N^D is the nonequimolar flux, which is $\sum N_i^D$. Since nonequimolar flux is a bulk flux similar to advective flux, the flux of component i is proportional to its mole fraction (x_i) in the gas mixture.

Knudsen diffusion
Knudsen diffusivity is the dominant transport mechanism when the mean free path of the gas molecules is much greater than the pore radius, resulting in collisions between gas molecules and the pore walls (in unsaturated media this is often the gas-liquid interface) being dominant over intermolecular collisions (Warrick, 2002; Scheutz et al., 2009). Otherwise molecular diffusion, nonequimolar diffusion and advection mechanisms are the dominating processes and Knudsen diffusivity is negligible. de Visscher and van Cleemput (2003) argue that under atmospheric conditions Knudsen diffusion becomes dominant for pore diameters below $0.1\mu m$. These are the fine pores, mainly associated with clay, and are occupied by water for optimal methane oxidation conditions. Thus Knudsen diffusion can be discarded for methane oxidation systems.

Thermal diffusion
Thermal diffusion is the movement of a component relative to the gas mixture due to a temperature gradient, which in turn disturbs the homogeneity of the gas mixture (Warrick, 2002): the concentration in warmer and cooler regions becomes different, inducing molecular diffusion. Therefore, thermal diffusion is always formulated together with molecular diffusion, similar to nonequimolar diffusion. In this thesis temperature is assumed to be constant and thus thermal diffusion does not play a role.

Surface diffusion
Surface diffusion is a process in which gas molecules, absorbed to the solid surface, jump from one adsorption place to an adjacent adsorption place under a concentration gradient (Mason and Malinauskas, 1983). It takes into account all complexities such as porous medium geometry, surface structure, adsorption equilibrium, etc. However, in the unsaturated zone there is always a water-film around the solids, so limited solid surface is available for the gas to adsorb to. This causes local small scale diffusion, which does not significantly contribute to the continuum flow.

Pressure diffusion
Pressure diffusion results from the separation of gases of different molecular weights under an external pressure gradient. Thus it is diffusion associated with advection. Pressure diffusion causes heavier molecules to diffuse towards regions of higher pressure and vice versa. Generally, the pressure difference is negligible at depths of less than 100m (Warrick, 2002), thus including methane oxidation systems, which are located near land surface.

3.3.3 Mechanical dispersion

Mechanical dispersion results from variation in fluid velocity at the pore scale. Higher flow velocities occur in the middle of the flow path, while lower flow velocities occur at the sides due to slip at the walls and other turbulence effects (Warrick, 2002). In most cases, dispersion is ignored as generally gas velocities are too small and the effects of diffusion are much greater than dispersion in the gas phase. Likewise, Scheutz et al. (2009) argue that dispersion is not critical for methane oxidation modelling, since dispersivity only becomes important at high flow rates, while in methane oxidation systems gas flow rates are kept low. Otherwise oxygen can not penetrate the soil and oxidation efficiency is low. For these reasons, mechanical dispersion is neglected in this thesis.

3.3.4 Ebullition

When the systems becomes nearly saturated, connectivity is impeded and the gas has two options: 1) Dissolve in the water, be transported by the water and return to gaseous state at a place with low concentration due to chemical equilibrium. 2) Ebullition (Scheutz et al., 2009), where gas pressure builds up until the gas flows through the water as bubbles. However, in methane oxidation systems a saturated state is to be avoided. Therefore, ebullition will only appear occasionally and is not taken into account for this thesis.

3.4 Gas transport models

Based upon these gas flow mechanisms multiple models were generated to simulate gas transport. This section elaborates on these models. However, for the reason explained above, none of them take pressure diffusion, mechanical dispersion or ebullition into account. Therefore in the rest of this thesis it is assumed that these three mechanisms can be disregarded.

3.4.1 Fick's law

The simplest model used to describe gas flow in porous media only includes molecular diffusion. Fick's law can only calculate the flux of one component relative to the rest of the mixture. For multicomponent gases, Wilke's modification can be used to calculate the flux of each component. Even though Wilke's modification allows for multicomponent gas, it does not take into account that for a multicomponent analysis the transport of one component depends upon the transport of all other components. Furthermore, as stated above, Fick's law and Wilke's modification only hold for equimolar gas mixtures under isothermal isobaric conditions and are therefore of limited use.

3.4.2 Advection & diffusion model

The diffusive process is described by Wilke's modification of Fick's law, see equations 3.13 to 3.15. The advective process is described by Darcy's law as in equation 3.12. The diffusive and advective terms can simply be added, since there is no direct coupling of terms in the equations; there is no advective term, ∇p, in the diffusion equation and no diffusive term, ∇c, in the advective equation, thus they are entirely independent (Mason and Malinauskas, 1983). The total flux of component i (N_i) can now be written as:

$$N_i = J_i + x_i N^V \tag{3.17}$$

This model holds for equimolar gas mixtures under isothermal conditions. Under these conditions, this model combines good accuracy with ease of implementation (Scheutz et al., 2009). Among others, Perera et al. (2002) and Stein et al. (2001) have adopted this approach.

3.4.3 Stefan-Maxwell equations

The Stefan-Maxwell equations combine advection, molecular diffusion and nonequimolar diffusion in one description. For the bulk molar flux this results in equation 3.18 and rewriting for component molar flux gives equation 3.19.

$$N = N^V + N^D \tag{3.18}$$

$$N_i = N_i^V + N_i^D = x_i N^V + J_i + x_i N^D = J_i + x_i(N^V + N^D) = J_i + x_i N \tag{3.19}$$

Including nonequimolar diffusion causes the component fluxes to depend on the bulk flux, whilst the bulk flux is the sum of all component fluxes. Therefore, in this formulation, they are all interdependent. This is

the key to describing multicomponent mixtures and enables components to flow against the concentration gradient. For an ideal gas, the Stefan-Maxwell equations can be written as follows (Warrick, 2002):

$$\sum \frac{x_i N_j - x_j N_i}{D_{ij}} = \frac{\nabla P_i}{RT} = \frac{P \nabla x_i}{RT} + \frac{x_i \nabla P}{RT} \tag{3.20}$$

The model does not take into account Knudsen diffusivity. Therefore, the Stefan-Maxwell equations do not take into account that the soil has grains which act as walls. This approach was adopted in various researches (Scheutz et al., 2009), among which de Visscher and van Cleemput (2003).

3.4.4 Dusty gas model

The dusty gas model combines advection, continuum diffusion (= molecular diffusion + nonequimolar diffusion + thermal diffusion + surface diffusion) and Knudsen diffusion (Mason and Malinauskas, 1983). As previously described, the diffusive and advective terms can be simply added, see Subsection 3.4.2 and the component fluxes are coupled similarly as in the Stefan-Maxwell equations. However, the diffusive term is now expanded with thermal, surface and Knudsen diffusion. The Knudsen diffusion allows for coupling of advection and diffusion. Including Knudsen diffusion leads to the assumption that there are walls in the system. Furthermore, the dusty gas model treats the porous medium as one component of the gas mixture, consisting of giant molecules held fixed in space. Thorstenson and Pollock (1989) derived equation 3.21, assuming no thermal diffusion (so temperature is steady) or surface diffusion:

$$\sum \frac{x_i N_j - x_j N_i}{D^*_{ij}} - \frac{N_i}{D^K_i} = \frac{P \nabla x_i}{RT} + \left(1 + \frac{\kappa P}{\mu D^K_i}\right) \frac{x_i \nabla P}{RT} \tag{3.21}$$

The total flux N_i is now a function of the total pressure gradient, the mole fraction gradient (thus concentration gradient) and all other total fluxes N_j. As a mathematical artefact of including Knudsen diffusion, the permeability (k) appears, showing the advection contribution to the fluxes (which is also present in the Stefan-Maxwell equations).

Piehler (2003) has used this model to predict the oxidation rates with a transient model. However, sometimes large errors can be observed e.g. underestimating by 50% of the measurements. Furthermore, the introduction of new parameters induces uncertainty.

3.4.5 Chemical potential model

This model is based on the chemical potential gradient, which might look entirely different on first sight, but is essentially similar to the other models. The chemical potential is given by the sum of the kinetic and potential energy, and as stated in the beginning of the chapter, energy gradients are caused by difference in pressure, concentration, temperature, etc. Chemical potential models can take advection, molecular diffusion and thermal diffusion into account. Multiple MOS researches have used this kind of model, most of them with their main focus on the kinetics of methane oxidation. Bogner et al. (1997) formulated such a model as follows:

$$N = D \nabla \mu \qquad \text{with} \qquad \mu = KE + PE \tag{3.22}$$

Where N is the net flux, D the chemical potential coefficient, μ the chemical potential, and KE and PE the kinetic and potential energy, respectively.

3.4.6 Comparison

Table 3.1 summarises the transport mechanisms taken into account by each model. The scope of this thesis also included actively pumped methane oxidation systems. Therefore, pressures differences are

encountered and advection should be taken into account. Solely Fick's law is then not sufficient. For reasons explained above, Knudsen diffusion and surface diffusion can be neglected for methane oxidation systems. As the Dusty gas model is not required, the introduction of large uncertainties by the use of numerous unknown parameters is omitted. In order to model the methane oxidation system, it is needed to coupling water flow and gas flow. From equation 3.10 it can be seen that the flow of water is expressed by a pressure gradient. Therefore, it is required to rewrite the above mentions equations to a form including gas pressure, see Section 3.6. For this multiphase problem focused on gas transport, a chemical potential model is thus not logical to choose. Lastly, Thorstenson and Pollock (1989) concluded that when viscous fluxes become dominant, the Stefan-Maxwell equations become inapplicable, due to the incomplete coupling of the advective and diffusive fluxes. Thus, the advection & diffusion model is chosen for the simulations of this thesis, see Subsection 3.4.2. The limitations of this model are outweighed by the advantage of relatively simple implementation.

Table 3.1: Comparison between gas flow models.

Model	Transport mechanisms					
	Advection	Molecular diffusion	Nonequimolar diffusion	Knudsen diffusion	Thermal diffusion	Surface diffusion
Fick's Law		√				
Advection & diffusion	√	√				
Stefan-Maxwell	√	√	√			
Dusty gas	√	√	√	√	√	√
Chemical potential	√	√			√	

3.5 Methane oxidation model

This thesis addresses the gas and water flow in a methane oxidation system. It does not focus on the methane oxidation process itself. However, as explained in Chapter 2 the methane oxidation process has an influence on the drivers of the system. Therefore, for the mere purpose of gas and water transport equation 2.1 is simplified to:

$$CH_4 + 2O_2 \longrightarrow CO_2 \tag{3.23}$$

Literature reviews (Sadasivam and Reddy, 2014; Cao and Staszewska, 2013; Scheutz et al., 2009) show that the reaction kinetics for methane oxidation in landfill cover soils is often described with a dual-substrate Michaelis-Menten model. Several researches that have adopted this oxidation model are Stein et al. (2001); Perera et al. (2002); de Visscher and van Cleemput (2003); de Visscher et al. (1999); Wilshusen et al. (2004). The dual-substrate model is formulated as:

$$R_{CH_4} = V_{max} \frac{[CH_4]}{K_{m,CH_4} + [CH_4]} \frac{[O_2]}{K_{m,O_2} + [O_2]} \tag{3.24}$$

With R_{CH_4} the reaction rate, V_{max} the maximum reaction rate, $[CH_4]$ and $[O_2]$ the methane and oxygen concentrations in the water, and K_{m,CH_4} and K_{m,O_2} the Michaelis-Menten constants. The corresponding reaction speed for oxygen and carbon dioxide are now $2R_{CH_4}$ and $-R_{CH_4}$ times the reaction speed of methane, respectively.

The methane and oxygen concentrations in the water are in equilibrium with their partial gas pressures. This can be expressed by Henry's law (Sander, 2014), which is shown in equation 3.25 for methane. The same expression can be written for the oxygen concentration.

$$[CH_4] = H^{cp}_{CH_4} P_{CH_4} \tag{3.25}$$

Where $[CH_4]$ is the concentration of methane in the water phase, $H^{cp}_{CH_4}$ is Henry's constant for methane and P_{CH_4} is the partial gas pressure for methane.

3.6 Mass balance

To couple the water phase, the multi-component gas phase and the methane oxidation reaction, the law of mass conservation is applied. This law dictates that the mass inside a volume can only change due to flow in or out through the sides, or due to a sink or source. For a compressible phase, this is similar to a molecular balance. For a incompressible phase, this is similar to both a molecular balance and a volumetric balance. Since both occur in the methane oxidation system, a mass balance in the form of a molecular balance is chosen. This can be formulated for the advection & diffusion model as:

$$\frac{dc_T}{dt} = -\nabla \cdot (J) - \nabla \cdot (qc_T) - R \tag{3.26}$$

Where c_T is the number of moles per volume, J is the diffusive flux, q the advective flux and R the methane oxidation reaction term. This creates a dynamic model, which allows for the methanotrophic activity to be a function of the concentrations of that time, instead of assuming a steady rate.

Rewriting the molecular balances for the water and all four gas components into a formulation based upon partial pressures allows for coupling of the phases and components. This is implemented in Chapter 9.

Part II

Laboratory studies

4 Introduction to laboratory studies

Chapter 2 elaborated on the importance of gas transport for the efficiency of the methane oxidation system. The effective permeability is influenced by the air filled porosity, connectivity, and tortuosity, which in turn depend on the compaction level, the texture and the water content of the soil. Changing the compaction level mimics the construction practice, where soil is compacted by bulldozers driving over a few times. The importance of compaction in relation to the effective permeability is shown in literature Beghardt et al. (2009); Scheutz et al. (2009); Geck (2017). The influence of the texture of a soil is important for making the right material choices. And lastly, changing the water content mimics the seasonal variation in saturation. This concerns three of the research questions:

- How does the effective permeability of a soil depend on the compaction level of that soil?
- How does the effective permeability of a soil depend on the physical properties of that soil?
- How do the hydraulic conditions influence the effective permeability of a soil?

To answer these questions two laboratory experiments were designed. These are pressure loss permeability tests, similar to the falling head permeability test, but then designed for air flow. By doing so, the soil sample is allowed to be unsaturated. This creates the opportunity to research the effect of the water saturation on the effective permeability. As explained in Chapter 3, the effective permeability for air is described as the intrinsic permeability of the soil times the relative permeability factor, see equation 4.1. The intrinsic permeability is influenced by the texture of the soil and the compaction level. The relative permeability factor is influenced by the type of soil, the compaction level and the hydraulic conditions.

$$\kappa_{eff} = \kappa k_r \tag{4.1}$$

4.1 Hypothesis

The first experiment is designed to asses the effect of compaction level on the effective permeability of a soil. If the pores are coarser, there is less contact between the grains, resulting in less resistance when compacting. Compaction will, thus, have the largest effect on the coarse pores, as is shown in Figure 4.1. However, coarse pores contribute more to the effective gas permeability than the fine pores. Therefore, initial compaction is expected to have a large influence on the permeability. However, upon further compaction, the fraction of coarse pores is already decreased and compaction will lose its influence.

The second experiment is designed to asses the effect of different water contents, and thus how the hydraulic conditions influence the effective permeability of the soil. Due to the capillarity the finer pores are filled first. Adding water will thus clog the smaller pores, while the larger voids dominate the effective permeability. Therefore, it is expected that adding water will not influence the effective permeability much up to a certain point, where the gas filled pores are hardly connected and the gas paths become very

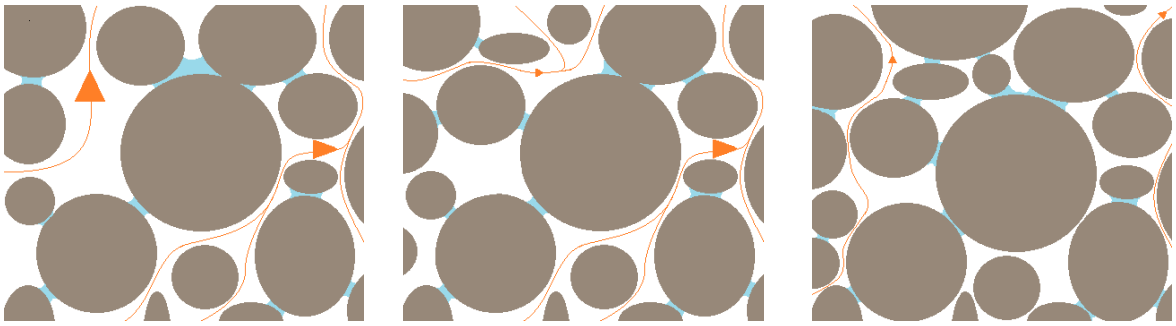

(a) (b) (c)

Figure 4.1: Schematic representation of the impact of compaction on gas transport through soils.

tortuous. After this point the influence will be significant. This is shown in Figure 4.2 and also observed by Cabral et al. (2004) for diffusion.

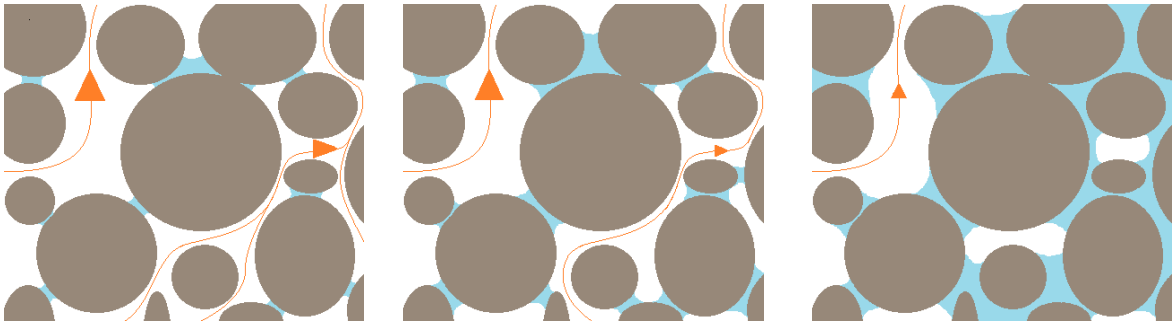

(a) (b) (c)

Figure 4.2: Schematic representation of the impact of saturation on gas transport through soils.

Both experiments are performed on two different soils, in order to asses the effect of the physical properties of the soil on the effective permeability. The physical properties are expected to influence the compaction experiment, since the particle size distribution will determine the pore sizes and thus the share of coarse pores. Furthermore, they will determine the ability to retain water and is thus expected to influence the connectivity and tortuosity of the soil.

A detailed explanation of the experiments is found in Chapter 5. The results of the experiments as well as their discussion are presented in Chapter 6. The conclusions on the laboratory experiments are presented in Chapter 7.

5 Materials and methods

This chapter describes the materials and methods that have been used to perform the experiments. Firstly the materials and their key properties are discussed. Secondly the implemented methods are explained.

5.1 Materials

5.1.1 Soils

Three different soils were used for the laboratory experiments of this thesis: two sands and one gravel. Below their key soil properties are elaborated upon and shown in Table 5.1.

The selected sands are currently used as methane oxidation layer material at two different landfills. One site is located near Hamburg, Germany, and is operated by the Hamburg Port Authority. The corresponding sand will be referred to as sand 1. The other site is located in Wieringermeer, the Netherlands, and is operated by Afvalzorg Deponie B.V.. The corresponding sand will be referred to as sand 2. These sands were selected, since they are already proven adequate as methane oxidation layer material. Both are sands, thus a high porosity is obtained for the LFG and oxygen transport. However, sand 2 is slightly

Table 5.1: Soil properties for the sands and gravel used in the experiments

Soil	**Sand 1**	**Sand 2**	**Gravel**	**Unit**
Clay	2.6	8.8	0	% dw
Silt	18.3	7.2	1.8	% dw
Sand	79.1	82.4	32.0	% dw
Coarse	15.87	3.42	-	% dw sand
Medium	27.88	16.38	-	% dw sand
Fine	45.22	75.21	-	% dw sand
Very fine	11.02	4.99	-	% dw sand
Gravel	0	1.6	66.2	% dw
Organic content	1.1	1.34	0	% dw
$CaCO_3$	0	5.5	0	% dw
German texture class[a]	Su2	St2	Gs	-
USDA texture class [b]	LS	LFS	SG	-
Proctor/dry density[c]	1.90	1.76	1.60	g/cm^3

[a] *Su2 = slightly silty sand, St2 = slightly clayey sand, Gs3 = sandy gravel*
[b] *LS = loamy sand, LFS = loamy fine sand, SG = sandy gravel (Bodenkunde, 2005)*
[C] *Proctor density for Sand 1 and 2; Dry density for Gravel (Benham et al., 2009)*

clayey with some gravel and calcium carbonate, while sand 1 is slightly silty with no gravel or calcium carbonate at all. Furthermore sand 1 is slightly coarser than sand 2. Additionally, the proctor densities differ significantly. The soil fractions were provided by the operators. The sand fractions and proctor densities were obtained with a sieving test and a proctor test, as described in Section 5.2. The results of these tests can be found in Appendices B.1 and B.2.

The gravel was obtained from the Wieringermeer site and is used as gas distribution layer. It is a well sorted fine sandy gravel. Since gravel is a coarse material, it is assumed that no (significant) compaction takes place upon loading. Therefore not the proctor density, but simply the dry density of the gravel was determined. The soil fractions of the gravel were obtained by a sieving test.

5.1.2 Columns

The columns were constructed from PVC tubes with an inner diameter of 151mm. They were cut at a length of 1m for each column. The bottoms were sealed by gluing a PVC cap around the bottom. A special gas tight tube connection system, was connected to the bottom of the column at a height of $1cm$.

5.2 Methods

Several laboratory tests were performed on the materials. Table 5.2 depicts which tests were performed on which soil. Firstly, the sieving and proctor tests were performed on the soils, according to the USDA Standard (USDA MO5 2009) and the British Standard (BS 1377-4), respectively. More detail about these tests and their results can be found in Appendices B.1 and B.2. Secondly, two samples were prepared per sand type at approximately $85\%D_{pr}$. Of these samples the drying water retention curve of the methane oxidation layer soil was determined using the HYPROP apparatus (HYPROP-UMS, 2013). From disturbed sand samples, another five data points were obtained with a WP4C Dewpoint PotentiaMeter, manufactured by Decagon Devices. One other point was obtained by back-calculating the saturated water content from the bulk density and gravimetric water content. These water retention curves and 6 additional data points were fitted for the Brooks and Corey (BC) model with DREAM (DiffeRential Evolution Adaptive Metropolis), as implemented in Matlab by van Turnhout (2017). Based upon these BC curves the sands were prepared for the column experiments (Subsection 5.2.2 and Appendix B.3). Subsequently, the column experiments were performed. The rest of this chapter will elaborate upon the column tests. Finally, the water retention curves were determined for each compaction level in the same way as explained above.

Table 5.2: Laboratory tests performed on the sands and gravel

Tests / Soil	Sieving test	Proctor test	HYPROP test	Dewpoint meter test	Column test
Sand 1	√	√	√	√	√
Sand 2	√	√	√	√	√
Gravel	√				√

5.2.1 Test set-up

The set-up is shown schematically in Figure 5.1. The tank has a volume of $0.514m^3$ and contains air. Extra air can be pumped in with a compressor, during which valve 1 (#5 in Figure 5.1) is open and valve 2 (#6 in Figure 5.1) is closed. The tank pressure can be regulated this way. The tank pressure is measured with a pressure sensor ranging from 0 to $100hPa$, connected to the tank via tubes with an inner diameter of $1cm$. The pressure sensor is connected to a data logger, which keeps track of the time. The data logger forwards the pressure measurements and corresponding time to a computer, where the data is stored.

During the test, valve 1 is closed and valve 2 is opened. The pressurised air can now escape the tank via the column. This contains a layer of gravel to ensure homogeneous spread of the airflow over the base area, on top of which the soil sample to be tested is placed. The column has an inner diameter of $15.2cm$ and a height of $100cm$. The gravel layer is $4-7cm$ high to ensure that the gravel reaches above the inlet. The soil sample has a height of $\pm 90cm$.

The whole set-up was tested to be air tight.

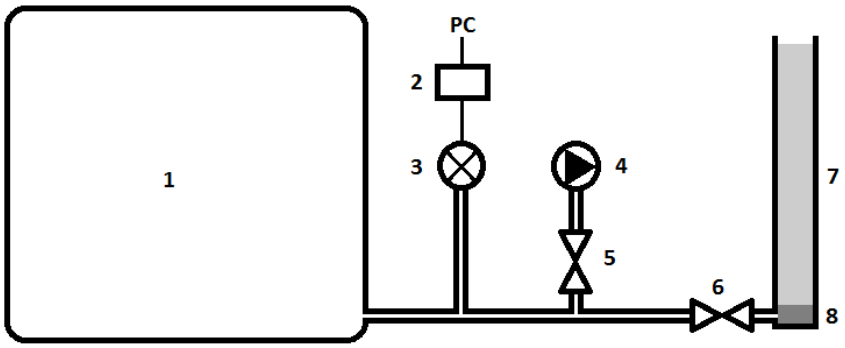

Figure 5.1: Schematic representation of the test set-up: (1) tank containing (pressurised) air; (2) data logger; (3) pressure sensor; (4) compressor; (5) valve 1, open when pressurising the tank, closed during testing; (6) valve 2, closed when pressurising the tank, open during testing; (7) soil sample; (8) gravel layer.

5.2.2 Sample preparation

Gravel is assumed to drain immediately, therefore the gravel was tested air dried. Furthermore gravel can hardly be compacted. Thus, only one column was prepared by simply pouring $90cm$ of gravel in the column without any further compaction. A completely empty column was tested as a blank, to ensure the the permeability of the gravel was tested and not the permeability of the test set-up itself.

The preparation of the sands started with attaining the intended water contents. The different water contents were selected based on certain capillary pressures, relating to certain pores sizes. Often used capillary pressures are: The pressure at field capacity; $60hPa$. This is the pressure at which all the free water is drained under gravity. The pressure at $300hPa$, where the coarse pores (pore diameter $> 10\mu m$) are drained, the medium and fine pores still contain water. The pressure at $1000hPa$, a common pressure to plot in water retention curves. And lastly, the permanent wilting point at $15000hPa$. At this point plants can no longer take-up water from the soil. Medium pores are now also drained and only the fine pores (pore diameter $< 0.2\mu m$) are still filled with water. Methane oxidation systems are not commonly situated in climates where soils get dryer than this point. Based upon the aforementioned capillary pressures, the following 5 capillary pressures were selected for the experiments:

Table 5.3: Capillary pressures for experiment design.

Capillary pressure	**Reason**
$120hPa$	2x field capacity pressure, to avoid flowing water during the experiment
$300hPa$	coarse pores drained
$1000hPa$	common point of both experiments
$3000hPa$	to ensure good spread in water contents
$15000hPa$	permanent wilting point

The water retention curves obtained for approximately $85\%D_{pr}$ (see Appendix B) give the volumetric water contents corresponding to these capillary pressures. These are the intended water contents for the

test and can be found in Table 5.4. The gravimetric water content of the soil was determined by taking three samples and drying them in the oven. Subsequently the soil was dried or moisturised and the gravimetric water content was determined again. This was repeated until the intended water contents were (approximately) reached.

Table 5.4: Intended water contents and compaction levels for the experiments.

Soil 1

Column	1	2	3	4	5	6	7	8	9
Capillary pressure $[hPa]$	1000	1000	1000	1000	1000	15000	3000	300	120
Water content $[\%V]$	12.35	12.35	12.35	12.35	12.35	5.18	8.59	18.58	25.49
Compaction level $[\%D_{pr}]$	75	80	85	90	95	85	85	85	85

Soil 2

Column	1	2	3	4	5	6	7	8	9
Capillary pressure $[hPa]$	1000	1000	1000	1000	1000	15000	3000	300	120
Water content $[\%V]$	20.47	20.47	20.47	20.47	20.47	12.49	16.74	25.53	31.24
Compaction level $[\%D_{pr}]$	75	80	85	90	95	85	85	85	85

Next, the columns were prepared. For both sand types, 9 columns were constructed. All 18 columns were constructed in a similar way. First a gravel layer of $4-7cm$ height was poured in, to establish good air flow via the inlet into the column and to ensure homogeneous spread over the base area of the column. Subsequently, the sand sample was constructed in 9 layers of $10cm$, so a sample height of $90cm$ in total. This was done in the following order. Firstly, the amount of soil (in kg) that should go into $10cm$ of sample height was determined, based upon the intended water content and bulk density. Secondly, this amount was poured in to the column and compacted. Compaction was achieved with a weight of $4.936kg$ falling down on a base plate with a diameter and weight of $15.1cm$ and $3.359kg$, respectively. After compaction of one layer, the top centimetre of that layer was scraped loose with a fork to smooth the boundary between two layers. After which, the soil for the next layer was poured in and compacted. This was repeated until all $90cm$ of sample was constructed. The bulk density was determined as a mean density over the whole $90cm$ of sample. The bulk density of the soils will be expressed as percentage of the Proctor density $[\%D_{pr}]$, which allows for comparing these two soils with very different compaction behaviour.

For construction purpose, the compaction of the columns can be compared to field compaction with a bulldozer. It is important to notice that dropping 100 times $1kg$ on a soil has a different effect than dropping 1 time $100kg$ on that soil, since every time you let the $1kg$ fall it will have less effect than the time before. The same can be said about height; dropping the falling weight 100 times from 1cm height, will not be the same as letting it fall once from 1m. Therefore, the effective energy must be taken into account instead of the total energy to compare the compaction energy for construction of the columns to construction in practice. The effective energy was calculated with equation 5.1, see Appendix B.4 for the derivation. For construction with a bulldozer, this means that the mechanical work done by settlement of the bulldozer is equal to the effective energy. This settlement can be calculated based upon the bulk density change of the sand. From visual observation a bulk density of $50\%D_{pr}$ was estimated for the sand, after solely pouring the sand in the column. The needed ground pressure $[kg/cm^2]$ of the bulldozer driver over one construction layer of $10cm$ can now be back-calculated with equation 5.2.

$$E_{eff} = \frac{n}{\sum_{a=1}^{n} a^{-1.3}} mgh_{fall} \tag{5.1}$$

$$P_{ground} = \frac{E_{eff}}{Ag\left(\frac{D_{pr,final}}{D_{pr,initial}} - 1\right) h_{construction}} \tag{5.2}$$

Where E_{eff} is the effective energy exerted on the top area of the sample per construction layer $[J]$, n the amount of drops $[-]$, m the mass of the falling weight $[kg]$, g the gravitational acceleration $[m/s^2]$, h_{fall} the fall height $[m]$. A is the base area of the column cm. $D_{pr,final}$ and $D_{pr,initial}$ are the final and initial bulk densities of sand $[\%D_{pr}]$. Lastly, $h_{construction}$ is the height of the construction layer, which in this case is $0.1m$.

5.2.3 Measurements

The tank pressure is measured relative to the atmospheric pressure by a pressure meter with a range of $0 - 100hPa$. The pressure and time are logged every second. The tests started at $100hPa$ and were stopped when the pressure reached $5hPa$. All columns were tested in threefold.

The pressure meter is calibrated with a device consisting of one column filled with water, see Figure 5.2a. The bottom of the column is connected with the pressure meter via a tube. The difference in water level $[cm]$ is now the water pressure $[cm = hPa]$ the pressure sensor should read. The results are shown in Figure 5.2b, where the actual pressure is the water level difference. The data can be fitted with a linear equation as indicated in the figure.

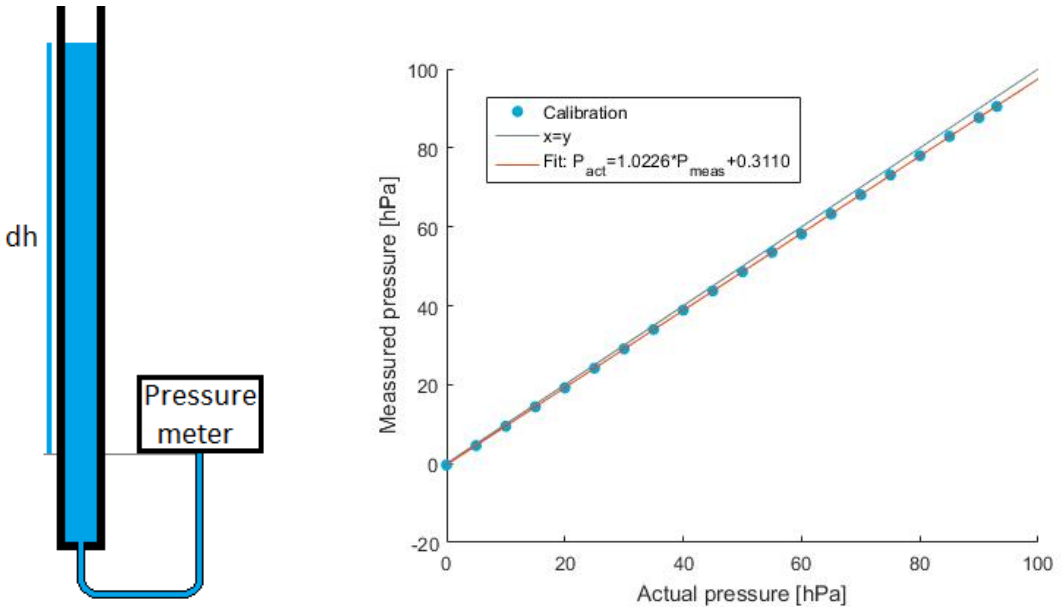

(a) Calibration device

(b) Calibration results

Figure 5.2: Calibration of the pressure sensor

5.2.4 Data evaluation

Firstly, the measured pressures ($P_{measured}$) are rewritten into the actual pressures (P) via the following formula, obtained with the calibration:

$$P = 1.0226P_{measured} + 0.3110 \tag{5.3}$$

Secondly, the measured pressure is not only decreasing due to outflow via the column, but also via a small leakage, which was tested by closing all valves. The data showed exponential decay, see Figures 5.3 and 5.4. For exponential decay, formula 5.4 holds. This means that λ (the decay factor) measured is the λ of flux through the soil column plus the λ of the leakage. Thus, to take into account the leakage, the time is recalculated via formula 5.5. For the full derivation, see Appendix B.5. The duration of the leakage test was found to be $t_{leakage,end} = 118611s$ according to exponential fit.

$$P = P_0 e^{-\lambda t} \qquad \text{with} \qquad \frac{dP}{dt} = -\lambda P \tag{5.4}$$

$$t = t_{measured} \frac{1}{1 - \frac{t_{measured,end}}{t_{leakage,end}}} \tag{5.5}$$

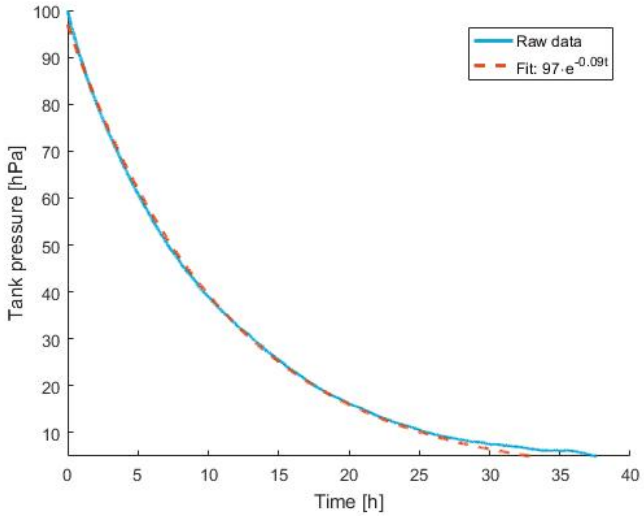

Figure 5.3: Change of pressure over time in relation to leakage; all valves are closed.

Thirdly, the actual test: an effective permeability value for each soil column must be obtained to interpret the effects of compaction and water content on the permeability. Therefore an equation is needed that describes the column experiment. Such an equation is derived by equating the number of moles flowing out of the tank to the number of moles flowing into the soil column. The number of moles flowing out of the tank can be described by the ideal gas law, see the left hand side of equation 5.6. The experiments are performed with air, which means that the flow is solely driven by advection. From Chapter 3 it follows that the flow can be described by Darcy's law, see equation 3.12. It thus represents the number of moles flowing into the soil column, see the right hand side of equation 5.6. Rewriting this to a form where pressure is a function of time ($P = f(t)$) gives equation 5.7. For the full derivation, see Appendix B.6

$$\frac{V}{RT}\frac{dP}{dt} = -\frac{A}{L}\frac{\kappa}{\mu}\frac{1}{RT}P\left(P + P_{atm}\right) \tag{5.6}$$

$$P = \left(\frac{P_{atm}}{\frac{P_0 + P_{atm}}{P_0} - e^{-Ct}}\right) e^{-Ct} \qquad \text{with} \qquad C = P_{atm}\frac{A}{VL}\frac{\kappa_{eff}}{\mu} \tag{5.7}$$

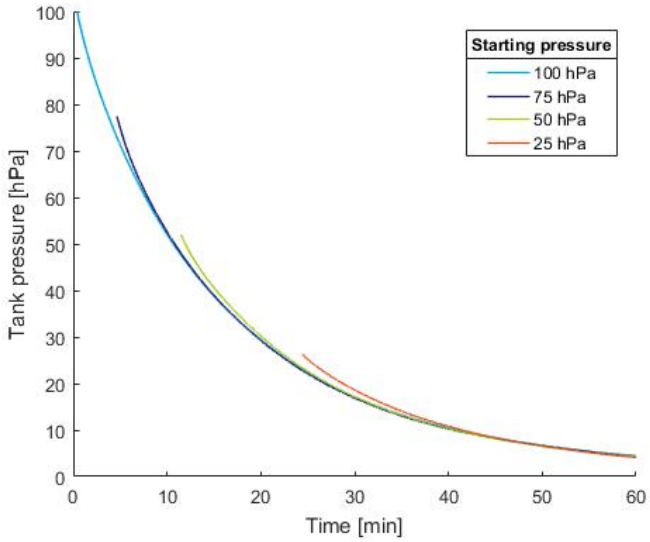

Figure 5.4: Change of pressure over time for different starting pressures.

Where P and P_0 are the tank and starting tank pressures relative to the atmospheric pressure, and P_{atm} is the absolute atmospheric pressure $[Pa]$. A is the base area of the column $[m^2]$ and dL is the path length of the flow through the soil tested $[m]$. V is the volume of the tank $[m^3]$. R and T are the universal gas constant $[J/Kmol]$ and the room temperature $[K]$. μ is the dynamic viscosity of air at room temperature $[sPa]$. κ_{eff} is the effective permeability $[m^2]$ and is the parameter to be determined.

Since all columns are tested in threefold, one representative κ_{eff} is found by fitting all three data sets simultaneously between $5 - 80hPa$ with DREAM as implemented in Matlab by van Turnhout (2017). This one value is assumed to be representative for the soil tested, since the permeability of the gravel and the test set-up are much higher and thus will not limit the flow. The fit is fitted up to $80hPa$ in stead of $100hPa$, since Figure 5.4 shows that $\pm 20hPa$ is required for each the test to converge to the same line, regardless of the starting pressure. The values that are used for fitting are shown in Table 5.5.

Table 5.5: Parameter values used for obtaining the effective permeability with the analytical fit.

Parameter	**Value**	**Unit**
t	Measured	s
dP_a	Measured	Pa
P_{atm}	101325	Pa
μ_a	$18.13 \cdot 10^{-6}$	$Pa \cdot s$
V_T	0.514	m^3
A	0.018	m^2
dL_{set-up}	1.42	m
dL_{soil}	± 0.9	m
κ_{eff}	Optimised (one value for all 3 tests)	m^2
P_0	Optimised (one value for each tests)	Pa

Validity
Darcy's law only holds for laminar flow. Reynolds number is used for distinction between laminar and turbulent flow. Darcy's law is valid as long as the Reynolds number does not exceed 2000. According to Bear and Cheng (2010) the Reynolds number for flow through porous media can be calculated by:

$$Re = q\frac{D}{\nu} \tag{5.8}$$

Where q is the effective velocity $[m/s]$, D the mean grain diameter $[m]$, and ν the fluid's kinematic viscosity $[m^2/s]$. The 'worst case' values for these parameters for this thesis are filled in below (the beginning of the gravel test). A soil can be seen as a system of pipes. In pipes the transition from laminar to turbulent flow is about 2000. The Reynolds number is well below 2000, thus Darcy's law is valid for the laboratory tests.

$$Re = \frac{\kappa k_r w}{\mu_{air}}\nabla P\frac{D}{\nu_{air}} = \frac{2\cdot 10^{-10}}{2\cdot 10^{-5}}\frac{10000}{0.9}\frac{0.01}{15\cdot 10^{-6}} = 74$$

Besides that, the air is assumed to be an ideal gas. Therefore, the ideal gas law should be checked for validity as well. The ideal gas law is valid when the pressures are below the critical pressure and the temperature is above the critical temperature. For air these are $38bar$ and $-141°C$ (Engineering Toolbox URL, 2018), respectively. The tests were performed at $1.1bar$ and $21°C$. Thus the ideal gas law is valid.

Sensitivity
A sensitivity analysis was performed to check the influence of change of these parameters on the obtained effective permeability. The analysis was executed on the atmospheric pressure, the dynamic viscosity of air, the volume of the tank, the base area of the column and the length of the sand sample.

6 Experiment results and discussion

This Chapter elaborates upon the results of the laboratory work. All the data shown are already adjusted according to equations 5.4 and 5.5.

6.1 Sensitivity analysis

The sensitivity analysis is performed with the experimental data of column 3 of sand 1, as can be seen in Figure 6.1. The base case is the fit to this data according to the values stated in Table 5.5. Fitting was performed with 10^5 iterations. Firstly, the sensitivity of DREAM was determined by running the base case 10 times. This gave a mean and standard deviation of $4.1445 \cdot 10^{-12} m^2$ and $7.2689 \cdot 10^{-14} m^2$, respectively. Therefore the spread (6 times the standard deviation) is $4.3613 \cdot 10^{-13} m^2$. Accordingly, the effective permeabilities (in the order of 10^{-12} to 10^{-11}) are rounded to 1 significant digit. This is adopted in the rest of the report.

The atmospheric pressure as determined in Table 5.5 is changed by 1, 10, 100 and -10%, each one run 5 times. The rest of the parameters has a clearly defined relation to the permeability, due to the formulation of the analytical fit, see Equation 5.7. The effects on the effective permeability can found in Table 6.1. It can be seen that the dynamic viscosity, the tank volume, the sample length and base area all have the same effect on the effective permeability. If all the parameters differ maximal from the used parameters, see the accuracy, this will give a deviation of the effective permeability of 7%. However, this deviation is within the spread of the DREAM fit. Therefore, rounding the effective permeabilities to 1 significant digit will suffice with an uncertainty of ± 1 in the order of that magnitude.

Table 6.1: Results of the sensitivity analyse of the analytical fit.

Base case

Iterations	**Mean k**	**Standard deviation**	**Rounded k**
10^5	$4.1445 \cdot 10^{-12} m^2$	$7.2689 \cdot 10^{-14} m^2$	$4 \cdot 10{-}12 m^2$

Parameters

Parameter	**Change of parameter**	**(Mean) change in k**	**Accuracy or parameter**
P_{atm}	$+1\%$	-2.5592%	$\pm 20 hPa \rightarrow \pm 2.0\%$
	$+10\%$	-6.4065%	
	$+100\%$	-47.9769%	
	-10%	$+9.0813\%$	
μ	$+10\%$	$+10\%$	$\pm 9 \cdot 10^{-8} Pa \cdot s \rightarrow \pm 0.5\%$
V	$+10\%$	$+10\%$	$\pm 0.014 m^3 \rightarrow \pm 2.7\%$
A	$+10\%$	-9.09%	$\pm 2 cm^2 \rightarrow \pm 1.1\%$
L	$+10\%$	$+10\%$	$\pm 5 mm \rightarrow \pm 0.6\%$

6.2 Performance of analytical fit

The experimental data and according fits for column 3 of sand 1 are shown in Figure 6.1. In the left graph all three tests are shown. The pressure loss curves are almost identical, thus hardly distinguishable in the graph. This mean the test is highly reproducible. In the three graphs on the right, each test is shown together with its corresponding fit. All fits show a similar trend: in the beginning and at the end of the test the fit underestimates the tank pressure, while in between the slope of the fit is in accordance with the experimental data. Or better, in the beginning the slope of the fit is not steep enough, while in the end the slope is too steep. Thus, the fit does not get curved enough to fit the experimental data exactly. When fitted only between $60 - 80hPa$ and between $5 - 25hPa$, the obtained effective permeabilities are $4.5598 \cdot 10^{-12}m^2$ and $3.6843 \cdot 10^{-12}m^2$, respectively. This is $\pm 10\%$ deviation from the fit for $5 - 80hPa$, shown in the Figure below. Similar differences between the experimental data and their fits are observed at all other tests, including the tests for the gravel and the test set-up. All their data and fits can be found in Appendix B.7.

Possible reasons for the deviation in curvature between the fit and the actual test are: 1) The water content might not be uniformly distributed over the column, because of hydrostatic equilibrium. 2) Darcy's law does not correctly represent the flow through the column. 3) The air is not an ideal gas. 4) The leakage might be taken into account wrongly. By back-calculating the time, the tests are assumed to behave like exponential decay, which is roughly the case, but not exactly. Option 1 was proven not to be the problem by the model in Part 3. The other options could be further investigated.

Overall, the fit shows a good conformity with the experimental data with a root mean squared error of $RMSE = 1.2118hPa$. Since we fit in a range of $75hPa$, the error is below 2% of the range and is therefore acceptable.

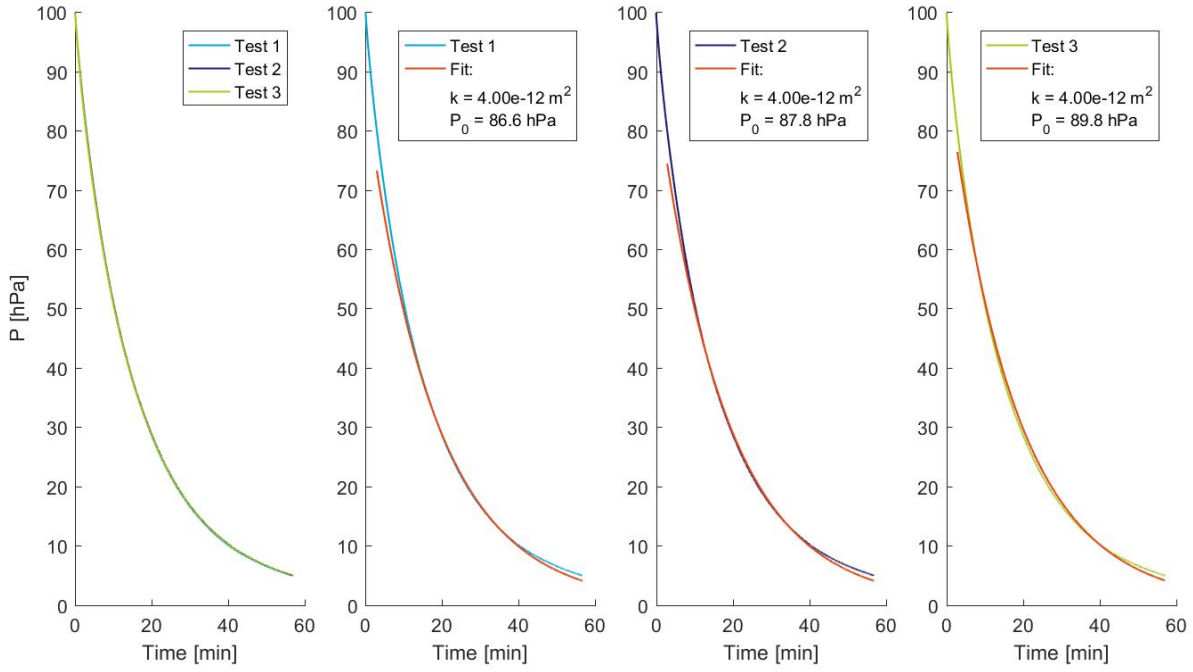

Figure 6.1: Change of pressure over time in relation to compaction level, sand 1, column 3 $85.04\%D_{pr}$, $12.34\%Vwater$. Each pressure loss test is performed in threefold (see 1, 2, 3 in legend). The red line represents the fit, fitted between 5 and $80hPa$.

6.3 Permeability of the gravel and of the experimental set-up

The results for pressure loss tests on the gravel and on the bare test set-up (without soil) are shown in Figure 6.2. The fitted curves can be found in Appendix B.7. The obtained effective permeabilities are $1.5625 \cdot 10^{-9} m^2$ for the test set-up and $2.0078 \cdot 10^{-10} m^2$ for the gravel. The permeability of the test set-up is 10 times larger than of the gravel, therefore the test set-up will not have limited the flow during the gravel test. Furthermore, the gravel's permeability is in the order of 10 to 100 times larger than the obtained sands permeabilities, which are shown in Sections 6.4 and 6.5. Therefore both the set-up and the gravel will not have limited the flow when the sand columns were tested. The gravel's permeability is in agreement with values found in literature, where the permeabilities for pure gravel range from 10^{-7} to $10^{-10} m^2$ (Warrick, 2002; Lu and Likos, 2004) and for gravel mixtures from 10^{-9} to $10^{-12} m^2$ (Warrick, 2002).

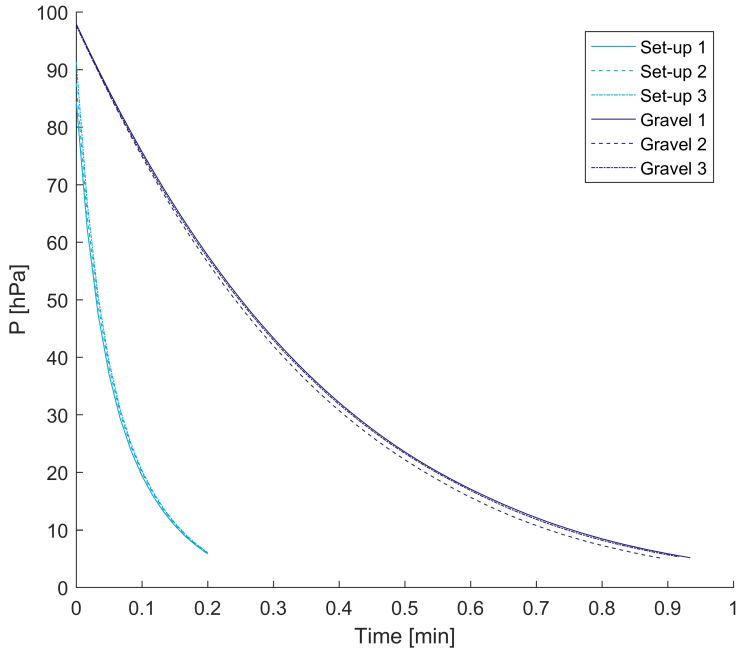

Figure 6.2: Change of pressure over time in relation to compaction level, gravel and experimental set-up. Each pressure loss test is performed in threefold (see 1, 2, 3 in legend).

6.4 Experiment 1: variable compaction level

For the first experiment five columns were constructed for both sands under different compaction levels of approximately 75, 80, 85, 90 and 95%D_{pr}. The details of these 10 columns are presented in Table 6.2. The fall height and corresponding number of drops changed per column. Slight variations in number of drops were found between the construction layers, therefore the average numbers of drops per construction layer are shown here. The effective compaction energy was calculated with Equation 5.1. The ground pressure of a bulldozer driving over a 10cm construction layer once was back-calculated with Equation 5.2. These preparations resulted in the compaction levels and water contents as shown in the table. The air content was back-calculated, assuming a particle density of $2.65 g/cm^3$. The effective permeabilities were obtained by fitting equation 5.7 to the experimental data and are shown in Table 6.2 as well. The experimental data can be found in Figures 6.4 and 6.5. The full data curves and corresponding fits are presented in Appendix B.7.

Table 6.2: Details on the compaction procedure and obtained physical properties for the compaction experiment.

Sand 1

Column		1	2	3	4	5
Fall height	$[cm]$	10	20	50	90	107
Number of drops	$[-]$	11	12	25	17	55
Effective compaction energy	$[kJ]$	23	49	227	294	972
Ground pressure	$[kg/cm^2]$	0.26	0.47	1.84	2.17	6.31
Compaction level	$[\%D_{pr}]$	75.06	79.79	85.04	88.55	93.82
Water content	$[\%V]$	12.54	12.33	12.34	12.37	12.41
Air content	$[\%V]$	33.64	30.47	26.69	24.15	20.33
Effective permeability	$[m^2]$	$3 \cdot 10^{-11}$	$1 \cdot 10^{-11}$	$4 \cdot 10^{-12}$	$2 \cdot 10^{-12}$	$1 \cdot 10^{-12}$

Sand 2

Column		1	2	3	4	5
Fall height	$[cm]$	10	15	15	50	90
Number of drops	$[-]$	7	12	33	34	54
Effective compaction energy	$[kJ]$	16	37	87	296	804
Ground pressure	$[kg/cm^2]$	0.19	0.35	0.70	2.13	5.08
Compaction level	$[\%D_{pr}]$	74.56	79.52	84.99	89.53	95.06
Water content	$[\%V]$	20.51	20.12	20.31	20.68	19.35
Air content	$[\%V]$	29.97	27.07	23.25	19.86	17.52
Effective permeability	$[m^2]$	$2 \cdot 10^{-11}$	$1 \cdot 10^{-11}$	$6 \cdot 10^{-12}$	$3 \cdot 10^{-12}$	$2 \cdot 10^{-12}$

Table 6.2 shows that the intended compaction levels and water contents are approached quite closely. Only columns 4 and 5 of sand 1 show some deviation of the intended compaction levels and column 5 of sand 2 shows some deviation of the intended water content. To visualise the differences between the columns, the volumetric contents are shown in Figure 6.3. Furthermore, from the table can be concluded that higher compaction levels need exponentially more compaction energy. Logically, this is also seen in the ground pressure needed for the bulldozer for compaction in one drive over. As a reference: a Caterpillar D6N LGP has a ground pressure of $0.327 kg/cm^2$ and a human of $90kg$ with shoe size 45 has a ground pressure of $0.529 kg/cm^2$ (Internal document provided by Afvalzorg Deponie B.V.).

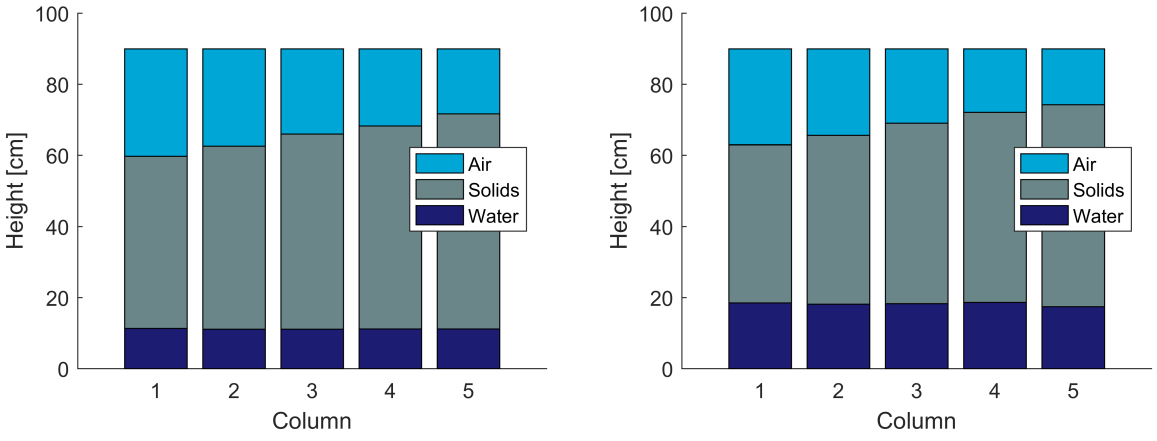

(a) Sand 1

(b) Sand 2

Figure 6.3: Visualisation of volumetric contents for the compaction experiment.

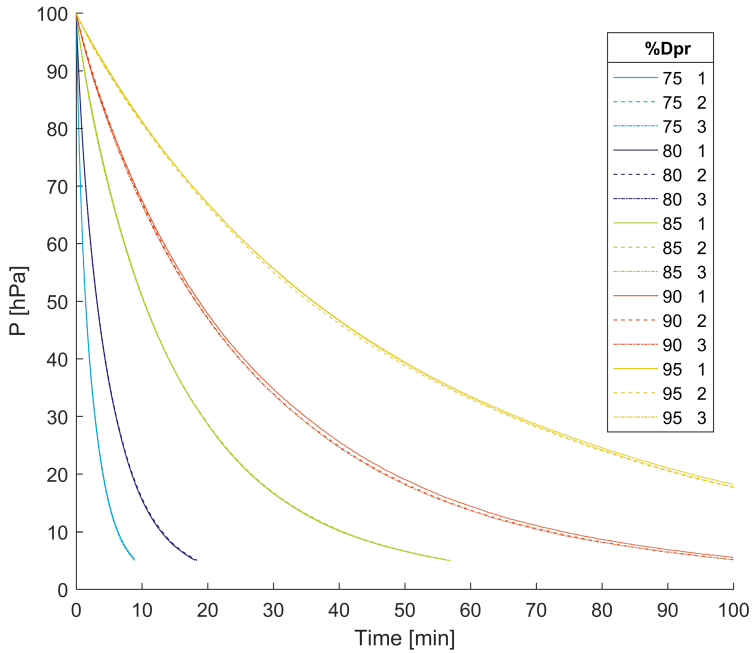

Figure 6.4: Change of pressure over time in relation to compaction level, sand 1. Each pressure loss test is performed in threefold (see 1, 2, 3 in legend).

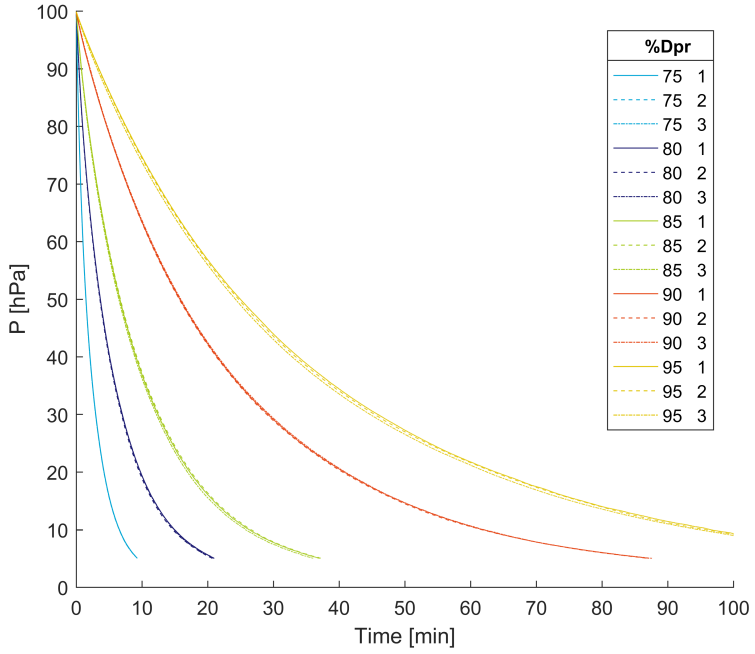

Figure 6.5: Change of pressure over time in relation to compaction level, sand 2. Each pressure loss test is performed in threefold (see 1, 2, 3 in legend).

When looking at the experimental data in Figures 6.4 and 6.5, both sands clearly show the same trend. An increase in compaction level leads to an increase in the time required for equilibrating the pressure in the tank with the atmospheric pressure, which means a decrease in the effective permeability. To analyse this trend, the effective permeability is plotted against the compaction level, see Figures 6.6. The effective permeability shows a exponential decay when density increases. However, sand 1 seems to have a slightly steeper decay than sand 2. This can be explained by the slight variations in water content. Therefore, the effective permeability is also plotted against the air filled porosity, which takes into account the water content, see Figure 6.7. The figure shows that the effective permeability of both sands depends exponentially on the air filled porosity. This is in accordance with Gebert et al. (2009), who also showed there is a log-linear relationship.

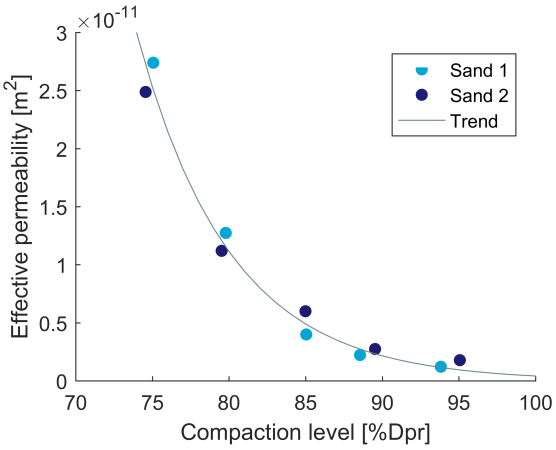

Figure 6.6: Relationship between compaction level and effective permeability

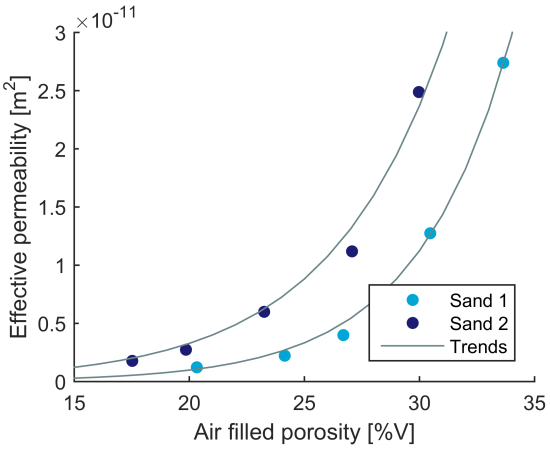

Figure 6.7: Relationship between air filled porosity and effective permeability

Furthermore, Figure 6.7 shows that there is a discrepancy between the two sands. Sand 1 has a lower effective permeability than sand 2 at similar air filled air filled porosities. As explained in Chapter 2 the permeability was not only dependent on the air filled porosity, but also on the connectivity and tortuosity, which on their turn depend on the soil texture and water content. Sand 2 has a higher water content in this experiment than sand 1, which decreases connectivity and increases tortuosity. To investigate this effect, water retention curves at different densities were obtained for both sands, from these the following relations are found for the Brooks and Corey parameters (Equations 6.1a-d). The derivation of these relations can be found in Appendix B.8.

$$\phi = 100 - \rho_d/2.65 * 100 \tag{6.1a}$$

$$\theta_{res} = 0.01 * (0.5 + clay + OC) \tag{6.1b}$$

$$P_e = e^{2*\rho_d + 0.02*clay} \tag{6.1c}$$

$$\lambda = 0.2 + 0.8 * clay - e^{0.14*clay*\rho_d} \tag{6.1d}$$

Where clay and OC are the clay and organic content fraction [%]. Ahoughalandari and Cabral (2017) conclude that it can be expected that an increase in dry density results in a higher air entry pressure, i.e. a decrease in the share of coarse pores corresponding to lower capillary pressure. The pedotransfer

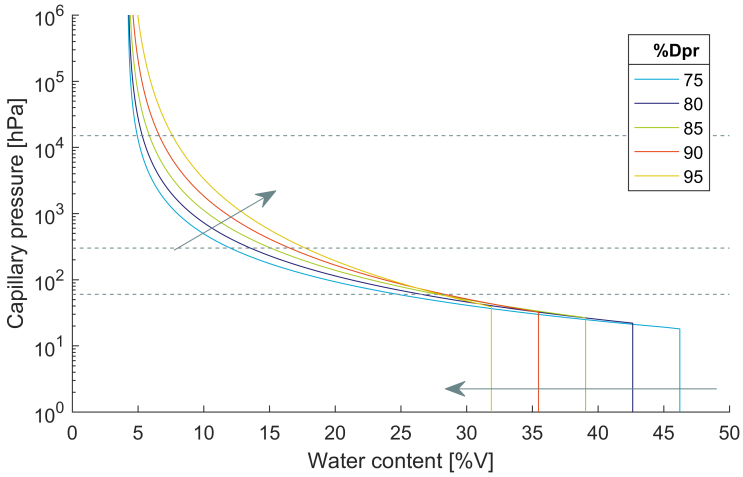

Figure 6.8: Water retention curves for sand 1 at multiple compaction levels: derived with the obtained pedotransfer functions. The arrows indicate the trend for increase in compaction level. The grey dotted lines show the pore sizes from top to bottom: fine pores, medium pores, fine coarse pores, wide coarse pores.

functions obtained with these sands support that. Five water retention curves for different levels of compaction based upon these pedotransfer functions are shown in Figure 6.8. These curves show that indeed the larger pores are affected mostly by compacting, as was expected.

Back-calculating the intrinsic permeability by Brooks and Corey formulation (see Subsection 3.1.1) gives the intrinsic permeabilities for each compaction level. These are shown in Figure 6.9. Both sands show exponential decay with increasing density. This exponential decay confirms the hypothesis that at first compaction has a lot of influence on the permeability. Upon further compaction this influence becomes smaller and smaller.

In contrast to Figure 6.6, now, the difference between the two sands can be seen. It shows clearly that sand 1 is more permeable than sand 2, even though it has a higher proctor density. This can be explained by the difference in particle size distribution. Firstly, sand 1 has a lower clay fraction than sand 2. Secondly, sand 1 has slightly coarser sand than sand 2. Thirdly, sand 1 has less (no) carbonate than sand 2.

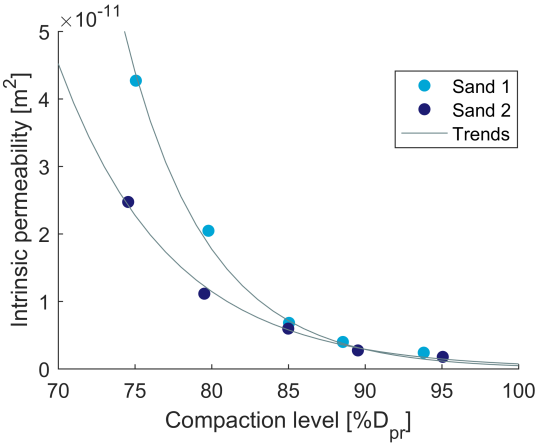

Figure 6.9: Relationship between compaction level and intrinsic permeability

6.5 Experiment 2: variable water content

The second experiment was performed for both sands on five columns with varying water contents at approximate capillary pressures of 120, 300, 1000, 3000 and 15000hPa. Table 6.3 presents the details of these 10 columns. Again, the average numbers of drops per construction layer are shown here. The effective compaction energy was calculated with Equation 5.1. The ground pressure of a bulldozer driving over a 10cm construction layer once, was back-calculated with Equation 5.2. The resulting compaction levels and water contents are shown in Table 6.3. The air content was back-calculated, assuming a particle density of $2.65 kg/cm^3$. Furthermore, the effective permeabilities are shown in the table, which were obtained by fitting equation 5.7. The experimental data for the second experiment can be found in Figures 6.11 and 6.12. The full data curves and corresponding fits are presented in Appendix B.7.

Table 6.3: Details on the compaction procedure and obtained physical properties for the water content experiment.

Sand 1

Column		6	7	3	8	9
Fall height	$[cm]$	40	40	50	10	10
Number of drops	$[-]$	20	24	25	34	10
Effective compaction energy	$[kJ]$	156	175	227	59	21
Ground pressure	$[kg/cm^2]$	1.35	1.45	1.84	0.49	0.18
Compaction level	$[\%D_{pr}]$	83.05	84.31	85.04	84.45	84.39
Water content	$[\%V]$	4.98	8.14	12.34	18.77	24.54
Air content	$[\%V]$	35.48	31.42	26.69	20.68	14.95
Effective permeability	$[m^2]$	$3 \cdot 10^{-12}$	$4 \cdot 10^{-12}$	$4 \cdot 10^{-12}$	$8 \cdot 10^{-12}$	$8 \cdot 10^{-12}$

Sand 2

Column		6	7	3	8	9
Fall height	$[cm]$	70	30	15	15	20
Number of drops	$[-]$	20	34	33	13	8
Effective compaction energy	$[kJ]$	262	178	87	39	36
Ground pressure	$[kg/cm^2]$	2.14	1.44	0.70	0.32	0.29
Compaction level	$[\%D_{pr}]$	84.96	85.02	84.99	84.99	84.97
Water content	$[\%V]$	12.46	16.66	20.31	25.55	30.99
Air content	$[\%V]$	31.12	26.88	23.25	18.00	12.58
Effective permeability	$[m^2]$	$7 \cdot 10^{-12}$	$6 \cdot 10^{-12}$	$6 \cdot 10^{-12}$	$7 \cdot 10^{-12}$	$2 \cdot 10^{-12}$

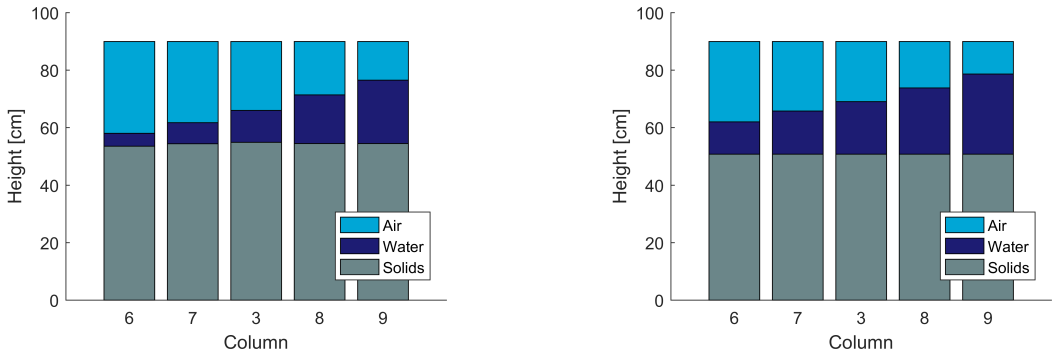

(a) Sand 1

(b) Sand 2

Figure 6.10: Visualisation of volumetric contents for the water content experiment

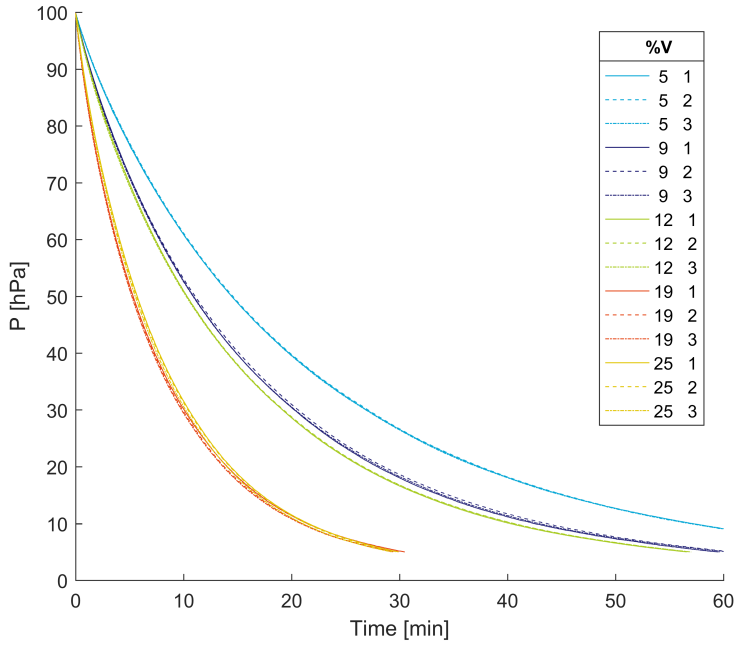

Figure 6.11: Change of pressure over time in relation to water content, sand 1. Each pressure loss test is performed in threefold (see 1, 2, 3 in legend).

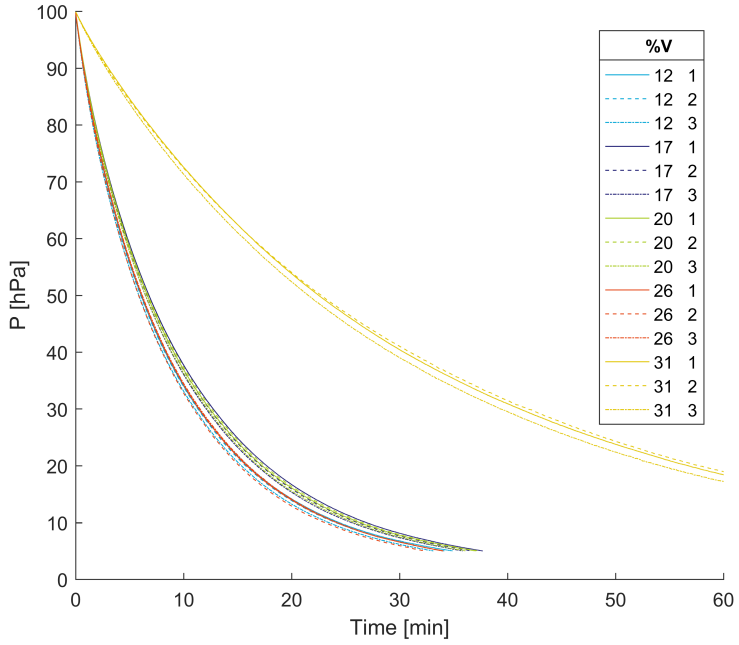

Figure 6.12: Change of pressure over time in relation to water content, sand 2. Each pressure loss test is performed in threefold (see 1, 2, 3 in legend).

Similarly as in experiment 1 the intended water contents and proctor densities are approached quite closely. Only column 6 of sand 1 shows deviation to the intended compaction level and column 9 of sand 1 to the intended water content. Again a bar plot is presented to visualise the differences between the columns, see Figure 6.10. For sand 2, with increasing water content, the compaction energy decreases. This is expected, since the tests are all performed at the dry side of the proctor curve. However, the opposite is seen for sand 1 for the first three columns. This can be explained by looking at the compaction level, which increases slightly for the first three columns. Thus it can be concluded for the investigated soils that the density that has to be reached has more influence on the needed compaction energy than the water content.

Figures 6.11 and 6.12 show contradicting trends. For sand 1, the duration of the test becomes longer at higher compaction levels, whereas for sand 2, the duration becomes shorter. The effective permeabilities are shown in Figure 6.13. For sand 2, the following trend is observed: a relatively steady effective permeability, followed by a sudden drop due to water impeding connectivity. Again in contrast to sand 2, sand 1 shows an increasing effective permeability with increasing water content. This is, however, highly unlikely to be true, since gas flow through water is in the order of 10^4 times slower (Cabral et al., 2004). It is most likely that columns 6, 7 and 3 (5, 8 and 12.5%V, respectively) are not correctly tested, since the three of them show an increase in effective permeability when both the water content and compaction level increase. Furthermore, columns 8 and 9 (18 and 25%V, respectively) are expected to be valid, as they lay in line to converge to the intrinsic permeability, similar to the trend of sand 2 (see next paragraph). The three columns were, however, constructed and tested in the same way as all other columns, while these show trends in accordance with literature. Lastly, the water retention curves obtained for different densities for sand 1 show behaviour that fits in the trend of sand 2 (see Appendix B.8). A logical explanation is thus missing and therefore sand 1 is discarded in experiment 2. It is recommended to redo the experiment on this sand.

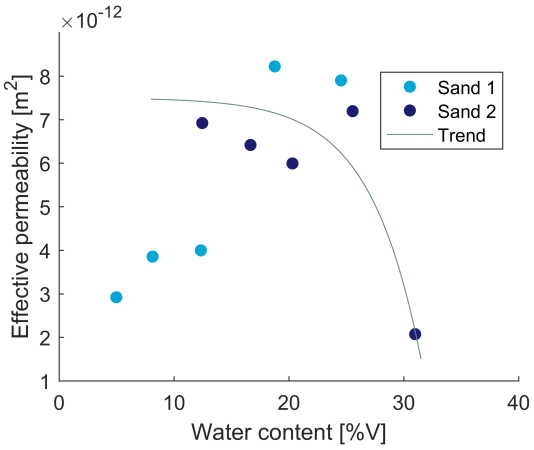

Figure 6.13: Relationship between effective permeability and water content

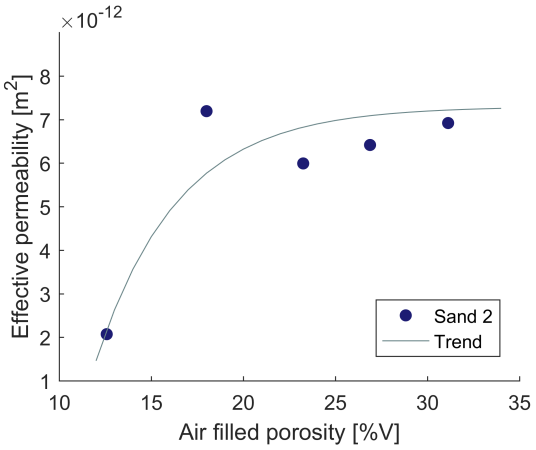

Figure 6.14: Relationship between effective permeability and water content

In Figure 6.14 the effective permeabilities for sand 2 are plotted against the air filled porosity. Similar to the first experiment, the effective permeability shows an increase with increasing air filled porosity. However, the trend converges to the intrinsic permeability instead of showing exponential growth. To clarify this difference in behaviour, both the experiments are plotted together for sand 2 in Figure 6.15. Clearly both show increasing effective permeability with increasing air filled porosity. However, compaction level has a larger influence on the intrinsic and thus on the effective permeability. Texture of the soil affected permeability on the same scale as compaction. Therefore, it can be concluded that the effective permeability is predominantly influenced by the compaction level and the texture. Water

content only has large influence near saturation.

Furthermore, this figure shows that at similar air filled porosities, the effective permeability can differ depending on the the compaction level and water content. For instance, the compaction experiment shows that at an air filled porosity of $20\%V$, the $95\%D_{pr}$ sample has an effective permeability of $2 \cdot 10^{-12} m^2$ at a water content of $19.35\%V$. At the same air filled porosity, the water content experiment shows that the $85\%D_{pr}$ sample with a water content of $\pm 27\%V$, has a permeability of approximately $6 \cdot 10^{-12} m^2$. This differs by a factor 3. This is in contradiction to Ahoughalandari and Cabral (2017), who state that the effective permeability is not much affected by the dry density if the air filled porosity remains constant. This difference can be explained by connectivity and tortuosity. At the high compaction levels, there are less coarse pores, which can therefore be easily disconnected. If the connectivity becomes lower often the tortuosity of the path length increases: the air is not likely to find a direct route. For lower compaction level at higher water level, the water mainly occupies the small pores. There are thus more coarse pores, which are better connected.

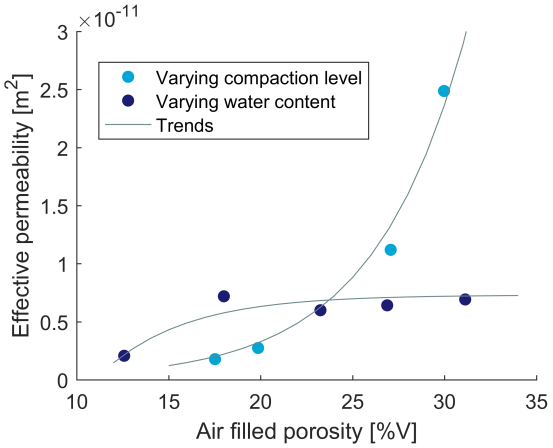

Figure 6.15: Relationship between effective permeability and air filled porosity for sand 2: Experiment 1 varies the compaction level, experiment 2 varies the water content.

7 Conclusions on experiments

Two experiments were performed to investigate the effects of the compaction level and hydraulic conditions on the effective permeability of a soil. These experiments were both conducted on two types of sand, so the effect of the physical properties could be researched. For each experiment ten columns were constructed (five per sand). These columns were tested with a falling tank pressure test. An analytical formulation was derived to fit the experimental data, based upon Darcy's law and the ideal gas law.

For the first experiment the columns were constructed at different levels of compaction of approximately 75, 80, 85, 90 and 95%D_{pr}. The results clearly showed the same trend for both sands: the intrinsic permeability decays exponentially with increasing density. This leads to an exponential decay of the effective permeability with increasing compaction level and an exponential increase of the effective permeability with an increase in air filled porosity. The exponential trends confirm the hypothesis that the initial compaction will have a large influence on the effective permeability, while upon further compaction this influence becomes smaller and smaller.

Sand 2 has higher effective permeabilities than sand 1 at similar air filled porosities, while it has lower intrinsic permeabilities at similar degrees of compaction. This is attributed to the dependency of the effective permeability on the soil texture and water content. Sand 2 has a higher clay content and finer sand fractions than sand 1, leading to a higher proctor density, smaller pores, which decrease the intrinsic permeability. Furthermore, from the derived pedotransfer functions it can be concluded that the capacity to retain water is mainly dictated by the clay fraction and the bulk density of the sands. Therefore, at the same capillary pressure the volumetric water content differs for the two sands. Sand 1 has a higher water content than sand 2, which decreases the connectivity and increases the tortuosity. So even though sand 2 has a lower intrinsic permeability, it shows a higher effective permeability than sand 1 at the same air filled porosity.

For the second experiments the columns were constructed at different water contents corresponding to capillary pressures of 120, 300, 1000, 3000 and 15000hPa. For this experiment the results for sand 1 were disregarded, because it showed inexplicable results for three of the five columns probably due to construction or measurements errors. The results for sand 2, however, show a trend of relatively steady effective permeability upon wetting, followed by a sudden drop. This is attributed to water impeding the connectivity after a certain threshold and confirms the hypothesis. The effective permeability converges to the intrinsic permeability with increasing air filled porosity.

Both experiments show an increase in effective permeability with increasing air filled porosity. However, compaction shows an exponential trend changing the intrinsic permeability, whereas increasing water content shows convergence to the intrinsic permeability at that compaction level. It can be concluded that compaction level and soil texture predominantly influence the effective permeability, whereas the influence of water content only becomes significantly at high water contents. Lastly, it is shown that

at constant air filled porosity the effective permeability of the same sand can vary due to the combined effects of compaction level and water content on the connectivity and tortuosity of the sand. These conclusions combined mean that the choice of suitable material and adequate construction practice has more effect on the effective permeability than seasonal changes in saturation levels in moderate climates.

Part III

Numerical model

8 Introduction to numerical model

In the introduction and background of this thesis, the importance of homogeneous LFG flux from the GDL into the MOL is explained. This part presents the numerical model built to answer the last three research questions:

- How can gas flow within a methane oxidation system be modelled?
- What is the minimum effective permeability ratio between the methane oxidation layer and gas distribution layer for a homogeneous methane flux?
- What should the centre-to-centre distance be of the gas inlet points to accomplish a homogeneous methane flux distribution?

The second and third question are of a spatial nature, therefore the spatial design of a methane oxidation system must be addressed, as will be done below. Next, the conceptual model is presented. Lastly, the hypothesis will be presented.

8.1 Spatial design of a methane oxidation system

The required dimensions and thickness of a methane oxidation system are dependent on the available materials and environmental conditions. These define the permeability of the sand and gravel, the expected LFG load to be oxidised, and the intended after-use of the landfill (Huber-Humer et al., 2008). The total methane load to be oxidised [gCH_4/day] is based upon the methane production of the landfill. The intended methane load per squared meter [gCH_4/m^2day] is chosen based upon the methane oxidation capacity of the MOL. When both are defined, the contractor can decide on the dimensions of the methane oxidation system. For example, a total methane load of 200000 gCH_4/day and a methane load per squared meter of $100gCH_4/m^2day$ could lead to a methane oxidation system of $40mx50m$.

At this point it is not decided yet how many inlet points are required to obtain a spatial homogeneous LFG flux from the GDL into the MOL. Continuing the example, two options for the spatial design are illustrated in Figure 8.1. One option is to have a centre-to-centre distance of $10m$. The total load on the field is equally divided over the inlet points, thus creating an inlet load of $200000/20 = 10000gCH_4/day$. An other option is to choose for a centre-to-centre distance of $5m$ between the inlet points. There are now four times more inlet points needed, decreasing the inlet load to $200000/80 = 2500gCH_4/day$. Two parameters can now be varied: 1) The intended methane load per square meter, which changes both the intended load per square meter and the inlet load. 2) The amount of inlet points, which effects the centre-to-centre distance between the inlet points. This changes the inlet load, while the intended load per square meter remains constant. Therefore these two parameters are varied in the simulations.

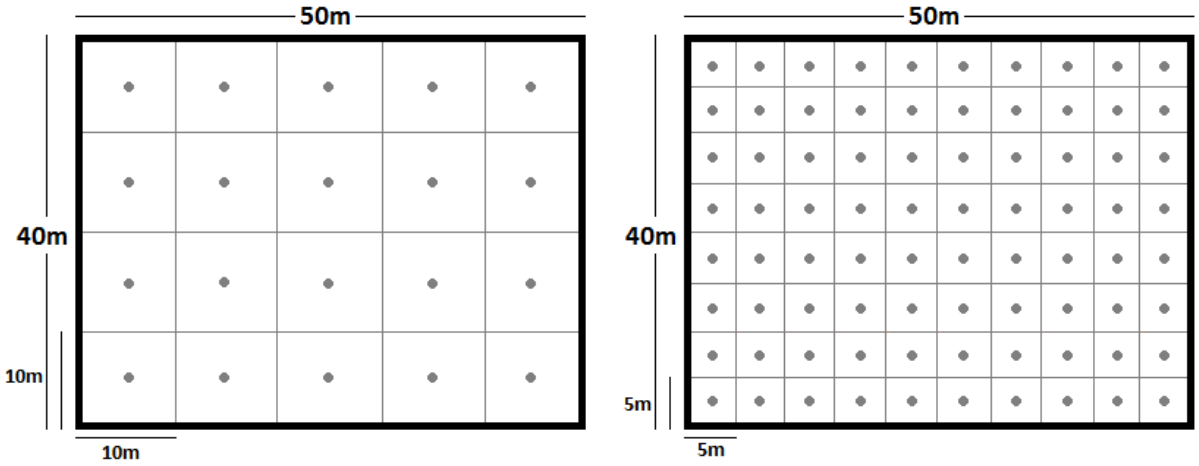

Figure 8.1: The spatial design of the inlet points: a top view on a methane oxidation system. Two cases: Left, the centre-to-centre distance between the inlet points is $10m$, and the inlet load is $10000gCH_4/day$. Right, the centre-to-centre distance between the inlet points is $5m$, and the inlet load is $2500gCH_4/day$. The total methane load for the whole field remains constant.

8.2 Conceptual model

To answer the three research questions mentioned above, only one inlet point and its according part of the methane oxidation system need to be modelled, as illustrated in Figure 8.2. To speed up the model, it is modelled as a 2D radial problem, thus a circular tube instead of a cube. The model is made in COMSOL Multiphysics as a 2D radial model. COMSOL was chosen as van Turnhout (2017) modelled a similar problem in COMSOL.

The LFG flux enters the gas distribution layer via the inlet point, as shown in Figure 8.2. If the MOL has a lower permeability than the GDL, this works as a resistance: some of the LFG is passing through, while the rest flows away in lateral direction. Therefore, the amount of LFG decreases with an increasing

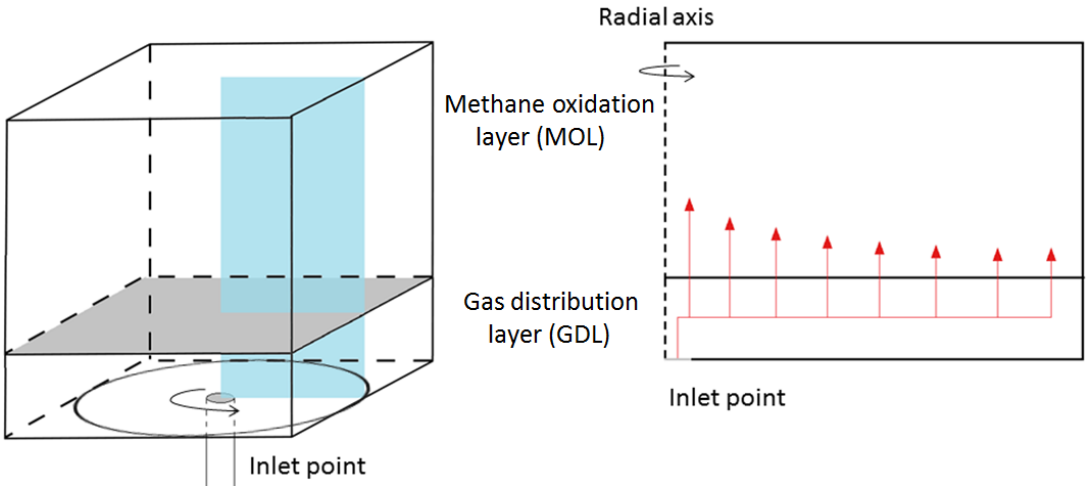

Figure 8.2: The conceptual model of a methane oxidation system: On the left side, one inlet point and its according part of the methane oxidation layer. On the right side, the gas flux through the GDL is shown of the cross-section indicated in blue in the left figure.

radius. The flux into the MOL is expected to decrease as well, with increasing radius. The methane flux distribution will thus not be homogeneous. For the purpose of this thesis the flux is adequately homogeneous when:

$$\frac{F_{R=R_{max}}}{F_{R=0}} \geq 0.95 \tag{8.1}$$

Where F is the methane flux from the GDL into the MOL in $[mol/m^2day]$ at the radius R.

8.3 Hypothesis

Based upon Chapter 3 it is expected that the methane oxidation system can be modelled with a advection and diffusion model coupled to a water model and a methane oxidation model. Advection and diffusion must be taken into account in order to simulate gas flow through the methane oxidation system, since there is a pressure and concentration difference between the landfill and the atmosphere.

In order for the GDL to work, the GDL must have a higher permeability than the MOL. The higher the ratio between the two permeabilities, the better the GDL can spread the gas. However, when an adequate spatial homogeneity is reached for a given centre-to-centre distance of the gas inlet points, it is expected that increasing the permeability ratio further does not have much effect on the spatial homogeneity. There must thus be an minimum permeability ratio for the methane oxidation system to perform acceptably.

Furthermore, the hypothesis is that the centre-to-centre distance has a maximum value for which an acceptable homogeneous methane flux distribution from the GDL into the MOL is still preserved. This value is expected to be dependent on the methane load and on the permeability ratio between the GDL and MOL. With a higher load and/or a higher permeability ratio, the maximum centre-to-centre distance provided homogeneous methane distribution is expected to increase. The minimum permeability ratio will thus also be dependent on the radius.

9 Model implementation

This chapter presents the implementation of the numerical model. The model is made in COMSOL Multiphysics as a 2D radial model, with the Coefficient Form PDE module. This approach was adopted from van Turnhout (2017), who built a landfill model with the same module. This chapter will first present the governing equations, followed by the material properties. Then the geometry and mesh are discussed, after which the initial and boundary conditions will be presented.

9.1 Governing equations

The governing equations are based upon conservation of mass. COMSOL requires the governing equations to be in a density or concentration form. Since gas is compressible and, in this problem, its composition is variable, the concentration form is chosen. This gives the following standard form, where the change in concentration is driven by diffusion (J) and advection or convection (q).

$$\frac{dc_T}{dt} = -\nabla \cdot (J) - \nabla \cdot (qc_T) - R \tag{9.1}$$

Where c_T is the concentration of a certain component ($_a$) per total volume $[mol/m^3]$. ∇ is a differential operator and is defined for a radial problem as $[d/dr, d/dx]$ in $[1/m]$. R is the sink/source term $[mol/m^3 s]$. It is important to note that this concentration (c) is the number of moles of a certain component ($_a$) per total volume ($_T$). Thus for a component a, the concentration per total volume can also be described by:

$$\theta_a c_a = \frac{V_a}{V_T}\frac{n_a}{V_a} = \frac{n_a}{V_T} = c_{Ta} \tag{9.2}$$

with θ_a the volumetric fraction of component a [-] and c_a the number of moles of component a per volume of component a $[mol/m^3]$.

There are two phases in the system, which are free to move: the water phase and the gas phase. For this problem, the water phase comprises of one component, whereas the gas phase comprises of multiple. As described in Chapter 3, the two phases are coupled via the capillary pressure and volumetric fractions. The water retention curves for both sands were best fitted by the equation according to Brooks and Corey, see Chapter 5. Accordingly, this equation will be used in this model to describe the water retention. These equations are formulated as:

$$P_c = P_g - P_w \tag{9.3}$$

$$\phi = \theta_w + \theta_g \tag{9.4}$$

$$S_{eff} = \begin{cases} \left(\frac{P_e}{P_c}\right)^{\lambda}, & P_c > P_e \\ 1\ , & P_c \leq P_e \end{cases} \qquad \text{with} \qquad S_{eff} = \frac{\theta_w - \theta_r}{\phi - \theta_r} \tag{9.5}$$

Where P_c, P_g and P_w are the capillary, total gas and water pressures $[Pa]$, respectively. ϕ is the porosity $[-]$ and θ_w and θ_g is the volumetric water and gas fractions $[-]$. S_{eff} is the effective saturation $[-]$. P_e, λ, and θ_r are the water retention parameters and are, respectively, air entry pressure $[Pa]$, pore size distribution index $[-]$, and residual water fraction $[-]$.

9.1.1 Water phase

Water movement is assumed to only be driven by convection, thus the diffusion term becomes zero. As explained in Chapter 3, the convection term is expressed by Darcy's law. Rewriting everything into pressures gives the following equations. The full derivation can be found in Appendix C.1.

$$-c_w C_{pc} \frac{dP_w}{dt} + \nabla \cdot (q_w \theta_w c_w) = -c_w C_{pc} \frac{dP_g}{dt} - R_w \tag{9.6}$$

$$C_{pc} = -(\phi - \theta_r)\lambda P_e^{\lambda} P_c^{-\lambda-1} \tag{9.7}$$

$$q_w = -\frac{\kappa k_{rw}}{\mu_w}(\nabla P_w + \rho_w g \nabla z) \tag{9.8}$$

$$k_{rw} = S_{eff}^{\frac{2+3\lambda}{\lambda}} \tag{9.9}$$

Where c_w is the concentration of water $[mol/m^3]$. q_w is the Darcy flux of water $[m/s]$, and R_w the water source $[mol/m^3 s]$ and will be 0 for this thesis. κ is the soil's permeability $[m^2]$. μ_w and ρ_w are the dynamic viscosity $[Pa \cdot s]$ and density $[kg/m^3]$ of water. g is the gravitational acceleration $[m/s^2]$. k_{rw} is the relative permeability factor for water $[-]$ according to Brooks and Corey (Heimovaara, 2016).

9.1.2 Gas phase

Gas movement is driven by both diffusion and advection. The gas movement is split into the movements per component, which are coupled via the total gas pressure, which is the sum of all partial pressures. As described in Chapter 3, the diffusion term will be described by Fick's law and the advection term by Darcy's law for gas. The concentration of the gas can be expressed in terms of pressure via the ideal gas law. Rewriting everything into pressures gives the following equations. The full derivation can be found in Appendix C.2.

$$\frac{\theta_g}{RT}\frac{dP_i}{dt} + \nabla \cdot (J_i) + \nabla \cdot (q_g \theta_g \frac{P_i}{RT}) = C_{pc}(\frac{dP_g}{dt} - \frac{dP_w}{dt})\frac{P_i}{RT} - R_i \tag{9.10}$$

$$J_i = -\frac{\theta_g^2 .5 D_{im}}{\phi RT} \nabla P_i \tag{9.11}$$

$$q_g = -\frac{\kappa k_{rg}}{\mu_g} \nabla P_g \tag{9.12}$$

$$k_{rg} = (1 - S_{eff})^2 \left(1 - S_{eff}^{\frac{2+\lambda}{\lambda}}\right) \tag{9.13}$$

$$\mu_g = \frac{1}{\sum \frac{P_i/P_g}{\mu_i}} \tag{9.14}$$

$$P_g = \sum P_i \tag{9.15}$$

$$\frac{dP_g}{dt} = \sum \frac{dP_i}{dt} \tag{9.16}$$

Where R is the universal gas constant $[J/Kmol]$, T the temperature [K]. P_i is the partial pressure of component i $[Pa]$. Ji is the diffusive flux for component i $[mol/m^2s]$ and q_g the Darcy flux for the bulk gas $[m/s]$. R_i is the source term for component i $[mol/m^3s]$, which is the methane oxidation term as derived in Section 3.5. The diffusion coefficient of component i D_{im} is derived according to equation 3.14. μ_g and μ_i are the dynamic viscosities of the gas mixture and of component i $[Pas]$, respectively. k_{rg} is the relative permeability factor for gas $[-]$ according to Brooks and Corey (Heimovaara, 2016).

9.2 Material properties

The material properties are obtained from the laboratory experiments, from literature or from the calibration, as will be explained in the paragraph below. It is assumed that the methane oxidation layer and the gas distribution layer are isotropic and homogeneous. The water is assumed to be incompressible and the gas is assumed ideal, following the ideal gas law, where temperature is assumed to be constant. The atmospheric pressure is taken at sea level. The material properties for the simulations are shown below in Table 9.1.

The water retention parameters (P_e, λ, θ_{res} and ϕ) for the sand are obtained from one of the lab tests and the intrinsic permeability (κ) for the sand is fitted by hand to the same test. For the gravel the water retention parameters are estimated assuming immediate drainage and the intrinsic permeability is varied within the range of permeabilities for gravel. The atmospheric temperature (T_{atm}) is chosen to be room temperature. The binary diffusion coefficients (D_{ij}) are recalculated according to Scheutz et al. (2009) for T_{atm} and $P = 1atm$. All viscosities (μ_i) and water density (ρ_w) are obtained from Engineering Toolbox URL (2018) for T_{atm}. The hydraulic concentration (c_w)is calculated based upon the molar mass of water and its density. The water table (z_{wt}) is calculated based upon the soil parameters for a water content of $12.34\%V$. Lastly, the oxidation parameters: the maximum oxidation rate (V_max) is based upon Table 2 within (Scheutz et al., 2009), and recalculated for soil 1, with a density of $85\%D_{pr}$. The Michaelis-Menten constants (K_i) are as adopted in Perera et al. (2002). Henry's constants (H_i^{cp}) are obtained from Sander (2014).

Table 9.1: Overview of the parameters for the soil, gas phase, methane oxidation process and hydraulic phase

Soil parameters

$P_{e,s}$	18.25	hPa
λ_s	0.60	$-$
$\theta_{res,s}$	0.042	$-$
ϕ_s	0.46	$-$
κ_s	$1.1 \cdot 10^{-11}$	m^2
$P_{e,gr}$	0.1	hPa
λ_{gr}	1	$-$
$\theta_{res,gr}$	0.01	$-$
ϕ_{gr}	0.375	$-$
κ_{gr}	$1.1 \cdot 10^{-8}$	m^2

Oxidation parameters

V_{max}	$6.57 \cdot 10^{-4}$	mol/m^3s
K_{CH_4}	0.05	mol/m^3
K_{O_2}	0.44	mol/m^3
$H^{cp}_{CH_4}$	$1.4 \cdot 10^{-5}$	mol/m^3Pa
$H^{cp}_{O_2}$	$1.3 \cdot 10^{-5}$	mol/m^3Pa

Gas parameters

$D_{CH_4-CO_2}$	$1.743 \cdot 10^{-5}$	m^2/s
$D_{CH_4-O_2}$	$2.197 \cdot 10^{-5}$	m^2/s
$D_{CH_4-N_2}$	$2.078 \cdot 10^{-5}$	m^2/s
$D_{CO_2-O_2}$	$1.587 \cdot 10^{-5}$	m^2/s
$D_{CO_2-N_2}$	$1.599 \cdot 10^{-5}$	m^2/s
$D_{O_2-N_2}$	$2.026 \cdot 10^{-5}$	m^2/s
μ_{CH_4}	$1.10 \cdot 10^{-5}$	$Pa \cdot s$
μ_{CO_2}	$1.47 \cdot 10^{-5}$	$Pa \cdot s$
μ_{O_2}	$2.04 \cdot 10^{-5}$	$Pa \cdot s$
μ_{N_2}	$1.76 \cdot 10^{-5}$	$Pa \cdot s$
T_{atm}	293.15	K

Hydraulic parameters

μ_w	$1.00 \cdot 10^{-3}$	$Pa \cdot s$
ρ	998	kg/m^3
c_w	55.38	mol/L
z_{wt}	-3.17	m

9.3 Geometry and mesh

Ranges for the GDL and MOL thickness are found in literature as 10-50cm and 30-120cm, respectively (Sadasivam and Reddy, 2014; Ahoughalandari and Cabral, 2017; Huber-Humer et al., 2008). Therefore, the thickness of the GDL (gravel layer) is chosen to be $30cm$, overlain by the MOL (sand layer) with a thickness of $80cm$. The geometry is shown in Figure 9.1. For the simulations, sand 1 was chosen as MOL soil. Therefore an inlet radius was chosen of $10cm$ inner diameter, similar to the inlets constructed at the Hamburg site (source of sand 1). The inlet seems to be on the left, but is actually located in the middle of a circle, since the model is 2D radial. The radius of this circle is $6m$ in the figure, but is actually varied between 3, 6, 9, 12 and $15m$. These radii were chosen based on the methane oxidation window constructed at the Hamburg landfill, which has a radius of $8.5m$.

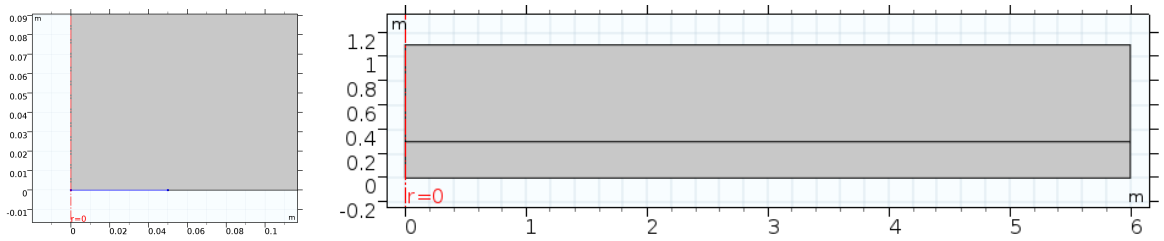

Figure 9.1: The geometry of the model: the full geometry (right) and zoomed in on the inlet (left).

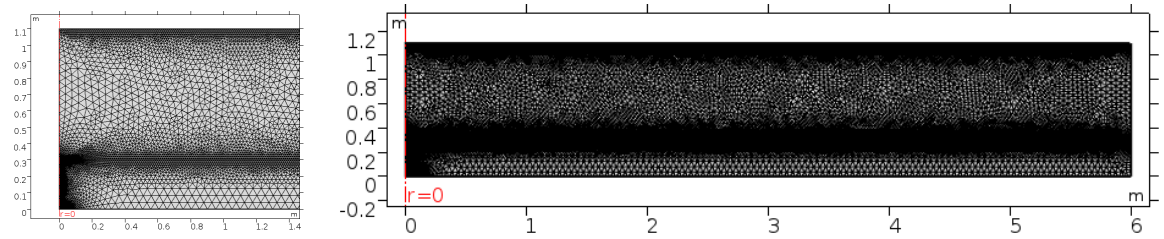

Figure 9.2: Mesh: the full geometry mesh (right) and zoomed in at r=0 (left)

The mesh was generated with triangular elements, as illustrated in Figure 9.2. Near the inlet, the MOL-GDL interface and the top boundary the mesh was further refined, because the pressure and concentration gradients are larger near these places. The total mesh consisted of 38278 elements.

Numerical dispersion

The influence of numerical dispersion was checked by running the 'worst case' variation (thus under the largest load $200gCH_4/m^2day$, largest radius $15m$ and smallest gravel permeability $1.1 \cdot 10^{-10}m^2$) a second time with a very fine mesh and small maximum time step. This resulted in a deviation of 0.5% above the inlet and 0.1% above the maximum radius. This can be seen in Figure 9.3. It results in an underestimation of 0.5% in flux ratio for the worst case scenario. This underestimation can be explained due to the numerical dispersion, which causes the flow to go faster for larger element. The spread is thus slightly better for the coarser mesh, causing the flux above the inlet to be slightly underestimated. The mesh is accepted as fine enough.

9.4 Boundary and initial conditions

The top of the methane oxidation system is located in open air, therefore a Dirichlet boundary condition is chosen at the top, with atmospheric conditions. This means the standard atmospheric pressure at sea level and a composition similar to the atmospheric composition. These values are shown in Table 9.2.

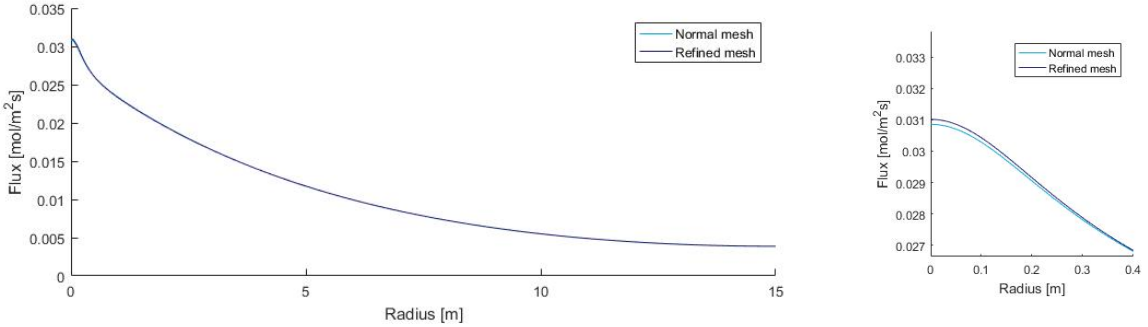

Figure 9.3: Influence of numerical dispersion. Left, the flux over the whole radius for the 'worst case' scenario. Right, the same scenario, but zoomed in on 0 to $0.4m$

The Dirichlet boundary dictates that these values must stay exactly like this at all times. The fluxes are free to change in order to accomplish this.

The left and right boundaries are zero flux boundaries, which means no flow is allowed through these boundaries. This assumption can be made due to repetition of the geometry in the larger field. Due to symmetry, equal conditions hold at both sides of these boundaries, so no gradients occur over the boundaries. No parameters need to be defined in order to apply this boundary condition in COMSOL.

The bottom of the methane oxidation system has two different boundary conditions. At the inlet a Neumann boundary is applied. This means that the gradient over the boundary is defined, while the pressures and concentration are free to change in order to accomplish this gradient. In COMSOL there is the option to directly define the component flux through the boundary. Therefore, the fluxes of all the components are defined for this boundary. Generally in literature, the load for a methane oxidation system is defined in grams of methane per square meters of methane oxidation system per time unit. Therefore, the load is defined here in a similar way. Subsequently, the flux of methane is back-calculated by:

$$F_{CH_4} = \frac{Load}{M_{CH_4}} \frac{R^2}{A_{inlet}} \tag{9.17}$$

Where F_{CH_4} is the inlet methane flux $[mol/m^2s]$. M_{CH_4} is the molecular weight of methane $[kg/mol]$, which is used to back-calculate the grams of methane to moles of methane. R^2 is the squared area of the part of the methane oxidation system that belongs to this inlet $[m^2]$. Since the model is modelled as a 2D radius however, this will results in a slight overestimation of the flux ratio, which is excepted for the purpose of this thesis. Lastly, A_{inlet} is the area of the inlet itself $[m^2]$. The other inlet fluxes can now be back-calculated by the partial fractions. This is shown below for the carbon dioxide flux.

$$F_{CO_2} = F_{CH_4} \frac{x_{CO_2}}{x_{CH_4}} \tag{9.18}$$

The values of the bottom boundary conditions can be found in Table 9.2. Scheutz et al. (2009) state that gas fluxes for older landills are approximately $85 gCH_4/m^2day$, while new landfills can reach a gas production of $1300 gCH_4/m^2day$. However, other research shows loads can also be lower (Gebert and Groengroeft, 2006). Since methane oxidation systems are designed for older landfills, four load cases per square meter are chosen as 20, 50, 100, and $200 gCH_4/m^2day$.

These conditions all hold at the inlet boundary. However, the rest of the bottom of the methane oxidation system is assumed to be a zero flux boundary as well.

Table 9.2: Boundary conditions for the gas pressure and composition (top) and methane load (bottom)

Top boundary		
P_{atm}	101325	Pa
$x_{CH_4,atm}$	0.00	–
$x_{CO_2,atm}$	0.02	–
$x_{O_2,atm}$	0.20	–
$x_{N_2,atm}$	0.78	–

Bottom boundary		
$Load$	200	gCH_4/m^2day
$x_{CH_4,inlet}$	0.60	–
$x_{CO_2,inlet}$	0.40	–
$x_{O_2,inlet}$	0.00	–
$x_{N_2,inlet}$	0.00	–

The initial conditions are chosen to be at atmospheric conditions, and thus are equal to the top boundary conditions. They can be found in the Table 9.3. The initial conditions for the water phase are hydro-static and are dictated by the water table, as was defined in Table 9.1.

Table 9.3: Initial conditions for gas pressure and composition

P_{atm}	101325	Pa
$x_{CH_4,atm}$	0.00	–
$x_{CO_2,atm}$	0.02	–
$x_{O_2,atm}$	0.20	–
$x_{N_2,atm}$	0.78	–

10 Verification

This chapter presents the verification of the numerical model. It start of with the verification of the advection part of the model and continues with the verification for the diffusive and methane oxidation parts.

10.1 Advection

The five column tests of experiment 1 for sand 1 were simulated as validation of the advective part of the modelled flux. Table 10.1 shows the soil parameters that change with compaction. Their values are derived according to the pedotransfer functions obtained from the laboratory, see equation 6.1. The water levels are chosen such that the water contents in the middle of the sand sample (at 55cm height; 10 cm gravel + 0.45 cm sand)resemble the water contents from the laboratory experiments. The other model parameters are defined as for the base case.

Table 10.1: Soil parameters for laboratory experiment simulations

Parameters	**Column 1**	**Column 2**	**Column 3**	**Column 4**	**Column 5**	Unit
Compaction level	75.06	79.79	85.04	88.55	93.82	$\%D_{pr}$
Water content	12.54	12.33	12.34	12.37	12.41	$\%V$
$P_{e,s}$	18.25	21.85	26.67	30.47	37.23	hPa
λ_s	0.60	0.54	0.48	0.44	0.37	–
$\theta_{res,s}$	0.042	0.042	0.042	0.042	0.042	–
ϕ_s	0.46	0.43	0.39	0.37	0.33	–
z_{wt}	-1.06	-1.62	-2.41	-3.14	-4.73	m

To simulate the column tests, the geometry of the model was adjusted to fit the test set-up. However, the model is 2D radial and cannot model a separate tank. Therefore, the radius, height and porosity of the gravel were set to $1.57m$, $0.1m$ and 1, respectively, such that the gravel had the same air filled volume as the tank. Furthermore, no inlet point is required, which was thus excluded from the geometry. The radius and height for the sand were set to $75.5mm$ and $90cm$, similar to the inner radius of the the column. The new geometry can be found in Figure 10.1. Lastly, the initial and boundary conditions needed to be changed. The initial conditions for gas pressure and composition in the sand remained atmospheric. In the tank (the gravel layer) an over-pressure of $100hPa$ was required.

The intrinsic permeabilities were obtained by fitting the model to the experimental data manually and can be found in Table 10.2. The fits can be found in Figure 10.2. The figure clearly shows that the change in compaction for the model leads to similar behaviour as change in compaction in the lab experiments. Therefore, the advection part of the model is verified to show the expected behaviour at different compaction levels.

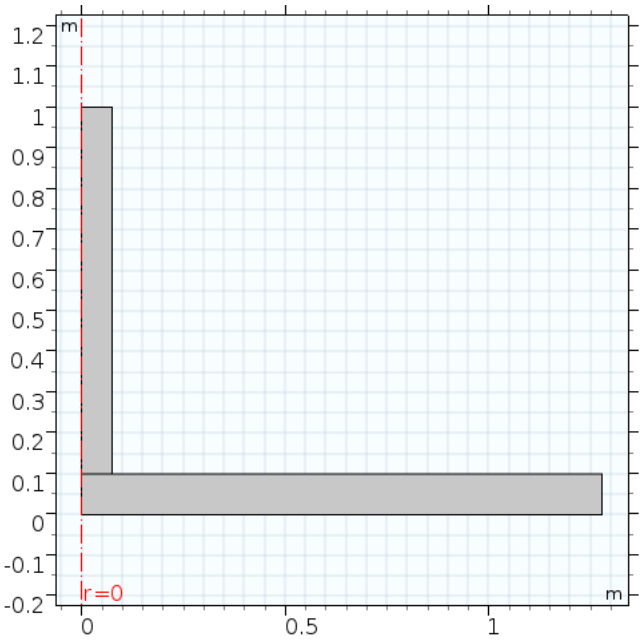

Figure 10.1: Geometry of the model for the column experiment.

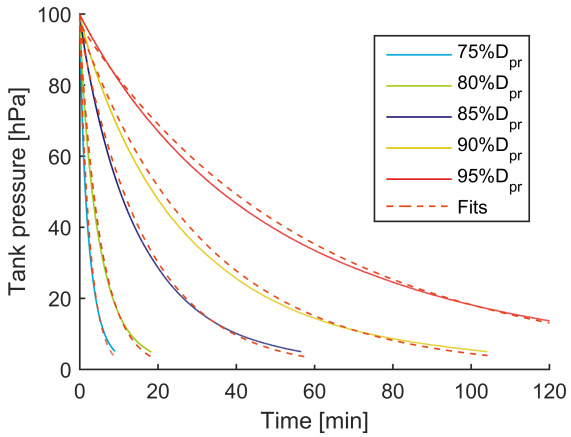

Figure 10.2: Numerical fits to the experimental data of the compaction experiment for sand 1.

10.1.1 Comparison to analytical fit

Figure 10.2 presents the intrinsic permeability fitted with the numerical and analytical models. The values for the intrinsic permeabilities are consistently lower for the numerical fit, deviating by a factor 2 to 4 from the values obtained by the analytical fit. This deviation can be explained by the fact that the numerical model takes a hydro static water content into account instead of a homogeneous water content throughout the sample. In addition, in the model the soil sample is discretised, which causes numerical dispersion. Due to the numerical dispersion the flow in the model flows faster than it actually does. Therefore the intrinsic permeability is underestimated by the model. However, in Chapter 9 it is proven that the numerical dispersion is small. All with all, on a scale where the permeability of sands ranges in orders of 10^5 (Warrick, 2002), the deviations between the numerically and analytically obtained permeabilities are low. The numerically obtained values are expected to be more reliable, since the model

Table 10.2: Intrinsic permeabilities obtained by the numerical and analytical fits.

Compaction level	Numerical fit	Analytical fit	Unit
$75\%D_{pr}$	$1.1 \cdot 10^{-11}$	$4.3 \cdot 10^{-11}$	m^2
$80\%D_{pr}$	$6.2 \cdot 10^{-12}$	$2.1 \cdot 10^{-11}$	m^2
$85\%D_{pr}$	$2.4 \cdot 10^{-12}$	$6.8 \cdot 10^{-12}$	m^2
$90\%D_{pr}$	$1.5 \cdot 10^{-12}$	$3.4 \cdot 10^{-12}$	m^2
$95\%D_{pr}$	$1.1 \cdot 10^{-12}$	$2.4 \cdot 10^{-12}$	m^2

takes more influential parameters into account.

Plotting the numerically and analytically obtained intrinsic permeabilities against each other shows a strong correlation between them, as illustrated in Figure 10.3. This means that both methods describe the system behaviour in the same way. Thus the numerical solution considered all influential parameters correctly. This also shows that, even though the numerical solution might be more reliable, the trends found with the analytical solution still hold.

Furthermore, Figure 10.2 shows that for the numerical fit the same problem occurs as with the analytical fit: the fit cannot get curved enough to fit the experimental data perfectly. Therefore, discretisation can be excluded as reason for this behaviour, see the elaboration on possible explanations for the discrepancy between the fits and the experimental data in Section 6.2.

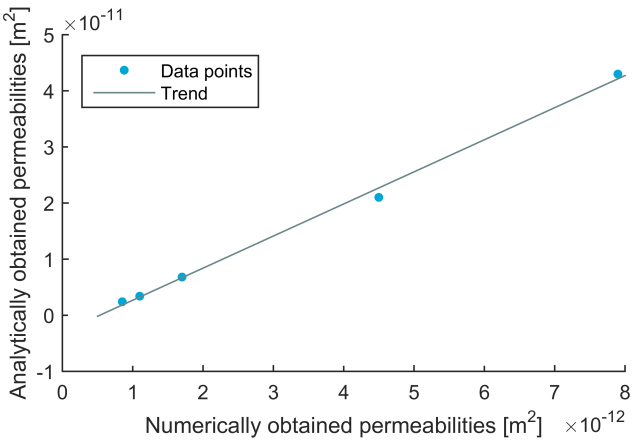

Figure 10.3: Correlation between the numerically and analytically fitted intrinsic permeabilities.

10.2 Diffusion and methane oxidation

Gebert et al. (2011) performed a research on the influence of compaction on the soil profiles created due to diffusion and methane oxidation. Three cases have been simulated to validate the diffusion and methane oxidation part of the numerical model, by checking if the model shows similar behaviour as the experiments from Gebert et al. (2011). The test set-up used by Gebert et al. (2011) is shown in Figure 10.4. The model geometry is adjusted to fit the test set-up and can be found in Figure 10.5. The inlet now covers the whole bottom of the model. The boundary and initial conditions are similar to the base case, except for the methane load, which was set to $19.11 gCH_4/m^2h$. The three cases from the experiments are shown below in Figure 10.6. The results for the three compaction levels are shown in Figure 10.7.

The model shows a similar trend with changing compaction level as the laboratory experiments. However, the model needed a 13 times higher load to simulate this behaviour. This can be explained by the fact

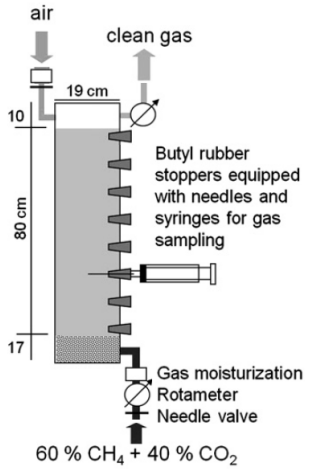

Figure 10.4: Schematic column set-up for diffusion experiment, not to scale. Adapted from Gebert et al. (2011), Figure 2.

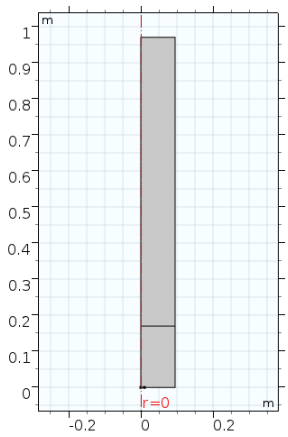

Figure 10.5: Model geometry for simulating diffusion experiments.

that a different soil is modelled under different air filled porosities. Yet, the change in soil profile between the different compaction levels are quite similar. Therefore, it can be concluded that the diffusive part of the model and the methane oxidation are verified to behave via the expected pattern.

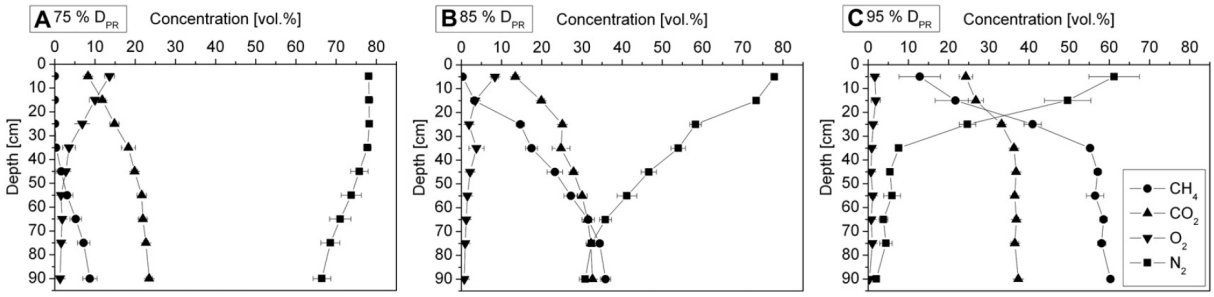

Figure 10.6: Experimental gas profiles for low (A), medium (B) and high (C) degrees of compaction (D_{pr}) at a methane load of $1.47 gCH_4/m^2h$. Altered from Gebert et al. (2011), Figure 7.

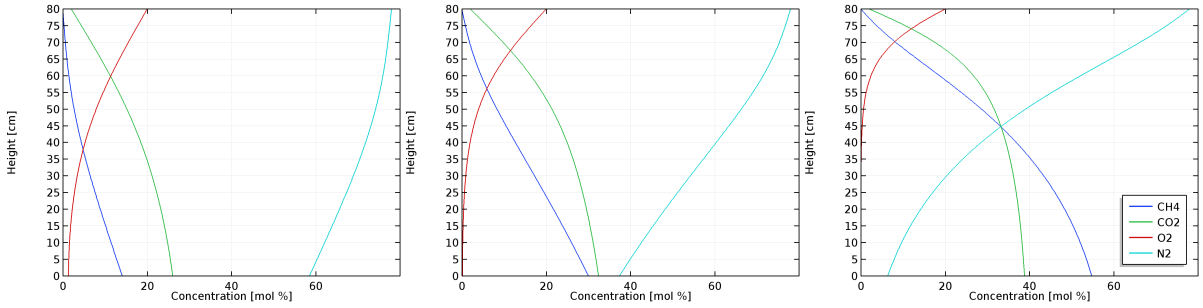

Figure 10.7: Modelled gas profiles for low (A), medium (B) and high (C) degrees of compaction (D_{pr}) at a methane load of $19.11 gCH_4/m^2h$.

11 Simulation results and discussion

This chapter provides the results of the model study. Firstly the results of a single case are presented and discussed. Secondly, all simulated variations are compared to each other and their relevance for the design of methane oxidation systems is elaborated on.

11.1 Results for a single case

The results for the case where the methane load is $100 gCH_4/m^2 day$, the radius is $6m$ and the permeability of the gravel is $1.1 \cdot 10^{-9} m^2$ are presented in this section. The total gas pressures are shown in Figure 11.1 for multiple times. Initially, the total gas pressure is equal to the atmospheric pressure everywhere. It can be seen that the gas pressure builds up faster in the gravel than in the sand. This means that the difference in permeability between the gas distribution layer and the methane oxidation layer indeed works as a resistance, forcing the gas to flow in lateral direction. Then the gas pressure slowly starts to build up in vertical direction until it reaches its peak pressure after about $100s$. Subsequently, the gas pressure starts to decrease again until it reaches steady state after $10,000s$. This peak behaviour can be explained by the slower reaction of the water to pressure change.

The hydraulic phase is initially under hydro-static conditions, see Figure 11.2. When the gas pressure starts to build up, the gas pushes against the water. The water can only move slowly, because the sand is relatively dry. Therefore the hydraulic pressure builds up to a similar amount as the total gas pressure. Therefore, the hydraulic pressure reaches its peak at exactly the same time as the gas pressure. At this point the water start to flow slowly in radial direction towards the regions where the gas pressure is slightly lower. This causes dissipation of the hydraulic pressures and continues until hydro-static conditions are reached again after $10,000s$. The total pressures in the system are now in steady state.

Figure 11.3 depicts the methane fractions in the system. Initially, there is no methane in the system. Then the methane concentration gradually increase throughout the system. At the peak pressures ($300s$) the methane fractions are far from steady state, which is reached around $10,000s$. For this case the pressure builds up to $10 hPa$ over-pressure. Due to this over-pressure the advective flux becomes so large that oxygen is prevented to diffuse into the methane oxidation layer from the top. This can be observed from the methane fractions as well, since only at the top $10cm$ of the methane oxidation layer the methane fractions decrease. This is confirmed by the active zone for the methanotrophs, which is also observed to be confined to this top $10cm$, as illustrated in Figure 11.4.

Lastly, Figure 11.5 presents the methane flux from the gas distribution layer into the methane oxidation layer. This flux is highest above the inlet point and decreases with increasing radius. In the introduction it was determined that the spread was accepted as homogeneous when the flux at the maximum radius was at least (95%) of the flux above the inlet. From this Figure it can be seen that for this case the flux is not homogeneous.

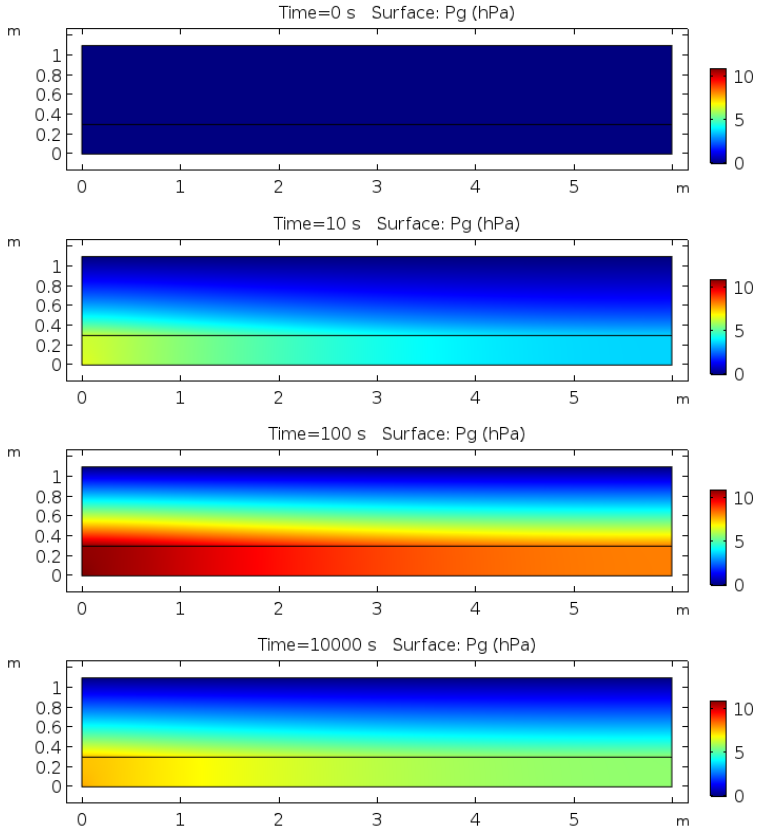

Figure 11.1: Modelled total gas pressure relative to the atmospheric pressure at different times.

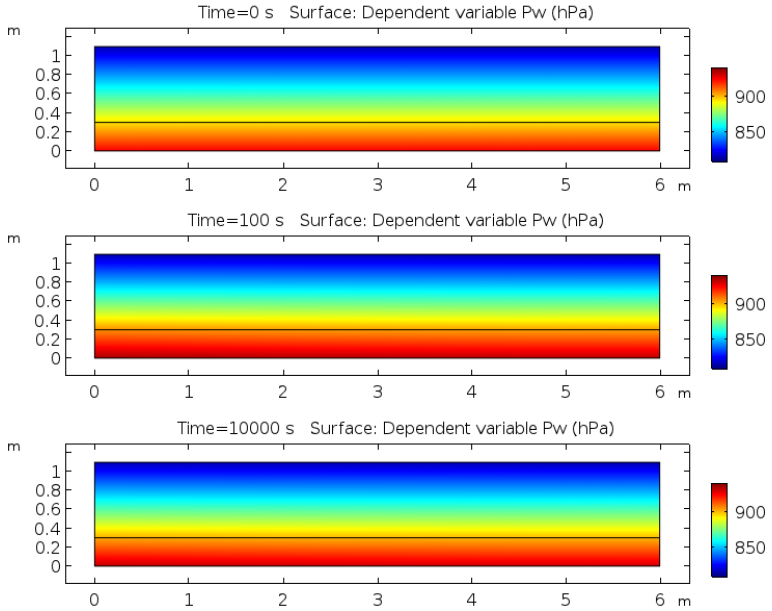

Figure 11.2: Modelled hydraulic pressure relative to the atmospheric pressure at different times.

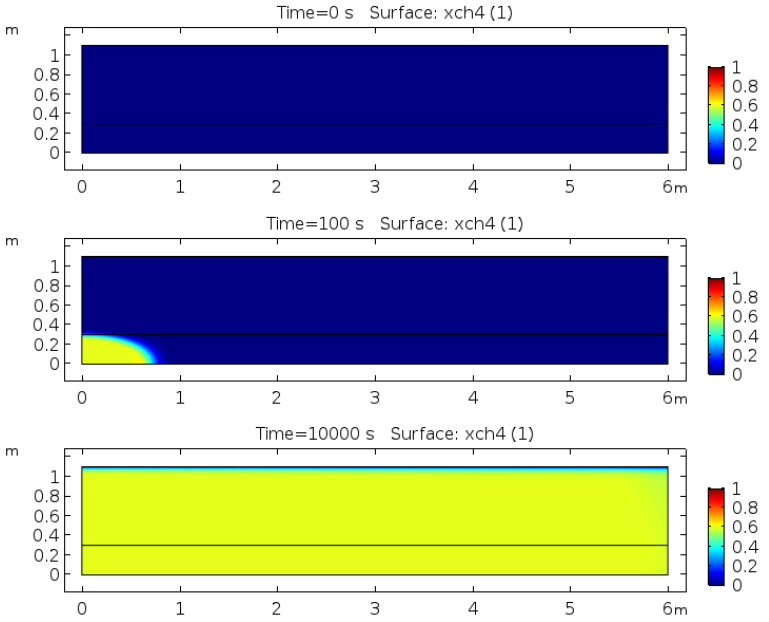

Figure 11.3: Modelled methane fractions at different times.

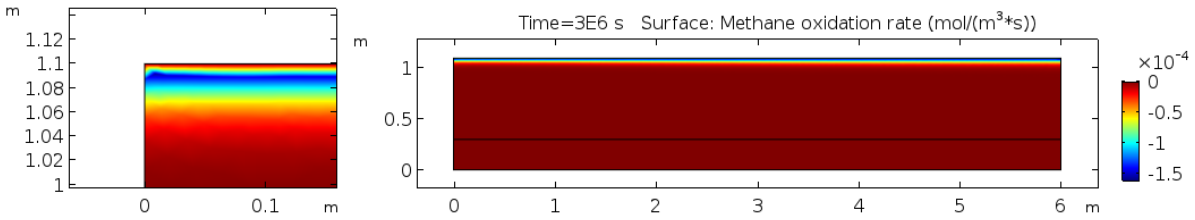

Figure 11.4: Modelled methane oxidation rate at steady state.

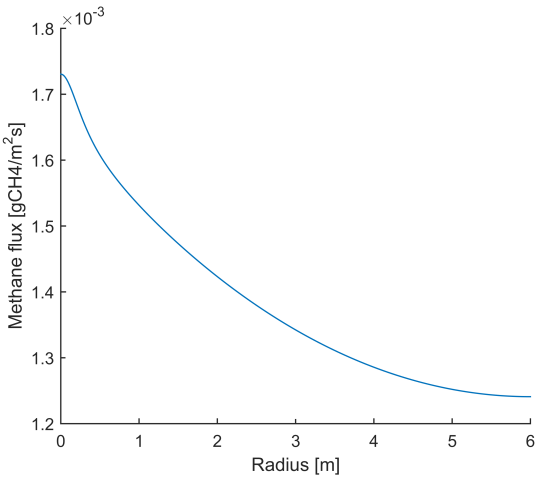

Figure 11.5: The methane flux from the gas distribution layer into the methane oxidation layer at steady state.

11.2 Parametric study

Three parameters were investigated with the parametric study: the permeability of the gravel, the methane load and the radius of the methane oxidation system. The different permeabilities of the gravel were $1.1 \cdot 10^{-8}$, $1.1 \cdot 10^{-9}$ and $1.1 \cdot 10^{-10} m^2$, corresponding to permeability ratios between the gravel and the sand of 1000, 100 and 10, respectively. The methane loads were 20, 50, 100 and $200 gCH_4/m^2 s$. For the radius five different radii were chosen: 3, 6, 9, 12 and $15m$. All combinations were simulated, so a total of 60 cases were simulated. All cases showed similar behaviour as the case elaborated on in the section above.

Figure 11.6 presents the permeability ratio's between the gas distribution layer and the methane oxidation layer. It can be seen that changing the load does not have an influence on the relationship between the radius and the permeability ratio. It was found that changing the load does have an influence on the magnitude of the methane flux into the methane oxidation layer, influencing the amount of oxygen diffusion from the atmosphere into the methane oxidation layer. The methane load is thus an important factor for the performance of the methane oxidation system, but does not influence the spatial homogeneity of the methane flux. Furthermore, the figures depict a clear trend: an increasing radius causes the permeability ratio to decrease, confirming the hypothesis. The data points are fitted with third order polynomial fits, to illustrate this.

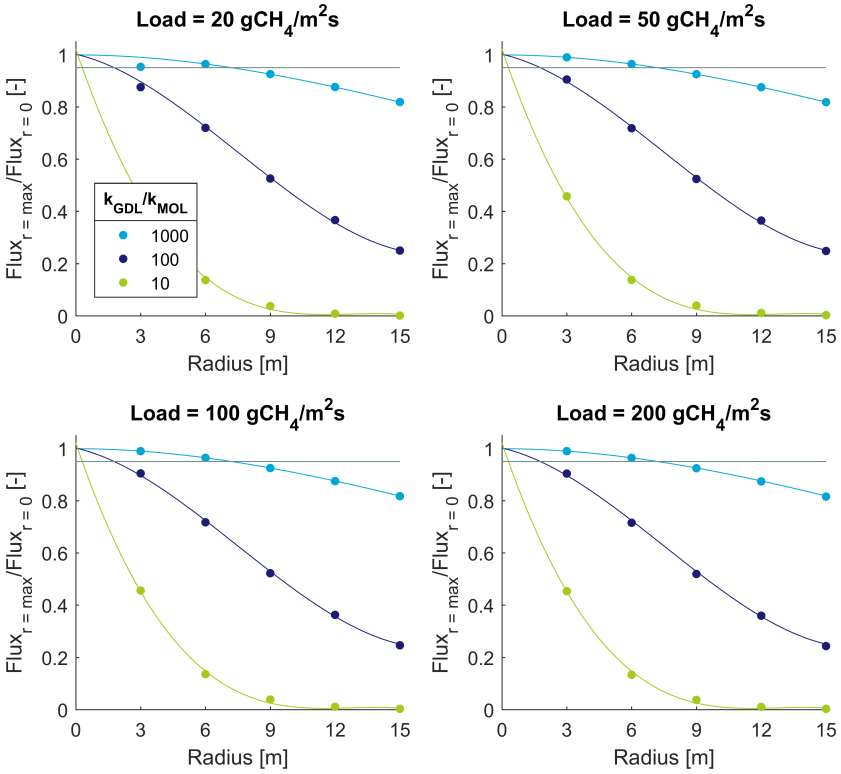

Figure 11.6: Relationship between the flux ratio and the radius for different load cases, fitted by third order polynomials. The grey line at a flux ratio of 0.95 represents the spatial homogeneity criterion.

11.2.1 Design implications

From Figure 11.6, the intersection with line for the permeability ratio of 0.95 were obtained. These intersection points are at the maximum radius allowed for the corresponding permeability ratio for which the spread of the flux still meets the homogeneity requirement. Or vice versa, these intersection points are the minimum required permeability ratio for the corresponding radius. The intersection points are plotted in Figure 11.7. The same is done for two other spatial homogeneity criteria: flux ratios of 0.90 and 0.85. It can be observed that for an increasing radius the minimal needed permeability ratio increases quadratically.

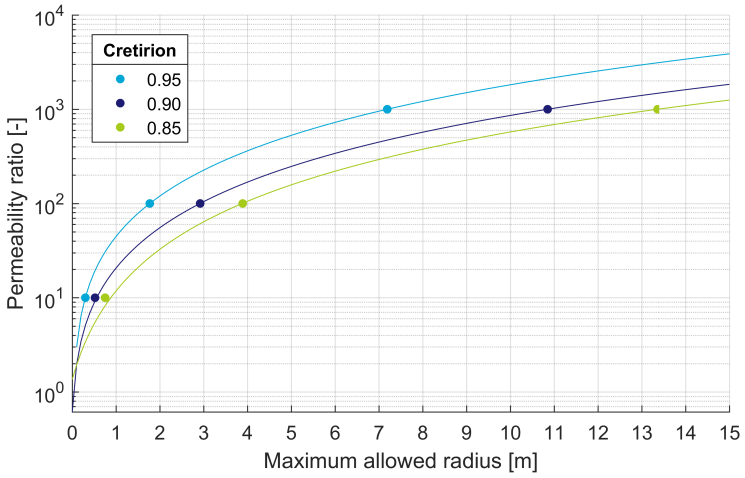

Figure 11.7: Maximum allowed radius for a given permeability ratio for different spatial homogeneity criteria.

Figure 11.7 can be used for two design purposes. Firstly, the inlet design. If a certain sand is available and the contractor wants a spread with a flux ratio of 0.90 as spatial homogeneity criterion, then the gas distribution layer can be optimised by checking which combination of gravel and maximum allowed radius gives the most economic option. For instance if a gravel with a permeability of a 100 times larger than the available sand is very inexpensive, the maximum radius is $3m$ and thus every $6m$ a new inlet is required. It might then be more economic to have a slightly more expensive gravel, for which only every $30m$ an inlet point is required.

Secondly, hot spot remediation. When the methane flux of a hotspot is known, this can be back-calculated for a certain area to the maximum methane load per square meter methane oxidation layer and the according radius. For example, a hot spot generates an emission of $2000gCH4/s$. If the available sand for the methane oxidation layer can handle a maximum load of for instance $80gCH4/m^2s$, this would require a $25m^2$ methane oxidation system (in a square). And thus a radius of $5m^2$ is needed for the system. A gravel with minimal permeability ratio of $10^{2.4}$ in respect to the permeability of the available sand is required. Another option would be installing multiple inlets instead of one.

12 Conclusions on simulations

The laboratory results of sand 1 for the experiment with varying compaction level were simulated with the model. The intrinsic permeabilities obtained by the model were a factor 2 to 4 lower than the intrinsic permeabilities found with the analytical fit. This can be explained by the fact that the numerical model is more extensive than the analytical model, including a discretisation of the soil sample, hydro static hydraulic conditions and free water flow. The simulation results show a correct trend upon an increasing compaction level. Furthermore, the model was verified by modelling a diffusion experiment on a loamy sand as performed by Gebert et al. (2011). Despite the fact that sand 1 differs form the loamy sand on which the experiment was performed, the simulation results show similar behaviour upon compaction to the experimental results from Gebert et al. (2011). It can be concluded that the the advection & diffusion model in combination with the simplified methane oxidation formulation considers the implemented processes correctly. The simulation results show the expected behaviour with adequate accuracy.

The simulation results show that the permeability ratio between the gas distribution layer and the methane oxidation layer works as a gas barrier, allowing gas pressure to built up, and forces the gas to flow into radial direction. In steady state the total gas pressure has a gradient in both vertical and radial directions. The steady state for advective flux is reached, when the water phase reaches hydro-static equilibrium. Water movement is observed in radial direction. The amount of water movement is dependent on the pressure built-up. At higher gas pressures more water movement is observed. This pressure built-up increases with increasing radius and methane load.

Similar to the total gas gradient, the methane flux from the gas distribution layer into the methane oxidation layer shows a decrease with increasing radius. Dividing the methane flux at maximum radius by the methane flux above the inlet gives a flux ratio, which is chosen to be the indicator for the spatial homogeneity of the methane flux. Three parameters were varied to see their effect on this flux ratio: the intrinsic permeabilities of the gravel ($1.1 \cdot 10^{-8}$, $1.1 \cdot 10^{-9}$ and $1.1 \cdot 10^{-10} m^2$), the methane load per square meter of methane oxidation system (20, 50, 100 and $200 gCH_4/m^2 s$) and the radius of the methane oxidation system per inlet point (3, 6, 9, 12 and $15m$). All combinations (60 cases in total) were simulated. Changing the methane load increases the magnitude of the methane fluxes but does not influence the flux ratio given a certain radius. The methane load thus influences the oxygen ingress and is therefore an important parameter in assessing the efficiency of the methane oxidation system. Increasing the radius leads to a decrease in flux ratio. Lastly, an increase of the intrinsic permeability of the gravel and thus a decrease in permeability ratio, leads to a distinct decrease in the flux ratio. It can thus be concluded that the permeability ratio between the methane oxidation layer and gas distribution layer and the centre-to-centre distance between the inlet points are the governing parameters for the spatial homogeneity of the methane flux.

A design plot is generated relating the permeability ratio to the maximum allowed radius (half the

centre-to-centre distance) for various homogeneity criteria. This design plot shows a quadratic increase in permeability ratio with increasing radius. The design plot can be used for the design of gas inlet systems and for the selection of the materials for the gas distribution layer and methane oxidation layer.

Part IV

Conclusions and Recommendations

13 Conclusions

Six research questions, provided in the introduction to this thesis, are answered with this laboratory and numerical study. This chapter presents the answers to these research questions by combining the conclusion of these studies found in Chapters 7 and 12. The last two research questions are answered as one, because they prove to be highly dependent on each other.

13.1 Conclusions per research question

How does the effective permeability of a soil depend on the compaction level of that soil?

The results show that the intrinsic permeability decays exponentially with increasing compaction level due to a decreasing total porosity. Correspondingly, the effective permeability decays exponentially with increasing compaction level due to decreasing air filled porosity. This means that the initial compaction will have a large influence on the effective permeability, while upon further compaction this influence becomes smaller and smaller. Besides the decrease in air filled porosity, it is expected that compaction alters the connectivity and tortuosity of the air filled pore system, which will further enhance the decrease in effective permeability.

How do the hydraulic conditions influence the effective permeability of a soil?

Small decreases in effective permeability are observed upon wetting, followed by a sudden drop when the water content reaches a certain threshold. This is attributed to the water impeding the connectivity of the air filled pore system above this threshold water content. Upon drying the effective permeability converges to the intrinsic permeability for that compaction level, in contrast to altering the intrinsic permeability as happens during compaction. It can be concluded that the water content only influences the effective permeability significantly near saturated circumstances.

How does the effective permeability of a soil depend on the physical properties of that soil?

The sand fraction mainly determines the share of coarse pores. A higher share coarse pores generally leads to a higher intrinsic permeability. From the derived pedotransfer functions, it can be concluded that the capacity to retain water is mainly dictated by the clay fraction and the bulk density of loamy sands. It is observed that different loamy sands can have different effective permeabilities at the same air filled porosity due to the combined effects of soil texture and bulk density. This shows that air filled porosity on its own is not the normative parameter for the effective permeability. The influence of the soil texture on the effective permeability is significant.

How can gas flow within a methane oxidation system be modelled?

The literature study indicates multiple models to simulate gas flow in a methane oxidation system. the advection & diffusion model was chosen based on the inclusion of advective flux and the ease of implementation. Furthermore, a simplified methane oxidation reaction was implemented. The model considers the implemented processes correctly and predicts the expected behaviour with adequate accuracy.

What is the minimum effective permeability ratio between the methane oxidation layer and gas distribution layer for a homogeneous methane flux? And what should the centre-to-centre distance be of the gas inlet points for a homogeneous methane flux distribution?
The permeability ratio between the gas distribution layer and the methane oxidation layer works as a gas barrier, allowing pressure to build up, which forces the gas flow into radial direction. It was observed that this build-up increases with increasing centre-to-centre distance and methane load.

The methane flux from the gas distribution layer into the methane oxidation layer decreases with increasing distance to the inlet point. The flux ratio between the methane flux at maximum distance to the inlet point and the methane flux above the inlet point is chosen as homogeneity criterion. This flux ratio decreases with increasing centre-to-centre distance of the inlet points and with a decreasing permeability ratio between the gas distribution layer and the methane oxidation layer. Increasing the methane load leads to an increase in the magnitude of the methane fluxes, but does not influence the flux ratio given a certain radius. The methane load is thus an important parameter in assessing the efficiency of the methane oxidation system. It can be concluded that the permeability ratio between the methane oxidation layer and gas distribution layer, and the centre-to-centre distance between the inlet points are the governing parameters for the spatial homogeneity of the methane flux.

A design plot is generated, relating these two parameters for various values for the homogeneity criterion. The design plot shows a quadratic increase in required permeability ratio with an increasing centre-to-centre distance. The design plot can be used for the design of gas inlet systems and for the selection of the materials for the gas distribution layer and methane oxidation layer.

13.2 General conclusions

Overall, it can be concluded that the effective permeability is predominantly influenced by the compaction level and the soil texture. The water saturation only shows significant influence at near saturated levels. This means that the choice of suitable material and adequate construction practice will probably have more effect on the effective permeability than seasonal changes in saturation levels in moderate climates.

After assessing the effective permeability of the methane oxidation layer, the spatial homogeneity of the methane flux from the gas distribution layer into the methane oxidation layer can be evaluated. It can be concluded that there are two governing parameters for assessing the spatial homogeneity of the methane fluxes from the gas distribution layer into the methane oxidation layers: the permeability ratio between these layers and the centre-to-centre distance between the inlet points.

14 Recommendations

Several recommendations on the presented laboratory and numerical study are provided in this concluding chapter of this thesis. The most important recommendations for improvement or further investigation are elaborated on.

It is concluded that for sandy soils the changing water content has little effect on the effective permeability upon wetting, until a certain threshold is reached, after which the effective permeability suddenly drops. This is however based on solely the experiment results of one sand. It is necessary to perform this experiment on multiple sandy soils, to investigate if this conclusion holds for sandy soils in general or only for this specific.

The experiment for the influence of compaction on the effective permeability showed a clear trend. It could be further investigated if this trend also holds for sand mixed with compost, sewage sludge, or peat, which are also often used as material for the methane oxidation layer.

A bachelor thesis was performed to investigate the homogeneity reached within the soil samples (ten Bosch, 2017). It was shown that the compaction method adopted in this thesis, creates layers getting denser towards their top. It must therefore be researched what the normative density is for the complete column, where in this thesis the mean density is taken. An other possibility would changing the compaction method to one that results in a more homogeneous soil sample. It must be noted that homogeneity was well established for the low level of sophistication of this compaction method.

The obtained effective permeabilities with the experiment and with the numerical model deviated by a factor of 2 to 4. In range of permeabilities for sand, which can deviate by orders of 10^5, this is a small difference. However, it should be further investigated which result is more reliable.

The numerical model has been verified, but not been validated. The results of this advection and diffusion model show great promise for such a simple model. A validation is recommended to asses if the model simulates the right values, and not just the right trend. The best way to validate the model would be based on field data, as the results of the model are intended for construction purposes. This validation could show if the advection and diffusion model is sufficient or if a more sophisticated gas transport model is required. Furthermore, a validation could demonstrate if the simplification of the methane oxidation process is sufficient for the purpose of gas transport modelling.

The Brooks and Corey formulation of the relative permeability does not show the trend of the influence of the water content on the effective permeability as was obtained from the lab. It decreases, but does not show the sudden drop after a certain threshold. It should be researched if there are other formulations of the relative permeability, which do describe such a trend. If these would be implemented in the model, this would make the model more reliable for sands as methane oxidation layer material.

The model overestimates the the flux ratio, since an circular area with a certain radius receives the load for the square area with this radius. For the purpose of this thesis this is excepted. However, if the design plot is extended for real use, this must be corrected.

Furthermore, it is recommended to simulate more variations in the cases than what was done in this thesis. More data points are always valuable when obtaining a reliable design plot. Different compaction levels, water contents and sand types should be simulated to see if the changes in effective permeability are as observed in the lab, or if there are any side effects due to the numerical model. Furthermore, the effect of a capillary barrier could be taken into account at higher saturation levels.

One of the major limitations of the model is the lack of all transient water processes, like rain, evapotranspiration, root uptake and water generation due to methane oxidation. If the methane oxidation system is in a highly changing hydraulic environment, the model should be extended for these processes. This could be done, by changing the boundary conditions and the source terms. The water transport equations are already sufficient.

Lastly, the design plot could be coupled to various time dependent processes, such as settlement of the methane oxidation system and decreasing methane loads. This could be useful when assessing long term efficiency in the designing phase.

Bibliography

Ahoughalandari, B. and Cabral, A. (2017). Influence of capillary barrier effect on biogas distribution at the base of passive methane oxidation biosystems: Parametric study. *Waste Management*, 63:172–187.

Bear, J. and Cheng, A. (2010). *Modeling Groundwater Flow and Contaminant Transport*. Springer Science & Buisiness Media.

Beghardt, S., Fleige, H., and Horn, R. (2009). Effect of compaction on pore functions of soils in a saalean moraine landscape in north germany. *Journal of Plant Nutrition and Soil Science*, 172(5):688–695.

Benham, E., Ahrens, R., and Nettleton, W. (2009). *Attachment to MO5 soil technical note-16*. National Soil Survey Center, USDA-NRCS, Lincoln, Nebraska.

Bodenkunde, A. (2005). *Bodenkundliche Kartierenaleitung. 5. Auflage*. Bundesanstalt für Geowissenschaften und Rohstoffe und Geologische Landesämter der Bundesrepublik Deutschland, Schweitzerbartsche Verlagsbuchhandlung, Stuttgart.

Bogner, J., Spokas, K., and Burton, E. (1997). Kinetics of methane oxidation in a landfill cover soil: Temporal variations, a whole-landfill oxidation experiment, and modeling of net ch4 emissions. *Environmenta science & technology*, 31(9):2504–2514.

Bohn, S., Brunke, P., Gebert, J., and Jager, J. (2011). Improving the aeration of critical fine-grained landfill top cover material by vegetation to increase the microbial methane oxidation efficiency. *Waste management*, 31(5):854–863.

Cabral, A., Tremblay, P., and Lefebvre, G. (2004). Determination of the diffusion coefficient of oxygen for a cover system including a pulp and paper by-product. *Geotechnical Testing Journal*, 27(2):184–197.

Cao, Y. and Staszewska, E. (2013). Role of landfill cover in reducing methane emission. *Archives of environmental protection*, 39(9):115–126.

Christophersen, M., Linderod, L., Jensen, P., and Kjeldsen, P. (2000). Methane oxidation at low temperatures in soil exposed to landfill gas. *Journal of Environmental Quality*, 29(6):1989–1997.

Czepiel, P., Mosher, B., Crill, P., and Harriss, R. (1996). Quantifying the effect of oxidation on landfill methane emissions. *Journal of geophysical research: Atmospheres*, 101(D11):16721–16729.

de Visscher, A., Thomas, D., Boeckx, P., and van Cleemput, O. (1999). Methane oxidation in simulated landfill cover soil environments. *Environmental Science & Technology*, 33(11):1854–1859.

de Visscher, A. and van Cleemput, O. (2003). Simulation model for gas diffusion and methane oxidation in landfill cover soils. *Waste Management*, 23(7):581–591.

Engineering Toolbox URL (2018). `http://www.engineeringtoolbox.com`. Cited on 1 June 2018.

EPA (2016). *Inventory of U.S. Greenhouse Gas Emissions and Sinks*. Technical report, United Sates Environmental Protection Agency.

Eurostat URL (2017). `http://ec.europa.eu/eurostat/statistics-explained/index.php/Municipal_waste_statistics`. Cited on 14 November 2017.

Fairbanks, D. and Wilke, C. (1950). Diffusion coefficients in multicomponent gas mixtures. *Industrial & Engineering Chemistry*, 42(3):471–475.

Gebert, J. (2017). *AES1640 Environmental Geotechnics*. Lecture slides, Delft University of Technology.

Gebert, J. and Groengroeft, A. (2006). Passive landfill gas emission – influence of atmospheric pressure and implications for the operation of methane-oxidising biofilters. *Waste Management*, 26(3):245–251.

Gebert, J., Groengroeft, A., and Miehlich, G. (2003). Kinetics of microbial landfill methane oxidation in biofilters. *Waste Management*, 23(7):609–619.

Gebert, J., Groengroeft, A., and Pfeiffer, E. (2011). Relevance of soil physical properties for the microbial oxidation of methane in landfill covers. *Soil Biology and Biochemistry*, 43(9):1759–1767.

Gebert, J., Kleinschmidt, V., and Gröngröft, A. (2009). *Gas Permeability Tests - Development of Procedures and Analysis of 9 Materials*. University of Hamburg.

Geck, C. (2017). *Temporal and spatial variability of soil gas transport parameters, soil gas composition and gas fluxes in methane oxidation systems*. Doctoral thesis, University of Hamburg.

Guber, A. and Pachepsky, Y. (2010). *Multimodeling with pedotransfer functions: Documentation and user manual for PTF Calculator (CalcPTF), version 3.0*. Technical report, USDA Rep., Beltsvill Agricultural Research Center, Beltsvill, MD.

Heimovaara, T. (2016). *CIE4365-13 Coupled Processes in Subsurface*. Lecture slides, Delft University of Technology.

Huber-Humer, M. (2004). *Abatement of Landfill Methane Emissions by Microbial Oxidation in Biocovers Made of Compost*. Doctoral thesis, University of Natural Resources and Applied Life Sciences Vienna.

Huber-Humer, M., Gebert, J., and Hilger, H. (2008). Biotic systems to mitigate landfill methane emissions. *Waste Management & Research*, 26(1):33–46.

IenM, M. (2014). *Landelijk afvalbeheerplan 2009-2021*. Technical report, Ministerie van Infrastructuur en Milieu.

IPCC (2007). *Fourth Assessment Report*. Technical report, International panel on climate change.

IPCC (2014). *Fifth Assessment Report*. Technical report, International panel on climate change.

Kightley, D., Nedwell, D., and Cooper, M. (1995). Capacity for methane oxidation in landfill cover soils measured in laboratory-scale soil microcosms. *Applied and Environmental Microbiology*, 61(2):591–601.

Lu, N. and Likos, W. (2004). *Unsaturated Soil Mechanics*. Wiley.

Mason, E. and Malinauskas, A. (1983). *Gas Transport in Porous Media: The Dusty-Gas Model*. Elsevier Science Publishers, Amsterdam.

Moldrup, P., Olesen, T., Gamst, J., nning, P. S., Yamaguchi, T., and Rolston, D. (2000). Predicting the gas diffusion coefficient in repacked soil: Water-induced linear reduction model. *Soil Science Society of America Journal*, 64(5):1588–1594.

NASA URL (2013). `https://www.nasa.gov/mission_pages/sunearth/science/atmosphere-layers2.html`. Cited on 14 November 2017.

Pawlowska, M. and Stephniewski, W. (2006). An influence of methane concentration on the methanotrophic activity of a model landfill cover. *Ecological Engineering*, 26(4):392–295.

Perera, L., Achari, G., and Hettiaratchi, J. (2002). Determination of source strength of landfill gas: A numerical modeling approach. *Journal of Environmental Engineering*, 128(5):461–471.

Piehler, H. (2003). *Transport und Abbau von Methan in der ungesättigten Bodenzone*. Internal report, University of Hamburg.

Röwer, I., Geck, C., Gebert, J., and Pfeiffer, E. (2011). Spatial variability of soil gas concentration and methane oxidation capacity in landfill covers. *Waste Management*, 31(5):926–934.

Sadasivam, B. and Reddy, K. (2014). Landfill methane oxidation in soil and bio-based cover systems: a review. *Reviews in Environmental Scinece and Bio/Technology*, 13(1):79–107.

Sander, R. (2014). Compilation of henry's law constants (version 4.0) for water as solvent. *Atmospheric Chemistry and Physics*, 15(8).

Scheutz, C. and Kjeldsen, P. (2004). Environmental factors influencing attenuation of methane and hydrochlorofluorocarbons in landfill cover soils. *Journal of Environmental Quality*, 33(1):72–79.

Scheutz, C., Kjeldsen, P., Bogner, J., de Visscher, A., Gebert, J., Hilger, H., Huber-Humer, M., and Spokas, K. (2009). Microbial methane oxidation processes and technologies for mitigation of landfill gas emissions. *Waste Management & Research*, 27(5):409–455.

Scheutz, C., Mosbaek, H., and Kjeldsen, P. (2004). Attenuation of methane and volatile organic compounds in landfill soil covers. *Journal of Environmental Quality*, 33(1):61–71.

Standard, B. (2013). *British standard 1377-4*. B.S.I. British Standard.

Stein, V., Hettiaratchi, J., and Achari, G. (2001). Numerical model for biological oxidation and migration of methane in soils. *Practice Periodical of Hazardous, Toxic, and Radioactive Waste Management*, 5(4):225–234.

Tanikawa, W. and Shimamoto, T. (2006). Klinkenberg effect for gas permeability and its comparison to water permeability for porous sedimentary rocks. *Hydrology and Earth System Sciences Discussions*, 3(4):1315–1338.

Tanthachoon, N., Chiemchaisri, C., Chiemchaisri, W., Tudsri, S., and Kumar, S. (2008). Methane oxidation in compost-based landfill cover with vegetation during wet and dry conditions in the tropics. *Journal of the Air & Waste Management Association*, 58(5):603–612.

ten Bosch, S. (2017). *Spatial variability of physical soil properties in constructed columns*. Bachelor thesis, Delft University of Technology.

Thorstenson, D. and Pollock, D. (1989). Gas transport in unsaturated zones: Multicomponent systems and the adequacy of fick's laws. *Water Recsources Research*, 25(3):477–507.

ThoughtCo URL (2017). `https://www.thoughtco.com/chemical-composition-of-air-604288`. Cited on 28 November 2017.

Tuli, A., Hopmans, J., Rolston, D., and Moldrup, P. (2005). Comparison of air and water permeability between disturbed and undisturbed soils. *Soil Scinece Society of America JOURNAL*, 69(5):1361–1371.

van Turnhout, A. (2017). *Characterizing dominant processes in landfills to quantify the emission potential*. Doctoral thesis, Delft University of Technology.

Wang, Y., Wu, W., Ding, Y., Liu, W., Perera, A., Chen, Y., and Devare, M. (2008). Methane oxidation activity and bacterial community composition in a simulated landfill cover soil is influenced by the growth of *Chenopodium album* l. *Soil Biology and Biochemistry*, 40(9):2452–2459.

Warrick, A. (2002). *Soil Physics Companion*. CRC Press, Taylor & Francis Group.

Wilshusen, J., Hettiaratchi, J., de Visscher, A., and Saint-Fort, R. (2004). Methane oxidation and formation of eps in compost: effect of oxygen concentration. *Environmental Pollution*, 129(2):305–314.

Part V

Appendices

A Atmosphere and climate change

The atmosphere is defined from the Earth's surface up to 10.000km height (NASA URL, 2013). Throughout the atmosphere temperature, pressure, air density and composition are changing with altitude. The troposphere, from earth surface to $\pm 10km$ altitude, is influenced by a large number of factors causing climate and weather as we know it. One of these factors is the composition of air. At sea level the composition of air is 78% nitrogen (N_2), 20% oxygen (O_2), and some water vapour, argon, carbon dioxide, and other gases (ThoughtCo URL, 2017). Some of these gases are classified as greenhouse gasses and have a warming effect on the Earth.

A.1 Greenhouse gasses

Greenhouse gasses (GHGs) are gasses that have a high capacity of absorbing infrared radiation reflected from the Earth's surface, thereby trapping heat in the atmosphere (the greenhouse effect). Naturally these gasses occur in the atmosphere. However, due to anthropogenic sources the concentration of these gasses in the atmosphere is increased (IPCC, 2014). Since the pre-industrial era economic and population growth have increased anthropogenic GHG emissions. From 2000 to 2010 emissions were the highest in history. Especially carbon dioxide (CO_2), methane (CH_4) and nitrous oxide (N_2O) atmospheric concentrations show an enormous increase since pre-industrial times (40%, 150% and 20%, respectively) and are driven to levels that are unparalleled in at least the last 800.000 years. CH_4 concentrations, showing the largest increase from $\pm 722ppb$ in 1750 to $\pm 1803ppb$ in 2011, became stable since the late 1990s. Renewed increases, however, are found since 2007 with some projections indicating a further doubling by 2100. CO_2 concentrations are rising faster and faster and N_2O concentrations have been increasing at a steady rate over the last 30 years as can be seen in Figure A.1. These increased emissions enhance global warming.

A.2 Radiative forcing

Radiative forcing is a quantification of the energy uptake into the Earth system caused by GHGs or aerosols (very fine solids suspended in gas, in this case the atmosphere, for instance smoke or mist). It is a simple quantitative value to compare for instance global mean temperature (IPCC, 2014). Positive radiative forcings lead to near-surface warming, and negative radiative forcings to cooling. CO_2 has the largest radiative forcing with 64% and CH_4 the second largest with 17% of the total radiative forcing in 2011. However, there are around 217 times more CO_2 molecules in the atmosphere than CH_4 molecules. This means that 1 CH_4 molecule has a 78 times larger radiative forcing than 1 CO_2 molecule. Luckily CH_4 has a shorter lifespan than CO_2, as it remains in the atmosphere for about 10-15 years (IPCC, 2007). Still over a 100-year period CH_4 is 28 times more effective in trapping heat in the atmosphere (IPCC, 2014). The same hold for N_2O, which is 265 time more effective in trapping heat than CO_2, but fortunately has far less molecules in the atmosphere.

Thus, the rising of the Earth's temperature by radiative forcing is mainly caused by CO_2 and partially by CH_4. Yet one CH_4 molecule is more damaging than one CO_2 molecule.

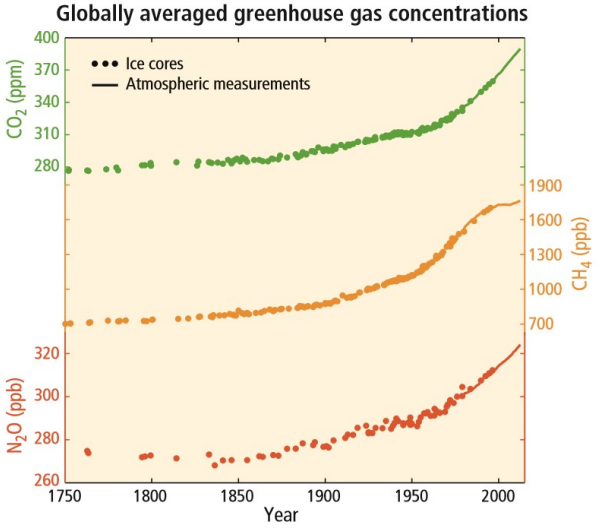

Figure A.1: Global CO_2, CH_4 and N_2O concentrations with time (IPCC, 2014).

B Laboratory details

For the gas distribution layer, the water retention curve was estimated assuming immediate drainage and thus no water retention. In the present study, the effects of hysteresis of the water retention curve was not considered and only the drying curve was used. (Ahoughalandari and Cabral, 2017)

B.1 Sieving tests

For both sands, the clay-, silt-, sand-, gravel-, organic matter- and $CaCO_3$ fractions were already known, as can be seen in Chapter 5. The sand fractions however were unknown. Therefore the fractions of sand were retrieved with sieving tests according to the USDA Standard. 5 sieves were used with diameters of 2, 0.5, 0.25, 0.106 and 0.053mm. The test was performed wet with 100g of oven dry sample. Therefore the fines flushed out. The gravel was discarded, since this is no sand. Two tests were performed per sand type. The mean sand fractions of the two tests are shown in Table B.1.

For the gravel, the general fractions were not known. Therefore one wet sieving test was performed with two sieves with diameter of 2 and 0.063mm; the gravel/sand and sand/silt divisions according to the British Standard (Standard, 2013). The fines again flushed out, thus must be the rest fraction. The fractions can be found in the table below.

Table B.1: Results of the sieving tests on the sands and gravel

Sieve diameter	**Fractions** [$\%dw$]			**Name**	**Classification system**
[mm]	Sand 1	Sand 2	Gravel		
2	-	-	66.15	Gravel	USDA/BS
0.5	15.87	3.42	-	(Very) course sand	USDA
0.25	27.88	16.38	-	Medium sand	USDA
0.106	45.22	75.21	-	Fine sand	USDA
0.063	-	-	-	Sand	BS
0.053	11.02	4.99	32.08	Very fine sand	USDA
rest	-	-	1.77	Silt and clay	USDA/BS

B.2 Proctor tests

For both sands two standard proctor tests (2,5 kg rammer) were performed following the British Standard (2013). The results can be found in Figures B.1 and B.2. The curves are fitted by plotting smooth lines between the points. Furthermore three lines are shown belonging to 5, 10 and 15% air filled porosity (AFP, the volume of air over the total volume). Below, in Table B.2, the proctor densities and corresponding water contents are given. The mean of the two tests was rounded for further use in the experiments.

Table B.2: Proctor test results for the sands

Test	Sand 2		Sand 1	
	Proctor density [g/cm^3]	**Water content** [%]	**Proctor density** [g/cm^3]	**Water content** [%]
Test 1	1,7637	12,85	1,8841	10,79
Test 2	1,7597	13,43	1,9173	10,44
Mean	1,7617	13,14	1,9007	10,62
Used values	**1,76**	**13,1**	**1,90**	**10,6**

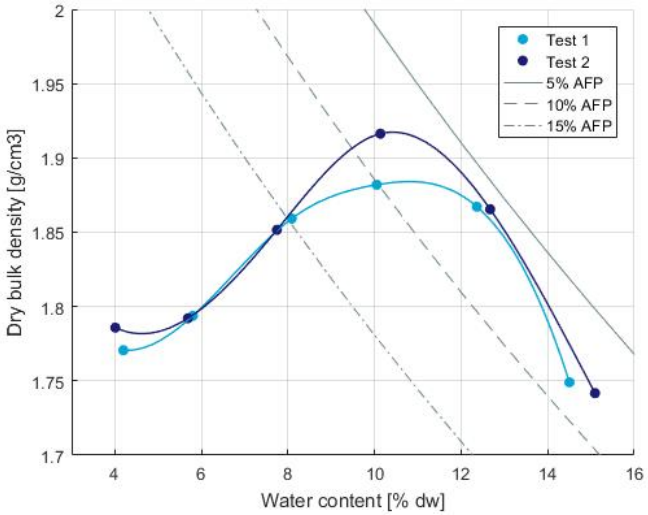

Figure B.1: Proctor curve of sand 1

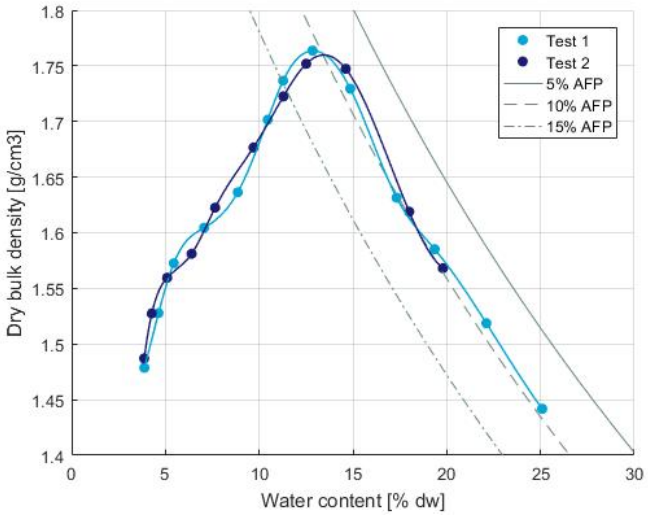

Figure B.2: Proctor curve of sand 2

B.3 Soil preparation

The water retention curves were obtained according to the methods described in 5.2 for both soils with approximately a compaction level of 85%D_{pr}. The results are depicted in Figures B.3 and B.4. The lines according to the capillary pressures used to design the experiment (see 5.2) are indicated with grey. From the intersection points of these lines with the water retention curve, the intended volumetric water contents for the experiments are established.

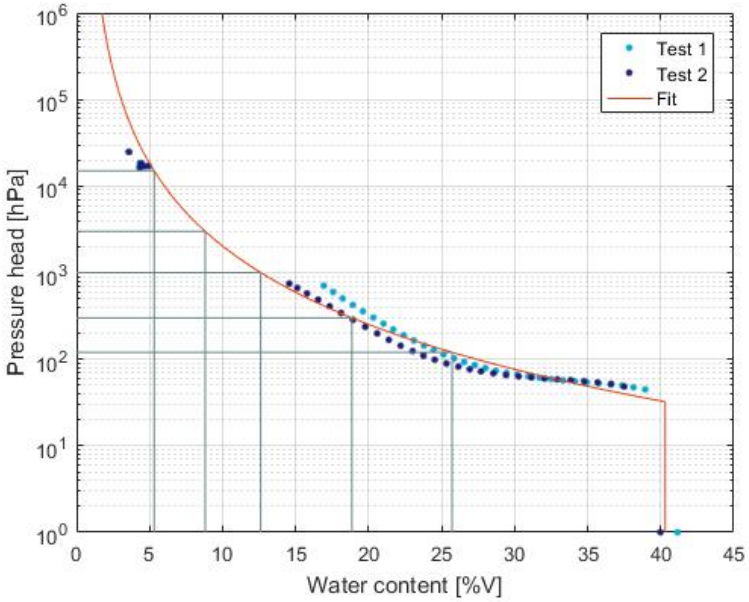

Figure B.3: Water retention curve for the determination of the volumetric water contents for sand 1.

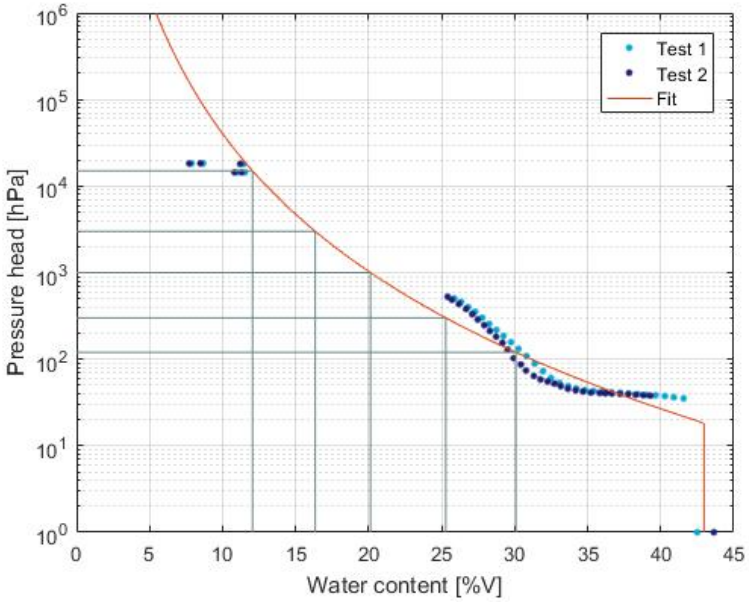

Figure B.4: Water retention curve for the determination of the volumetric water contents for sand 2.

B.4 Compaction energy

As explained in the Chapter 5, letting the falling weight fall 100 time from 1cm height will not have the same effect as letting it fall once from 1m. Therefore, the effective energy must be taken into account in stead of the total energy to compare the compaction energy for construction of the columns to construction in practice. For this reason, multiple falling heights were used on eight columns, which can be found in Table B.3. The amount of soil that went in each 10cm was the same, which means that, for example, letting the falling weight fall 15 times from 5cm height must have approximately an equal effective energy as letting it fall 7 times from 10cm. Therefore, the following empirical formula was conceived. The effective energy E_{eff} $[J]$ is calculated by the potential energy (weight of the falling weight, m [kg] x falling height, h $[m]$) times the a factor, which takes into account that every time the falling weight falls down, it will have less effect. This factor is dependent on the total times the falling weight has fallen n $[-]$ plus a scaling constant β. This scaling constant β is empirically derived to be 1.3 with the data in Table B.3 and the plot shown in Figure B.5.

$$E_{eff} = \frac{n}{\sum_{a=1}^{n} a^{-\beta}} \frac{m \cdot h_{fall}}{h} \tag{B.1}$$

Table B.3: Variations of compaction for different construction layers for several columns.

Column	**Times x height [cm]**		
sand 2-1	15x5	7x10	
sand 2-2	18x10	12x15	10x20
sand 2-3	33x15	23x20	15x30
sand 2-4	34x50	24x70	
sand 2-5	54x90	48x107	
sand 2-7	34x30	18x50	
sand 2-8	29x10	13x15	
sand 2-9	13x15	8x20	

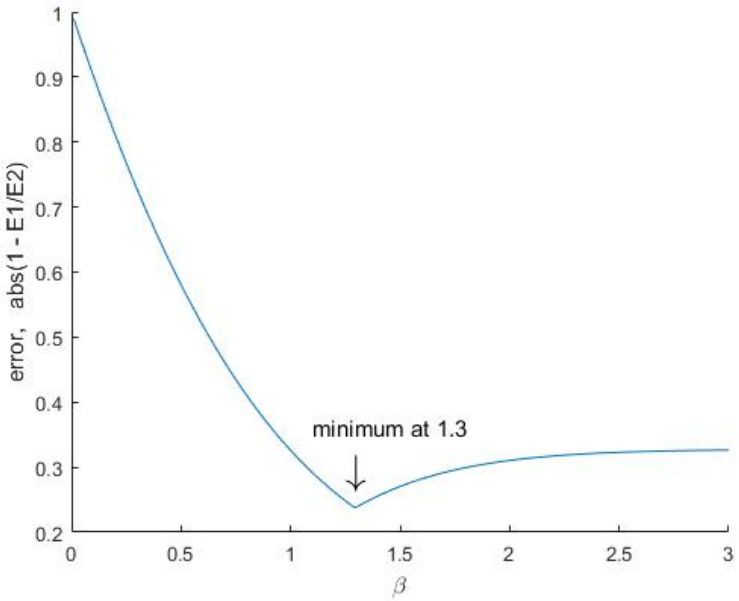

Figure B.5: Optimisation of β, the scaling constant.

B.5 Derivation of equation 5.5

For exponential decay, the following formula hold:

$$P = P_0 e^{-\lambda t} \tag{B.2a}$$

$$\frac{dP}{dt} = -\lambda P \tag{B.2b}$$

From B.2a it is known that at P:

$$P = P_0 e^{-\lambda_S t_S} = P_0 e^{-\lambda_M t_M} = P_0 e^{-\lambda_L t_L}$$

Where S stands for the component flux through the soil column, M stands for the test measurement and, L stand for the leakage measurement. Thus:

$$\lambda_S t_S = \lambda_M t_M = \lambda_L t_L \tag{B.3}$$

Furthermore it is known that:

$$\left(\frac{dP}{dt}\right)_M = \left(\frac{dP}{dt}\right)_S + \left(\frac{dP}{dt}\right)_L$$

And thus from B.2b, the following equation can be derived.

$$\lambda_M = \lambda_S + \lambda_L \tag{B.4}$$

We want to express t_S as a function of t_M and t_L. Equation B.3 can be rewritten and substituting equation B.3 gives:

$$t_S = t_M \frac{\lambda_M}{\lambda_S} = t_M \frac{\lambda_M}{\lambda_M - \lambda_L} = t_M F \tag{B.5}$$

Rewriting F according to equation B.3 gives us equation 5.5.

$$\frac{1}{F} = \frac{\lambda_M - \lambda_L}{\lambda_M} = 1 - \frac{\lambda_L}{\lambda_M}$$

$$F = \frac{1}{1 - \frac{\lambda_L}{\lambda_M}} = \frac{1}{1 - \frac{t_{Mend}}{t_{Lend}}}$$

$$t_S = t_M \frac{1}{1 - \frac{t_{Mend}}{t_{Lend}}}$$

B.6 Derivation of equation 5.7

The number of moles flowing out of the tank should equal the number of moles flowing into the soil column. The number of moles flowing out of the tank can be described by the ideal gas law, see equation B.6. The advection flux through the column can be described with Darcy's law, again shown here as equation B.7.

$$(P + P_{atm})V = nRT \qquad \frac{dn}{dt} = \frac{V}{RT}\frac{d(P + P_{atm})}{dt} = \frac{V}{RT}\frac{dP}{dt} \tag{B.6}$$

$$N^V = -\frac{p}{RT}\frac{\kappa}{\mu}\nabla p \qquad \frac{dn}{dt} = -\frac{A}{L}\frac{\kappa}{\mu}\frac{P}{RT}(P + P_{atm}) \tag{B.7}$$

With P is the tank pressure relative to the atmosphere and P_{atm} is the absolute atmospheric pressure. Equating equations B.6 and B.7 gives equation 5.6:

$$\frac{V}{RT}\frac{dP}{dt} = -\frac{A}{L}\frac{\kappa}{\mu}\frac{P}{RT}(P + P_{atm})$$

Rewriting gives the following differential equation, which can be solved by using partial fractions.

$$\frac{dP}{dt} = -\frac{A}{VL}\frac{\kappa}{\mu}P\,(P + P_{atm}) \tag{B.8}$$

$$\int^{P} \frac{1}{P\left(P+P_{atm}\right)} dx = -\frac{A}{VL}\frac{\kappa}{\mu}\int^{t} 1dt \tag{B.9}$$

$$\int^{P} \frac{1}{P_{atm}}\left(\frac{1}{P}-\frac{1}{P+P_{atm}}\right) dx = -\frac{A}{VL}\frac{\kappa}{\mu}\int^{t} 1dt \tag{B.10}$$

$$\frac{1}{P_{atm}} ln\left(\frac{P}{P+P_{atm}}\right) + C = -\frac{A}{VL}\frac{\kappa}{\mu} t \tag{B.11}$$

Solving for $t = 0$, gives C.

$$C = -\frac{1}{P_{atm}} ln\left(\frac{P_0}{P_0+P_{atm}}\right) \tag{B.12}$$

Now

$$\frac{1}{P_{atm}} ln\left(\frac{P}{P+P_{atm}}\frac{P_0+P_{atm}}{P_0}\right) = -\frac{A}{VL}\frac{\kappa}{\mu} t \tag{B.13}$$

Rewriting to a form where the tank pressures P is a function of the time gives equation 5.7.

$$P = \left(\frac{P_{atm}}{\frac{P_0+P_{atm}}{P_0} - e^{-Ct}}\right) e^{-Ct} \qquad \text{with} \qquad C = P_{atm}\frac{A}{VL}\frac{\kappa_{eff}}{\mu}$$

B.7 Experimental results for the column tests

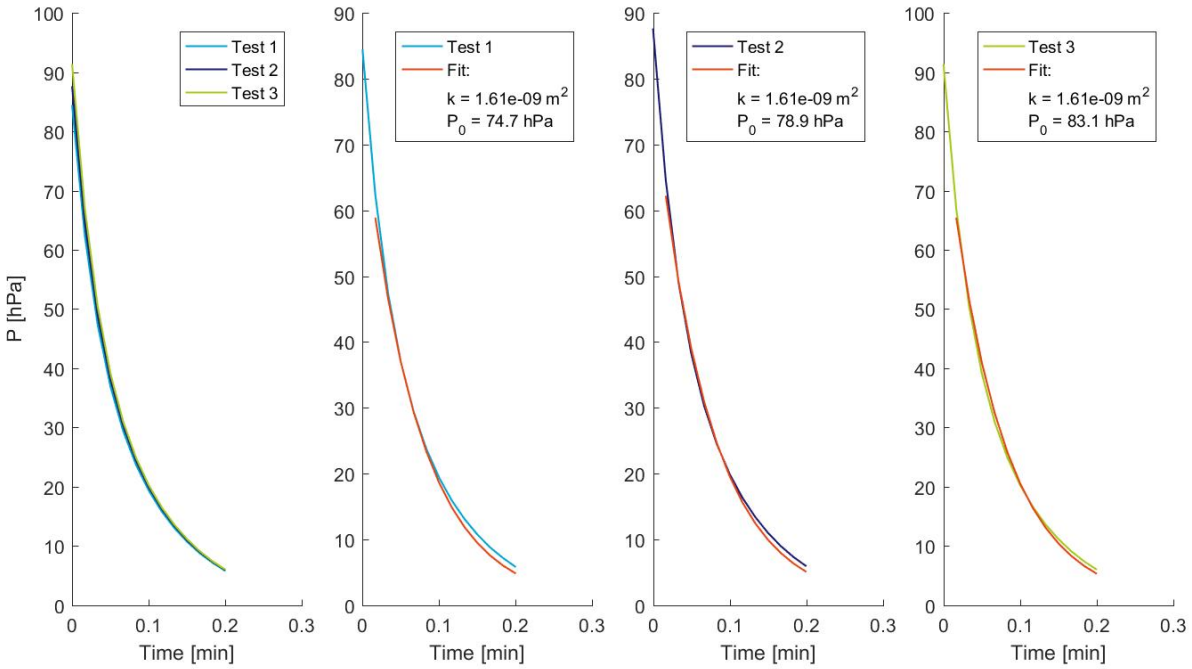

Figure B.6: Change of pressure over time for the experimental set-up. Each pressure loss test is performed in threefold (see 1, 2, 3 in legend). The red line represents the fit, fitted between 5 and 80hPa.

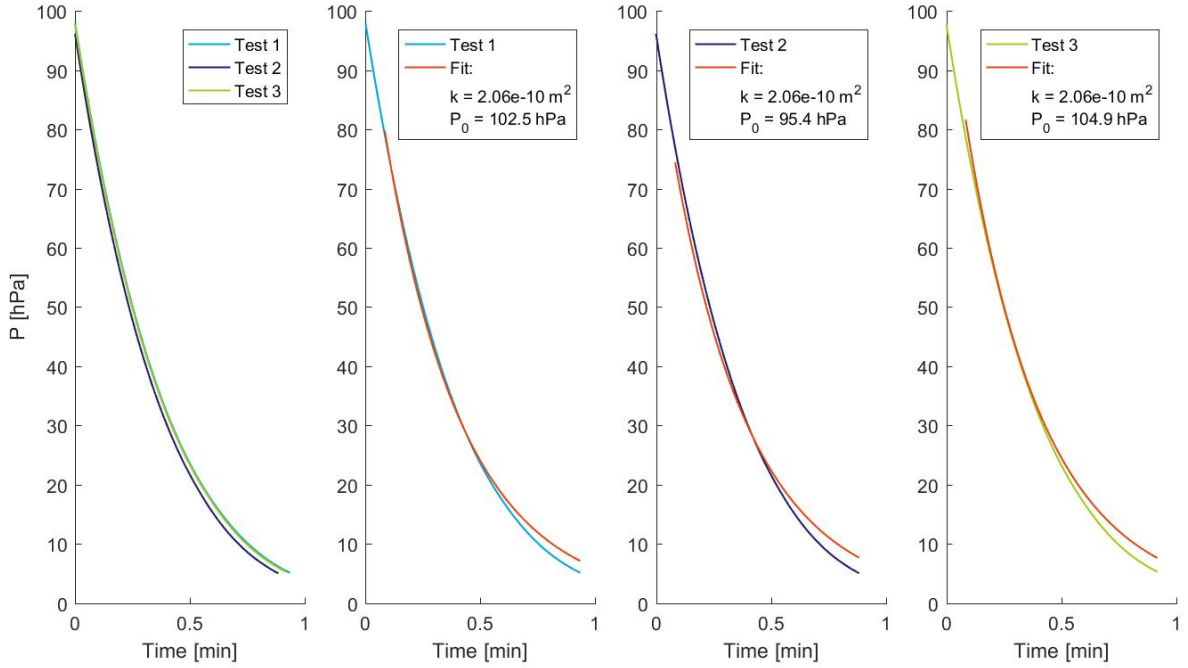

Figure B.7: Change of pressure over time for the gravel. Each pressure loss test is performed in threefold (see 1, 2, 3 in legend). The red line represents the fit, fitted between 5 and 80hPa.

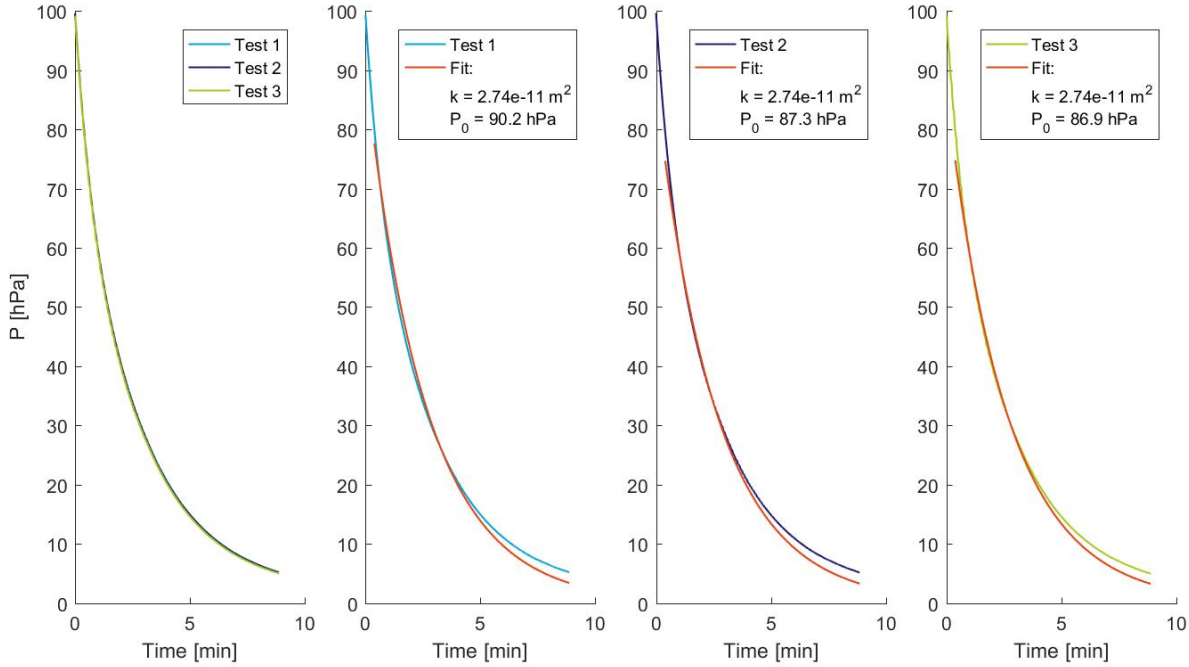

Figure B.8: Change of pressure over time for sand 1, column 1: 75.06%D_{pr}, 12.54%$Vwater$. Each pressure loss test is performed in threefold (see 1, 2, 3 in legend). The red line represents the fit, fitted between 5 and 80hPa.

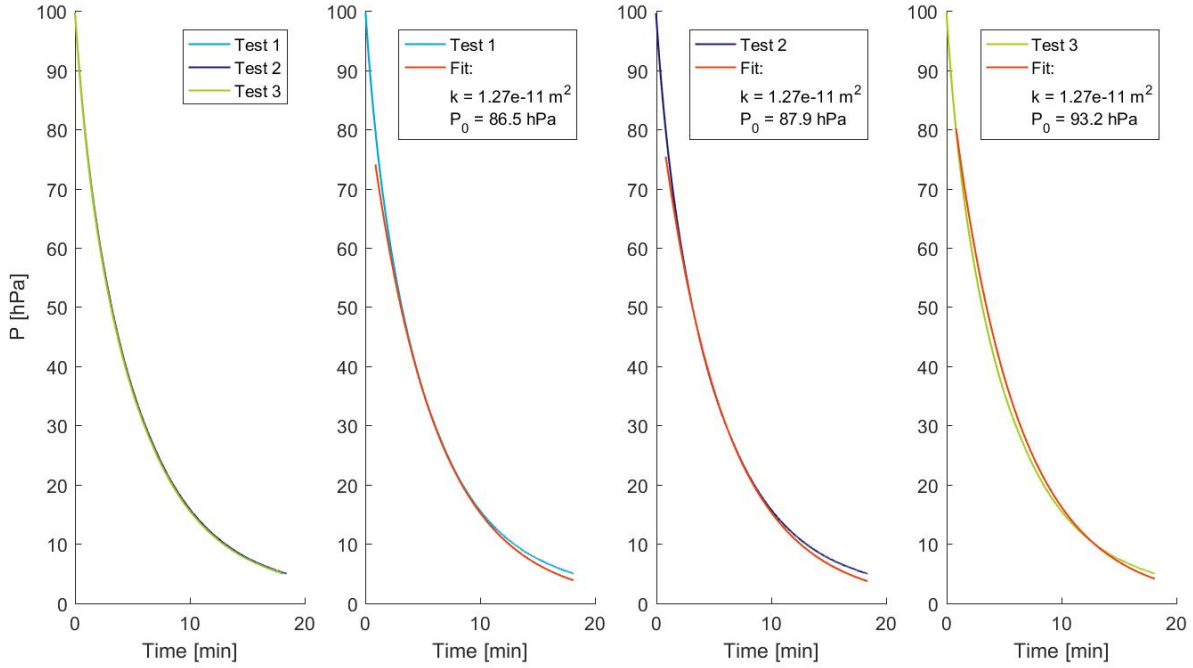

Figure B.9: Change of pressure over time for sand 1, column 2: 79.79%D_{pr}, 12.33%$Vwater$. Each pressure loss test is performed in threefold (see 1, 2, 3 in legend). The red line represents the fit, fitted between 5 and 80hPa.

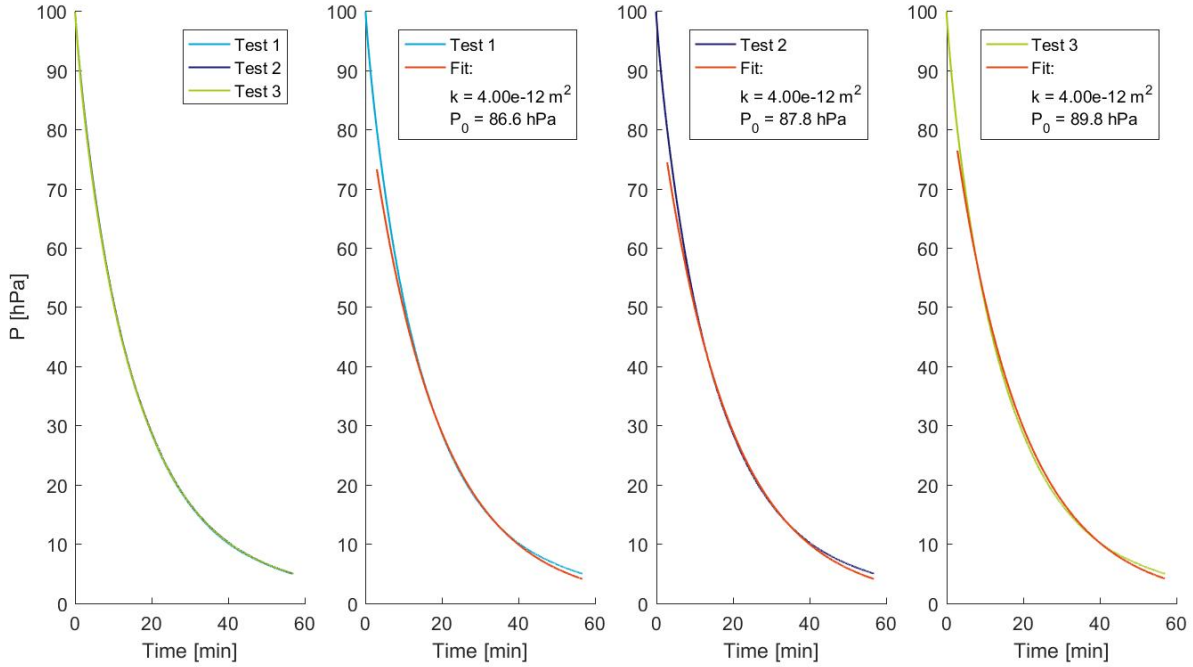

Figure B.10: Change of pressure over time for sand 1, column 3: 85.04%D_{pr}, 12.34%$Vwater$. Each pressure loss test is performed in threefold (see 1, 2, 3 in legend). The red line represents the fit, fitted between 5 and 80hPa.

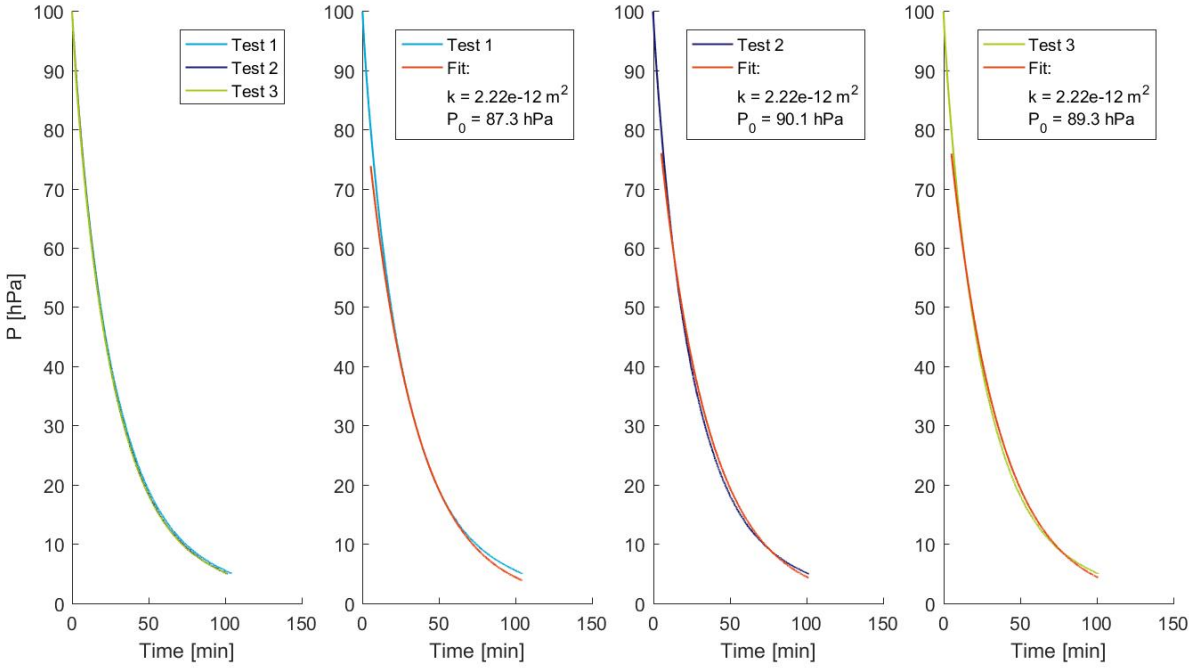

Figure B.11: Change of pressure over time for sand 1, column 4: 88.55%D_{pr}, 12.37%$Vwater$. Each pressure loss test is performed in threefold (see 1, 2, 3 in legend). The red line represents the fit, fitted between 5 and 80hPa.

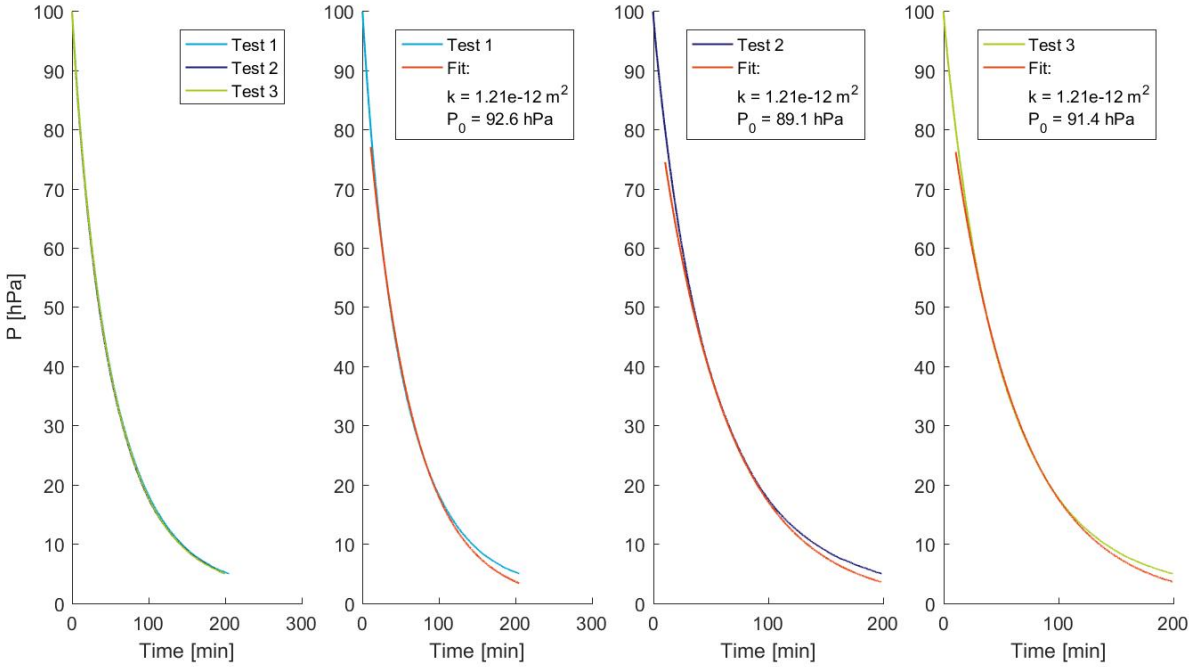

Figure B.12: Change of pressure over time for sand 1, column 5: 93.82%D_{pr}, 12.41%$Vwater$. Each pressure loss test is performed in threefold (see 1, 2, 3 in legend). The red line represents the fit, fitted between 5 and 80hPa.

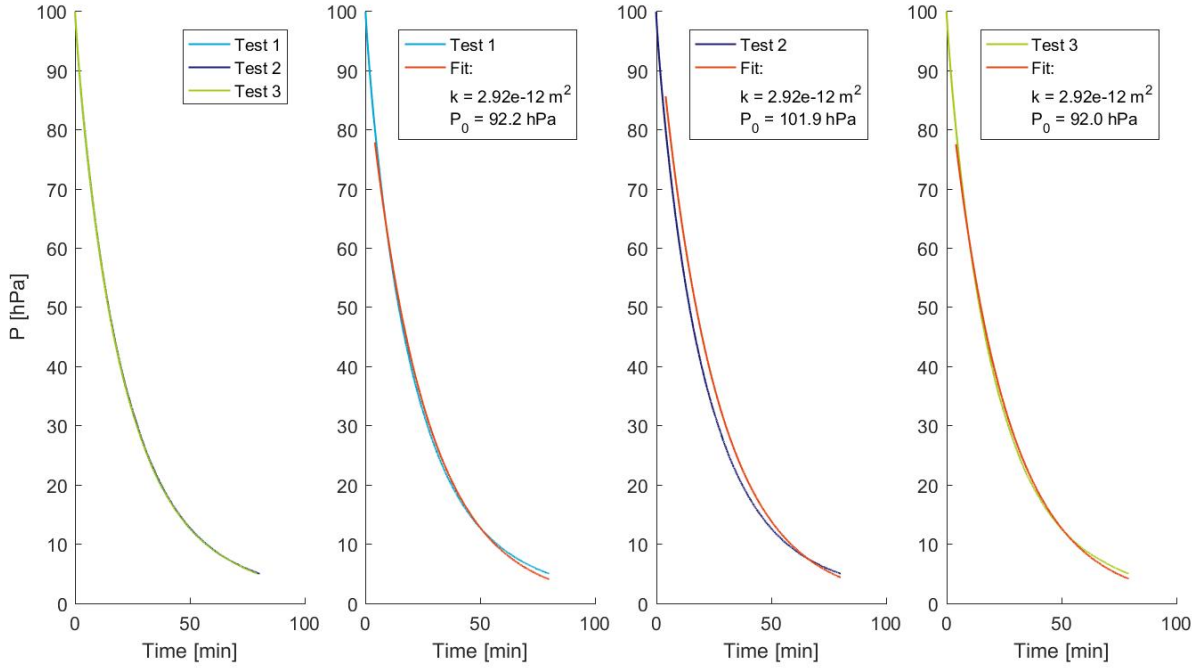

Figure B.13: Change of pressure over time for sand 1, column 6: 83.05%D_{pr}, 4.98%$Vwater$. Each pressure loss test is performed in threefold (see 1, 2, 3 in legend). The red line represents the fit, fitted between 5 and 80hPa.

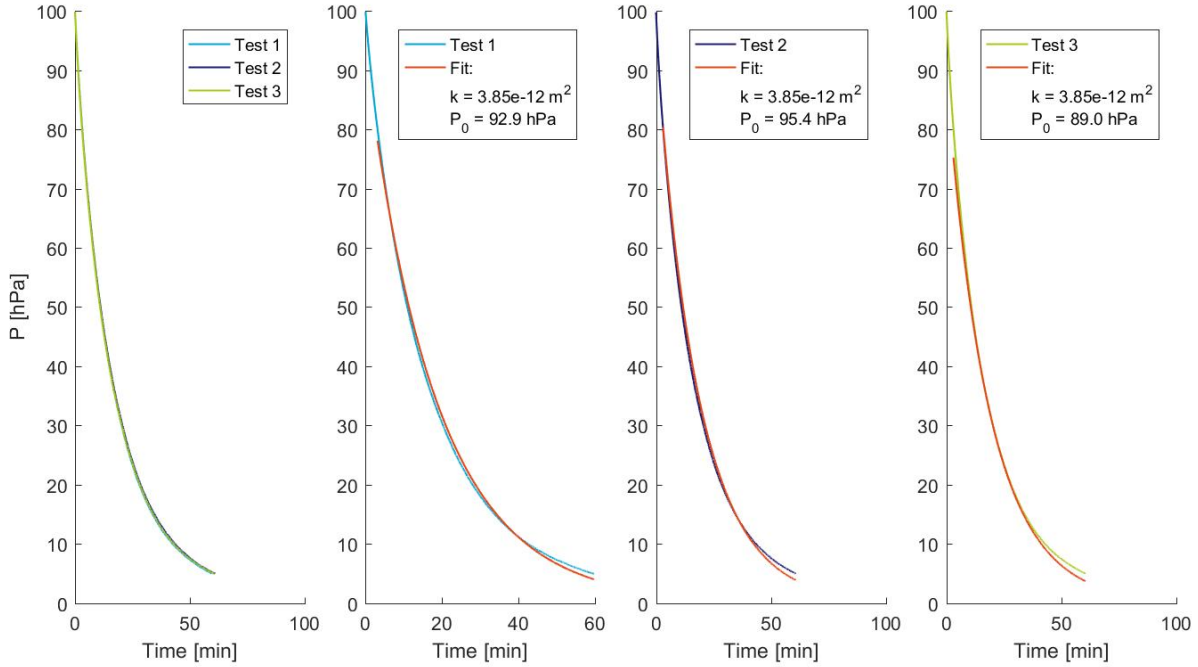

Figure B.14: Change of pressure over time for sand 1, column 7: 84.31%D_{pr}, 8.14%$Vwater$. Each pressure loss test is performed in threefold (see 1, 2, 3 in legend). The red line represents the fit, fitted between 5 and 80hPa.

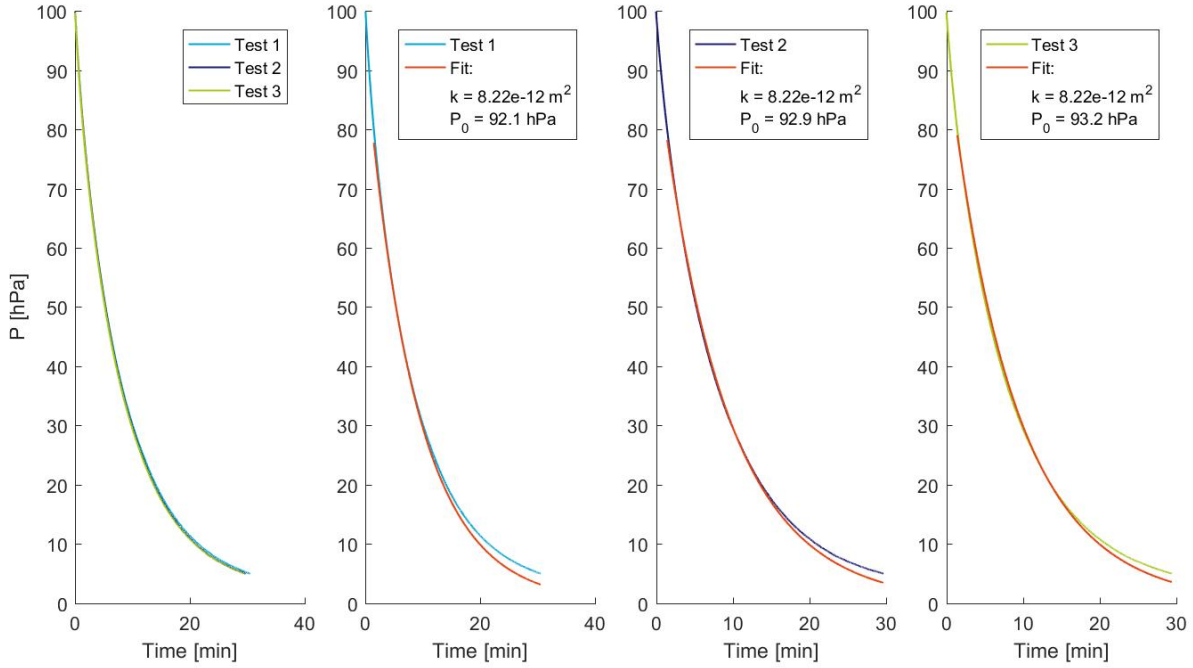

Figure B.15: Change of pressure over time for sand 1, column 8: 84.45%D_{pr}, 18.77%$Vwater$. Each pressure loss test is performed in threefold (see 1, 2, 3 in legend). The red line represents the fit, fitted between 5 and 80hPa.

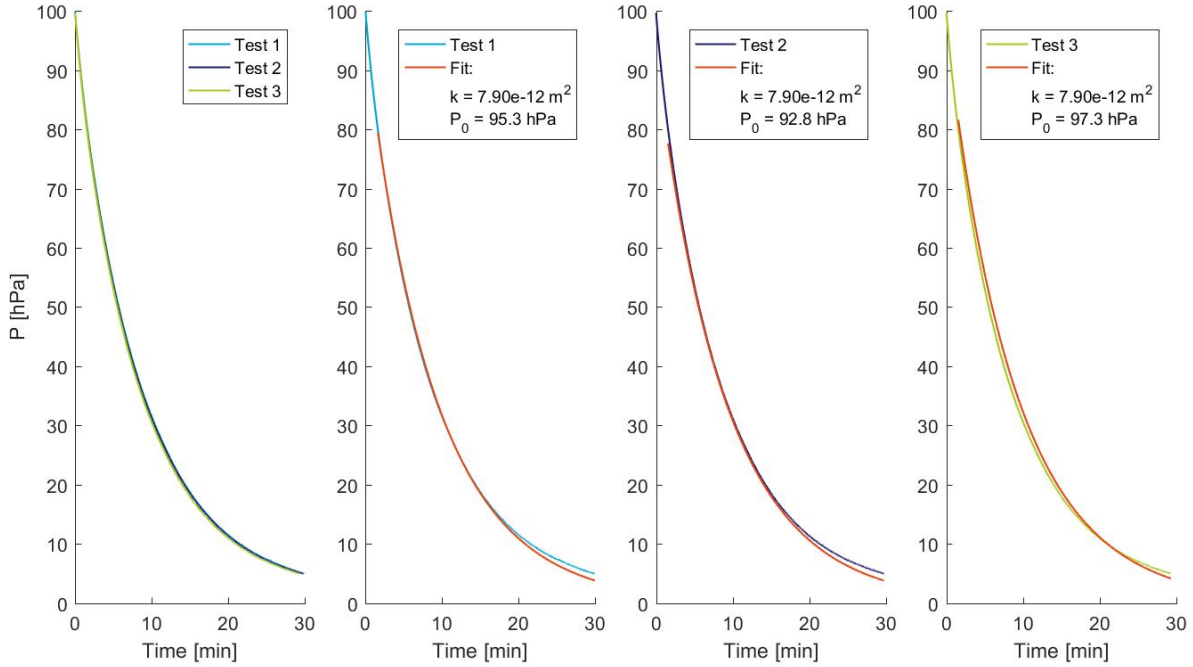

Figure B.16: Change of pressure over time for sand 1, column 9: 84.97%D_{pr}, 30.99%$Vwater$. Each pressure loss test is performed in threefold (see 1, 2, 3 in legend). The red line represents the fit, fitted between 5 and 80hPa.

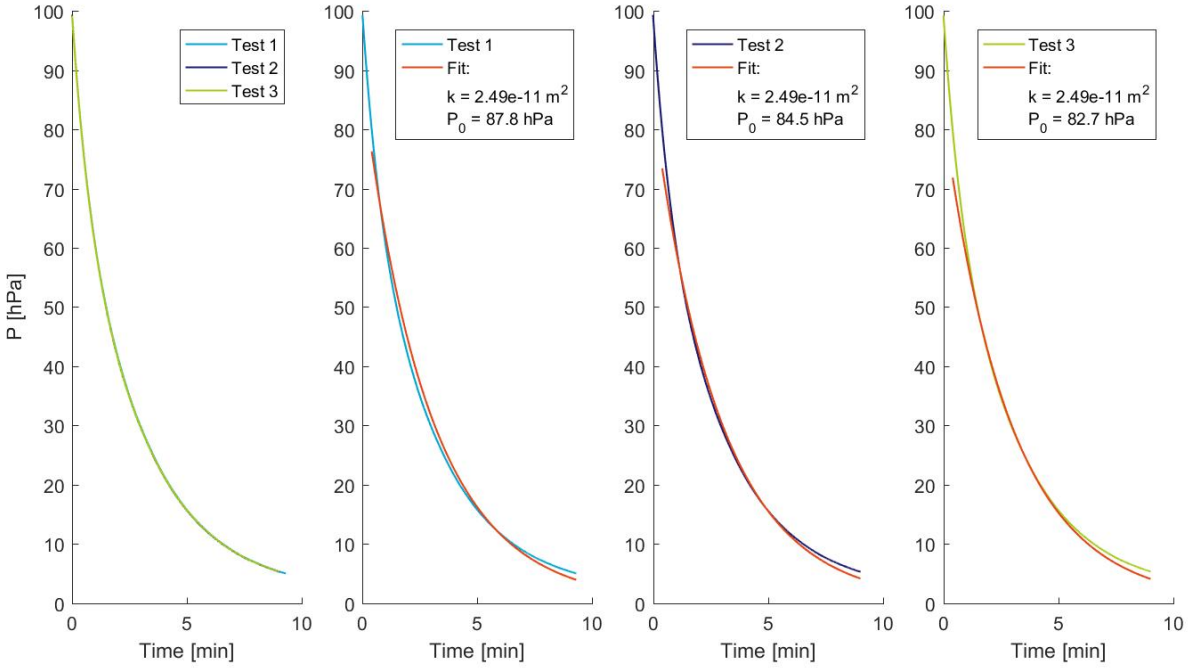

Figure B.17: Change of pressure over time for sand 2, column 1: 74.56%D_{pr}, 20.51%$Vwater$. Each pressure loss test is performed in threefold (see 1, 2, 3 in legend). The red line represents the fit, fitted between 5 and 80hPa.

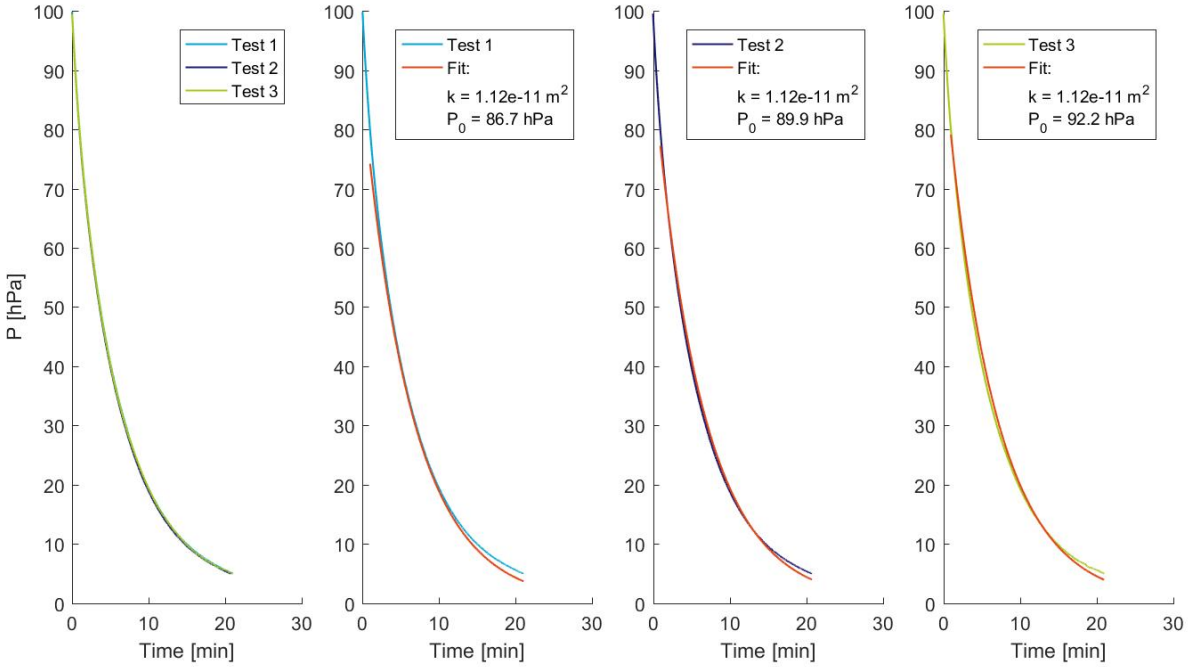

Figure B.18: Change of pressure over time for sand 2, column 2: 79.52%D_{pr}, 20.12%$Vwater$. Each pressure loss test is performed in threefold (see 1, 2, 3 in legend). The red line represents the fit, fitted between 5 and 80hPa.

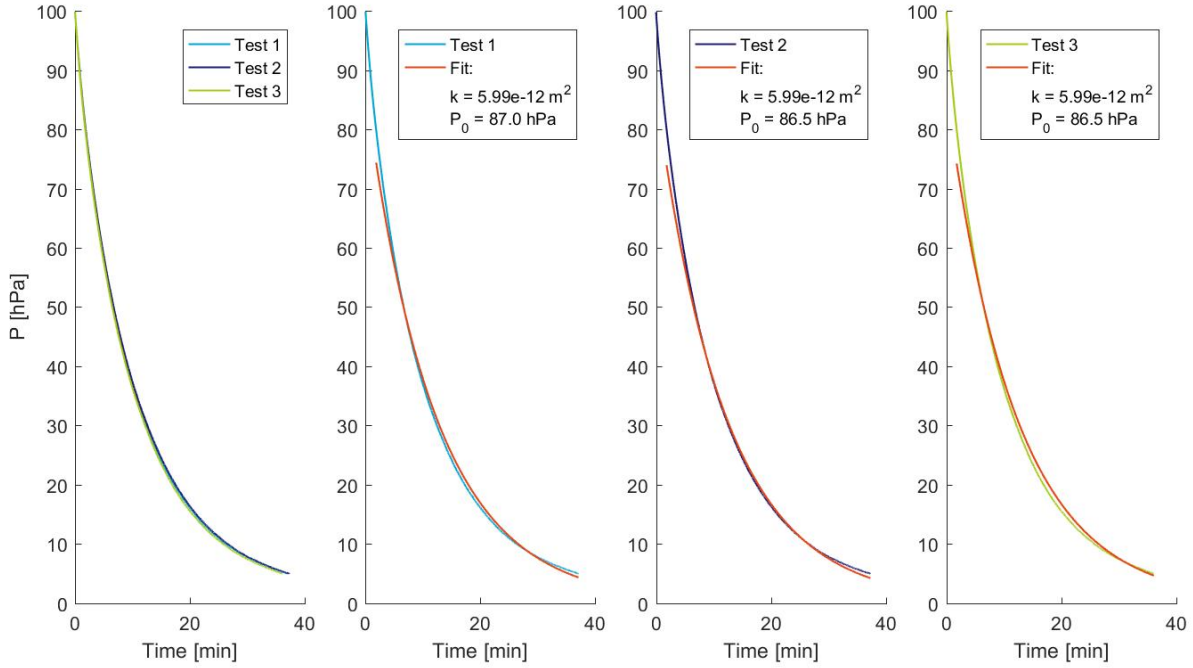

Figure B.19: Change of pressure over time for sand 2, column 3: 84.99%D_{pr}, 20.31%$Vwater$. Each pressure loss test is performed in threefold (see 1, 2, 3 in legend). The red line represents the fit, fitted between 5 and 80hPa.

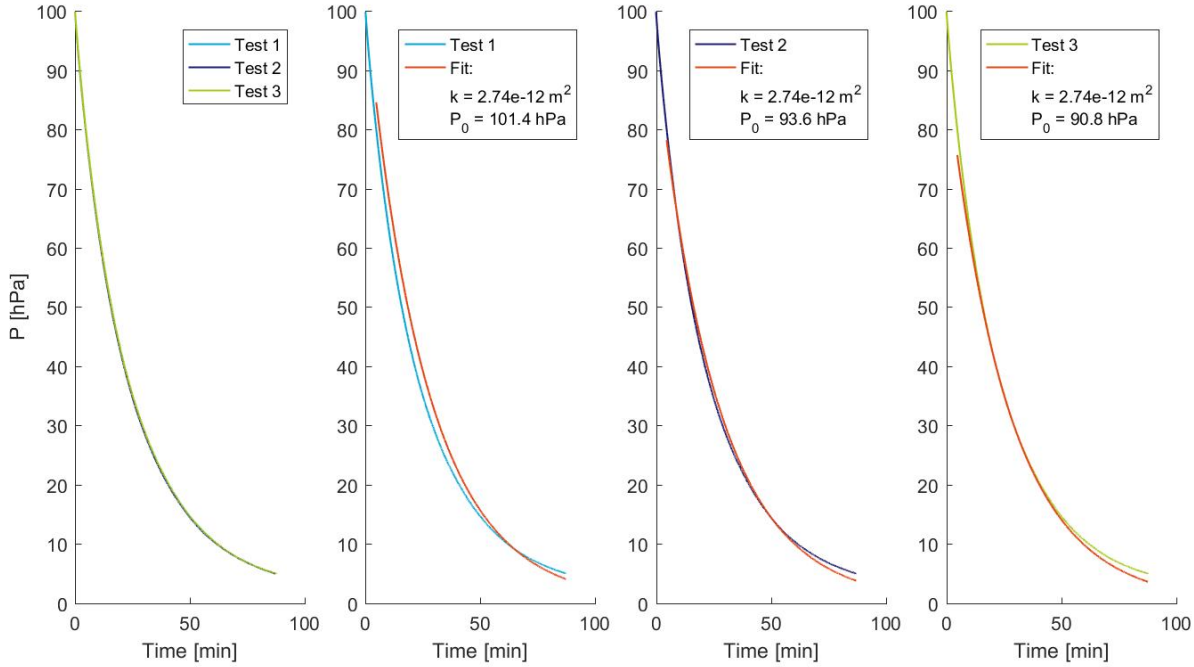

Figure B.20: Change of pressure over time for sand 2, column 4: 89.53%D_{pr}, 20.68%$Vwater$. Each pressure loss test is performed in threefold (see 1, 2, 3 in legend). The red line represents the fit, fitted between 5 and 80hPa.

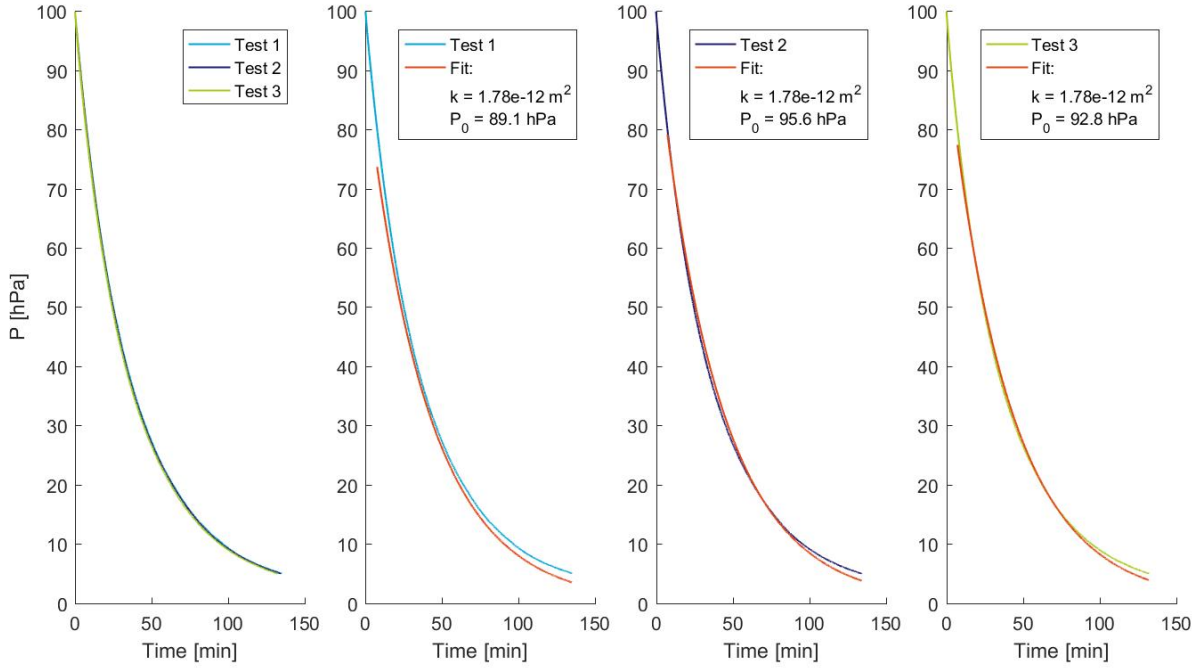

Figure B.21: Change of pressure over time for sand 2, column 5: 95.06%D_{pr}, 19.35%$Vwater$. Each pressure loss test is performed in threefold (see 1, 2, 3 in legend). The red line represents the fit, fitted between 5 and 80hPa.

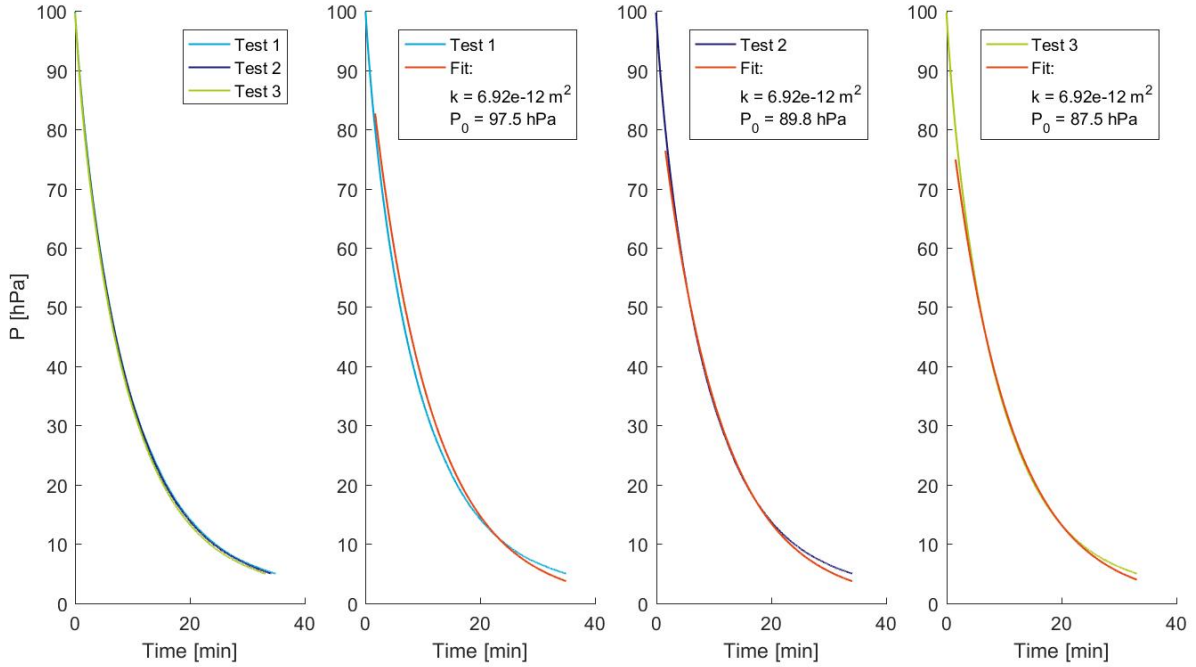

Figure B.22: Change of pressure over time for sand 2, column 6: 84.96%D_{pr}, 12.46%$Vwater$. Each pressure loss test is performed in threefold (see 1, 2, 3 in legend). The red line represents the fit, fitted between 5 and 80hPa.

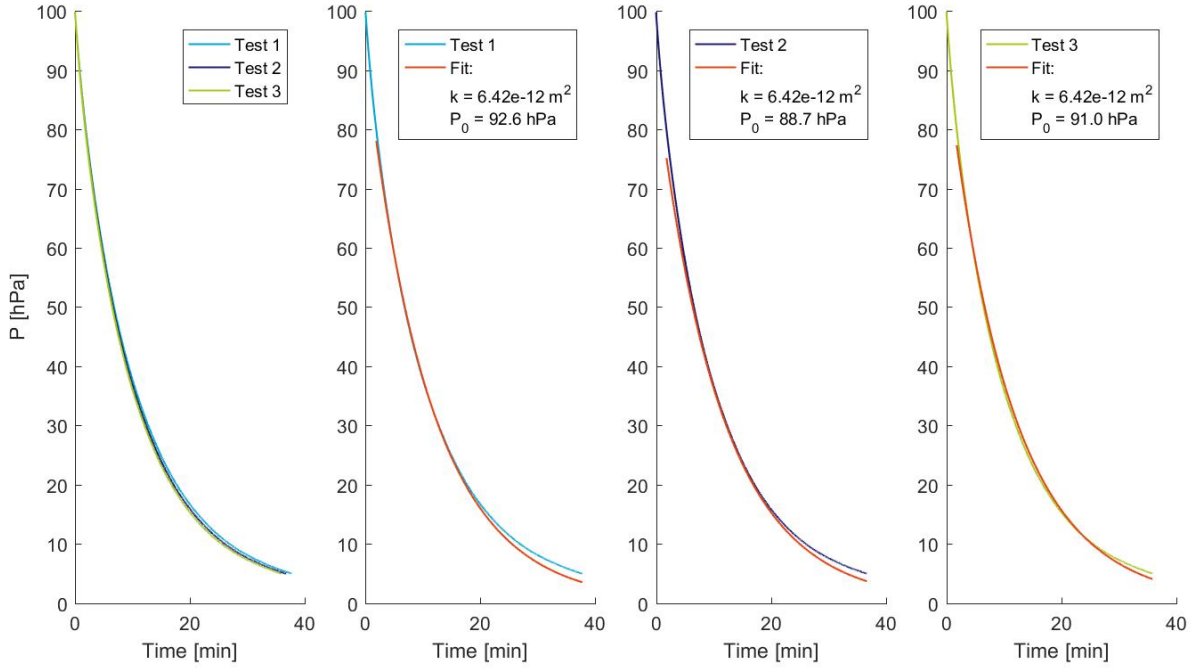

Figure B.23: Change of pressure over time for sand 2, column 7: 85.02%D_{pr}, 16.66%$Vwater$. Each pressure loss test is performed in threefold (see 1, 2, 3 in legend). The red line represents the fit, fitted between 5 and 80hPa.

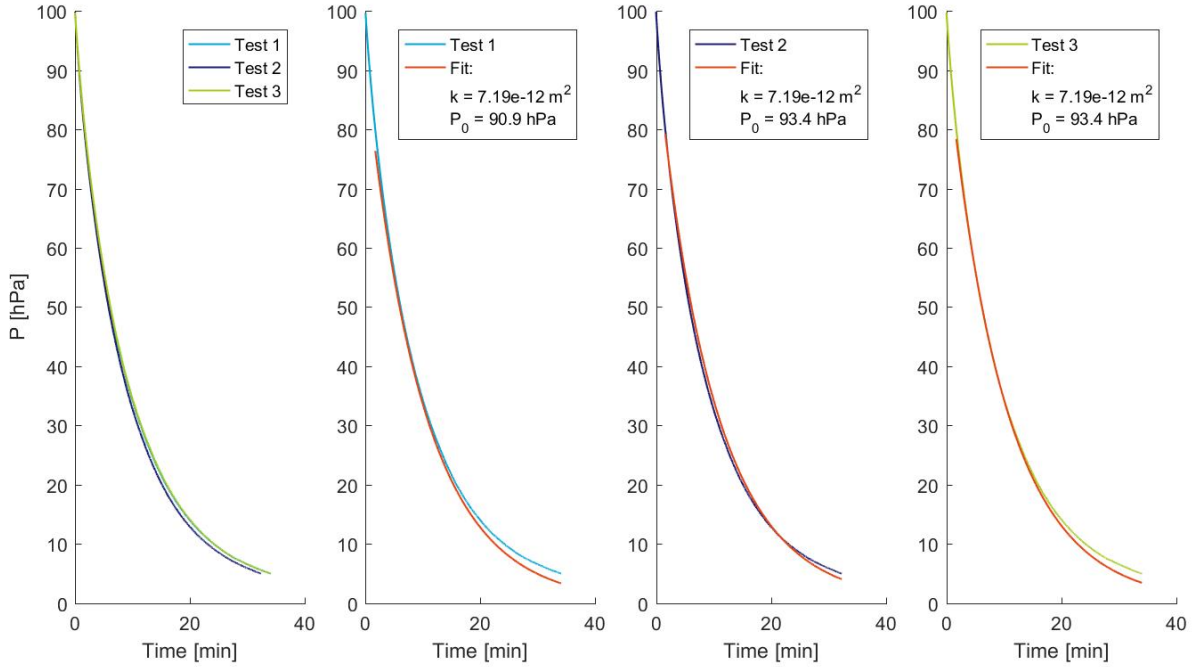

Figure B.24: Change of pressure over time for sand 2, column 8: 84.99%D_{pr}, 25.55%$Vwater$. Each pressure loss test is performed in threefold (see 1, 2, 3 in legend). The red line represents the fit, fitted between 5 and 80hPa.

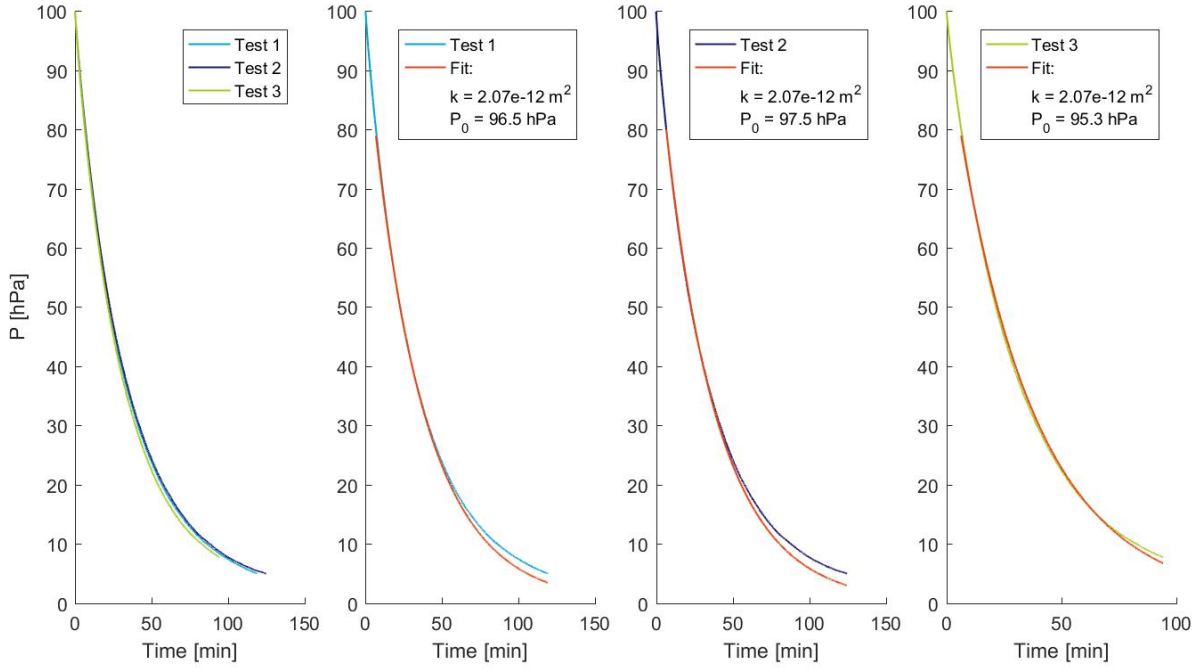

Figure B.25: Change of pressure over time for sand 2, column 9: 84.97%D_{pr}, 30.99%$Vwater$. Each pressure loss test is performed in threefold (see 1, 2, 3 in legend). The red line represents the fit, fitted between 5 and 80hPa.

B.8 Water retention curves

For both sands the water retention curve was obtained at different compaction levels. They are shown in Figure B.26. Sand 2 clearly experiences more impact by the varying compaction than sand 1. This can be explained due to the higher clay fraction in sand 2. Furthermore, sand 2 shows a clear trend: a higher compaction level leads to a shift towards the left of the middle section, while the porosity (data points on the x-axis) decreases. Only the data of the 79.98%D_{pr} does not fit in this trend. This is possibly due to the the sand containing clayey lumps. If one of the tensiometers were in such a lump, this would have the effect the data shows here. In addition there is an other sample at approximately the same density. Therefore, the data of the 79.98%D_{pr} sample is not taken into account for the pedotransfer functions.

The experimental data was fitted as described in Section B.3. This resulted in in a set of Brooks and Corey parameters. Pedotransfer function relate these parameters to the density and soil fractions. For these two soils the following pedotransfer functions were derived. The fits are shown in Figure B.27.

$$\phi = 100 - \rho_d/2.65 * 100 \tag{B.14a}$$

$$\theta_{res} = 0.01 * (0.5 + clay + OC) \tag{B.14b}$$

$$P_e = e^{2*\rho_d + 0.02*clay} \tag{B.14c}$$

$$\lambda = 0.2 + 0.8 * clay - e^{0.14*clay*\rho_d} \tag{B.14d}$$

Where clay and OC are the clay- and organic fractions of the soil in [%]. These functions were based upon functions found within (Guber and Pachepsky, 2010).

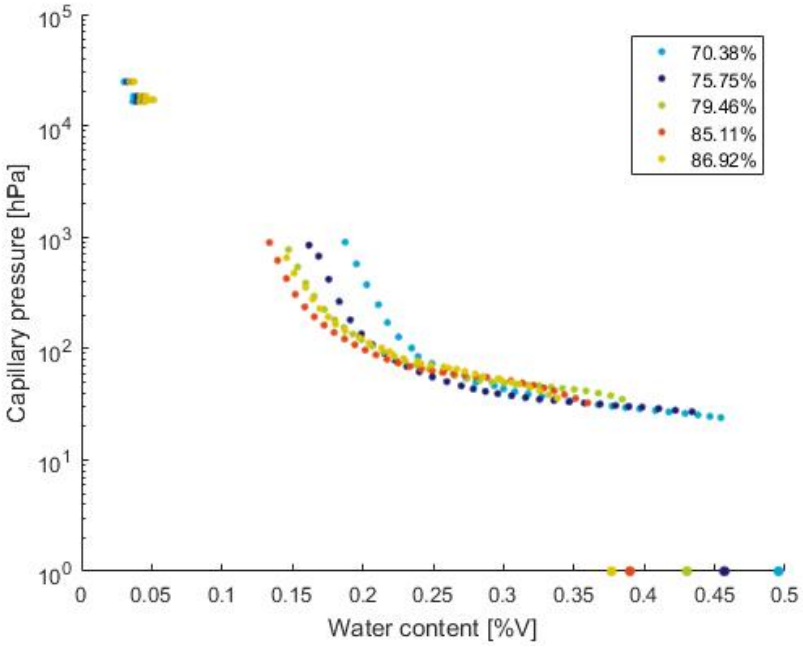

(a) Sand 1

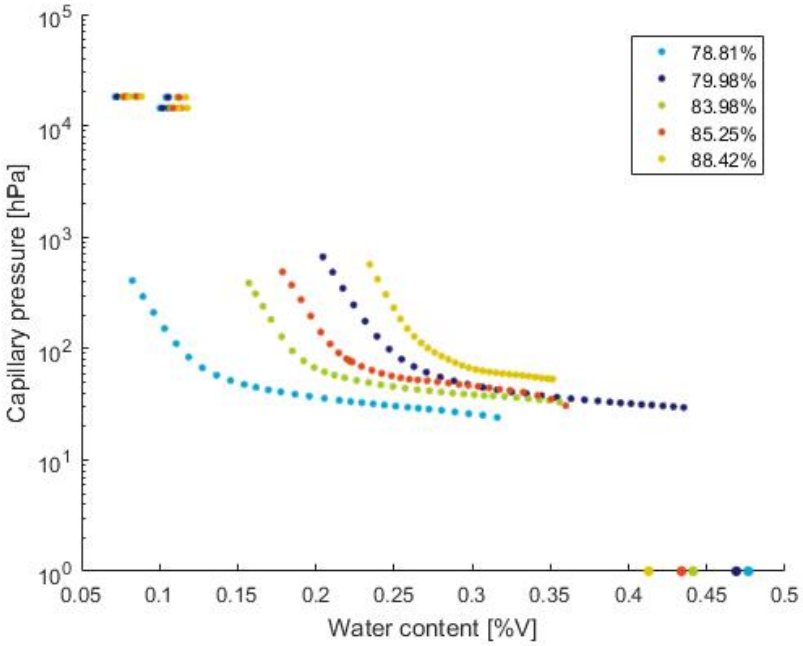

(b) Sand 2

Figure B.26: Water retention curves obtain from the laboratory experiments for both sands at varying densities

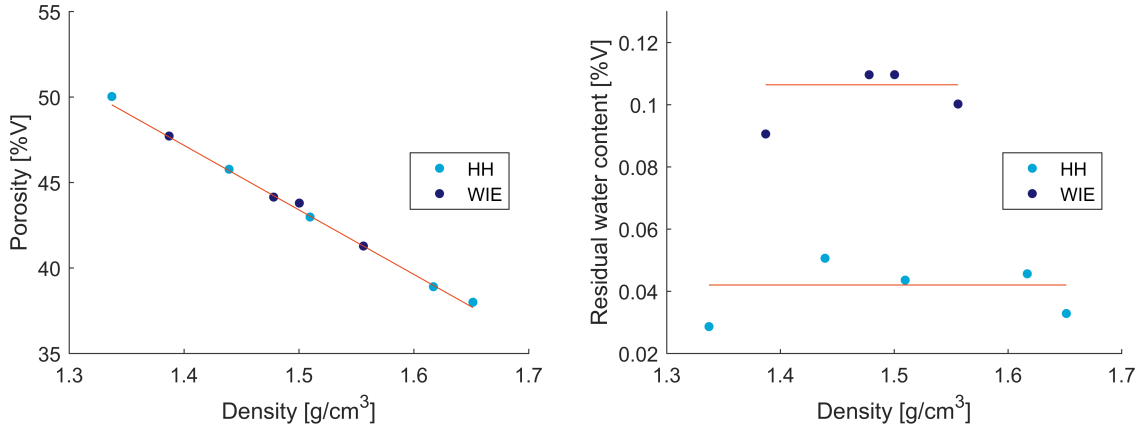

(a) Porosity

(b) Residual water content

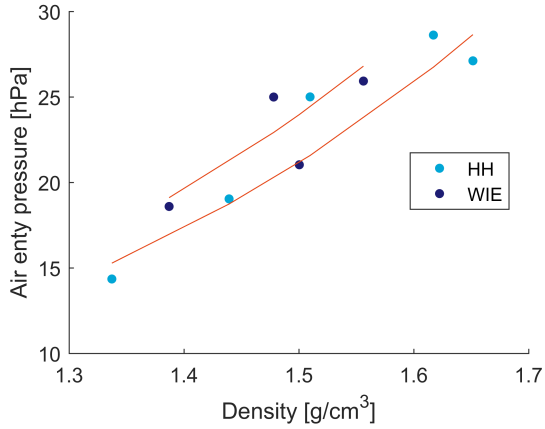

(c) Air entry pressure

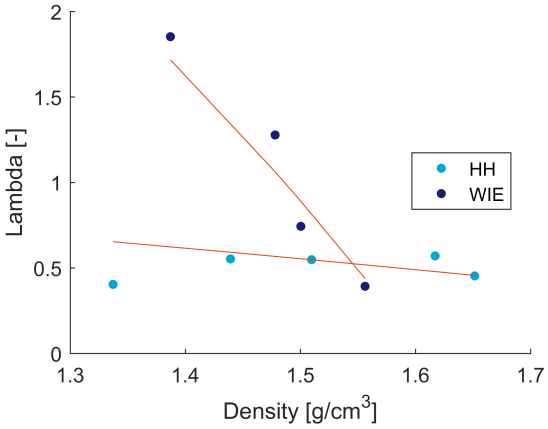

(d) Lambda

Figure B.27: Pedotransfer fits to the water retention parameters according to the Books and Corey formulation

C Derivations

Starting with equations 9.1 and 9.2, gives us:

$$\frac{d\theta_a c_a}{dt} = -\nabla \cdot (J_a) - \nabla \cdot (q_{Ta}\theta_a c_a) - R_a \tag{C.1}$$

Where the concentrations are the number of moles of component a per volume of component a.

C.1 Water phase

Two assumptions are made. Firstly, water is assumed to be driven solely by convection. The diffusive term can thus be discarded. Secondly, water is assumed to be incompressible. Therefore, the concentration of water stays constant in time. Equation C.1 reduces to:

$$c_w \frac{d\theta_w}{dt} = -\nabla \cdot (q_w \theta_w c_w) - R_w \tag{C.2}$$

Given equation 9.3, the change in volumetric water fraction can be rewritten into:

$$\frac{d\theta_w}{dt} = \frac{d\theta_w}{dS_{eff}} \frac{dS_{eff}}{dP_c} \frac{dP_c}{dt} = \frac{d\theta_w}{dS_{eff}} \frac{dS_{eff}}{dP_c} \left(\frac{dP_g}{dt} - \frac{dP_w}{dt} \right) \tag{C.3}$$

Remembering equation 9.5, C_{pc} is now defined as follows, resulting in equation 9.7.

$$C_{pc} = \frac{d\theta_w}{dS_{eff}} \frac{dS_{eff}}{dP_c} = (\phi - \theta_r) \left(-\lambda P_e^{\lambda} P_c^{-\lambda - 1} \right) \tag{C.4}$$

Substituting equations C.3 and C.4 into equation C.2 and rearranging, gives equation 9.6.

$$c_w C_{pc} \left(\frac{dP_g}{dt} - \frac{dP_w}{dt} \right) = -\nabla \cdot (q_w \theta_w c_w) - R_w$$

$$-c_w C_{pc} \frac{dP_w}{dt} + \nabla \cdot (q_w \theta_w c_w) = -c_w C_{pc} \frac{dP_g}{dt} - R_w$$

The Darcy flux q_w is already a function of the water pressure and is therefore as expressed as equation 3.10.

C.2 Gas phase

In contrary to water, gas is compressible. Both the volumetric gas fraction and the total gas concentration now change in time. Furthermore the gas phase comprises of multiple components. Equation C.1 can now be written for component i as:

$$\theta_g \frac{dc_i}{dt} + c_i \frac{d\theta_g}{dt} = -\nabla \cdot (J_i) - \nabla \cdot (q_g \theta_g c_i) - R_i \tag{C.5}$$

Where i stands for component i and g for the total gas phase. The porosity is assumed to be constant. This means that the change in volumetric gas fraction is dependent on the volumetric water fraction. This gives:

$$\frac{d\theta_g}{dt} = \frac{d\phi}{dt} - \frac{d\theta_w}{dt} = -\frac{d\theta_w}{dt} = -C_{pc} \left(\frac{dP_g}{dt} - \frac{dP_w}{dt} \right) \tag{C.6}$$

Rewriting the ideal gas law, gives the following equation, where pressures are absolute.

$$c_i = \frac{n_i}{V_g} = \frac{P_i}{RT} \tag{C.7}$$

Substituting equations C.6 and C.7 into C.5 and rearranging, gives equation 9.10.

$$\frac{\theta_g}{RT}\frac{dP_i}{dt} - \frac{P_i}{RT}C_{pc}\left(\frac{dP_g}{dt} - \frac{dP_w}{dt}\right) = -\nabla\cdot(J_i) - \nabla\cdot(q_g\theta_g\frac{P_i}{RT}) - R_i$$

$$\frac{\theta_g}{RT}\frac{dP_i}{dt} + \nabla\cdot(J_i) + \nabla\cdot(q_g\theta_g\frac{P_i}{RT}) = C_{pc}(\frac{dP_g}{dt} - \frac{dP_w}{dt})\frac{P_i}{RT} - R_i$$

The diffusion term is a function of c_i and must thus also be rewritten to pressure term. Substituting equations 3.15 and C.7 into equation 3.13 this gives equation 9.11.

$$J_i = -\frac{\theta_g^{2.5}D_{im}}{\phi RT}\nabla P_i$$